

A new hydrogen particle source

Citation for published version (APA):

Graaf, de, M. J. (1994). *A new hydrogen particle source*. [Phd Thesis 1 (Research TU/e / Graduation TU/e), Applied Physics and Science Education]. Technische Universiteit Eindhoven. <https://doi.org/10.6100/IR422203>

DOI:

[10.6100/IR422203](https://doi.org/10.6100/IR422203)

Document status and date:

Published: 01/01/1994

Document Version:

Publisher's PDF, also known as Version of Record (includes final page, issue and volume numbers)

Please check the document version of this publication:

- A submitted manuscript is the version of the article upon submission and before peer-review. There can be important differences between the submitted version and the official published version of record. People interested in the research are advised to contact the author for the final version of the publication, or visit the DOI to the publisher's website.
- The final author version and the galley proof are versions of the publication after peer review.
- The final published version features the final layout of the paper including the volume, issue and page numbers.

[Link to publication](#)

General rights

Copyright and moral rights for the publications made accessible in the public portal are retained by the authors and/or other copyright owners and it is a condition of accessing publications that users recognise and abide by the legal requirements associated with these rights.

- Users may download and print one copy of any publication from the public portal for the purpose of private study or research.
- You may not further distribute the material or use it for any profit-making activity or commercial gain
- You may freely distribute the URL identifying the publication in the public portal.

If the publication is distributed under the terms of Article 25fa of the Dutch Copyright Act, indicated by the "Taverne" license above, please follow below link for the End User Agreement:

www.tue.nl/taverne

Take down policy

If you believe that this document breaches copyright please contact us at:

openaccess@tue.nl

providing details and we will investigate your claim.

A New Hydrogen

Particle

Mark de Graaf

A NEW HYDROGEN PARTICLE SOURCE

PROEFSCHRIFT

ter verkrijging van de graad van doctor aan de Technische
Universiteit Eindhoven, op gezag van de Rector Magnificus,
prof.dr. J.H. van Lint, voor een commissie aangewezen door
het College van Dekanen in het openbaar te verdedigen op
dinsdag 27 september 1994 om 16.00 uur

door

Markus Jozef de Graaf

geboren te Zwolle



Dit proefschrift is goedgekeurd door de promotoren:

prof.dr.ir. D.C. Schram

en

prof.dr. A.W. Kleyn

en de copromotor:

dr.ir. M.C.M. van de Sanden

The work described in this thesis was supported by the Netherlands organizations "Fundamenteel Onderzoek der Materie (FOM)" and "Nederlandse Organisatie voor Wetenschappelijk Onderzoek (NWO)".

Contents

1	General introduction	1
2	The experimental setup	5
2.1	The expansion chamber	6
2.2	The cascaded arc source	6
2.3	Plasma operation	10
2.4	Safety considerations	14
2.5	Conclusions	15
3	Atomic hydrogen source featuring recirculation	17
3.1	Introduction	17
3.2	The plasma source	18
3.2.1	Results	21
3.3	Plasma beam	24
3.4	Recirculation	27
3.5	Discussion	31
3.5.1	Experimental techniques	31
3.5.2	Implications of the recirculation process	31
4	Anomalous recombination in a hydrogen plasma jet	33
4.1	Introduction	33
4.1.1	The plasma source	34
4.1.2	The plasma jet	35
4.2	Conclusions	40
5	The atomic hydrogen Balmer spectrum	43
5.1	Introduction	43
5.2	Experimental setup	44
5.3	Atomic state distribution function	45
5.4	Experiments	47
5.5	Discussion	50
6	Molecular excitation and the Fulcher α spectrum	55
6.1	Introduction	55
6.2	Molecular structure	56
6.2.1	Angular-momentum coupling: Hund's case (b)	57
6.2.2	Symmetry rules	58
6.3	Radiative transitions	60
6.3.1	Selection rules	60

6.3.2	Line strengths	62
6.4	Direct excitation process	62
6.4.1	Direct excitation: semi-empirical treatment	63
6.5	Thermal rotational and vibrational populations	65
6.6	Applications	67
6.6.1	Vibration	67
6.6.2	Rotation	71
6.6.3	Actinometry	73
6.7	Spectroscopic data	75
7	Fulcher α spectroscopy at FOMSCE	79
7.1	Introduction	79
7.2	Experimental setup	79
7.3	Interpretation of the molecular spectrum	82
7.3.1	Corona phase	82
7.3.2	Vibration	83
7.3.3	Rotation	85
7.4	Plasma characterization	89
7.5	Discussion	93
8	Treatment of iron archeological artifacts in a hydrogen plasma beam	95
8.1	Introduction	95
8.2	Corrosion	96
8.3	Reduction of oxides and chlorides	100
8.4	Diagnostics	101
8.5	Results	103
8.5.1	Elst samples	103
8.5.2	Platelets	106
8.6	Discussion	113
9	Conclusions	119
	References	121
	Summary	125
	Samenvatting	127
	Curriculum Vitae	130

General introduction

This thesis reflects the results of a study of the expanding cascaded arc plasma as a source for hydrogen ions and atoms. The expanding cascaded arc setup has been developed to serve as a plasma source for fast deposition of amorphous or cristalline carbon layers [1, 2, 3] and for amorphous silicon layers [4]. More fundamental research has been done on pure argon plasmas of this type [5, 6]. This type of setup combines the dissociative and ionizing power of a dense discharge, the cascaded arc source plasma, with the transport properties of a particle beam, the plasma expansion. A further advantage is that the source plasma is not influenced by the conditions in the low pressure reactor; as a consequence, the plasma beam characteristics can be controlled by the discharge settings of the source and of the low pressure chamber independently. This gives a large freedom in the choice of experimental conditions.

In the expanding cascaded arc deposition projects, studies were primarily aimed at the deposition of good layers, and not dedicated to the role of hydrogen in the plasma kinetics. Still in most experiments hydrogen gas is seeded into the argon source plasma, and even if no hydrogen is added, it is produced in the plasma beam in the dissociation of e.g. CH_4 or SiH_4 , and in subsequent wall association and desorption. Consequently, hydrogen kinetics in the plasma beam are relevant to the plasma beam deposition even if no hydrogen is seeded.

Here, pure hydrogen or hydrogen-argon plasmas are studied. At the foundation of this work lie a cooperation with SHELL Research France and a Euratom research program. The cooperation with SHELL was aimed at the development of a large flux hydrogen atom source. The scientific questions that came up during this initially technological work have stimulated the development of the new RF probe activated actinometry and catalized the insight in the recirculation of background gas in the reactor and its influence on the plasma beam. A spin-off of this work is the treatment of iron archeological artifacts as described in chapter 8. In the framework of plasma deposition, there is interest in atomic hydrogen as a selective etching medium for weaker bonds on deposited layers and for passivation of dangling bonds. The role of the hydrogen atoms in the dissociation of e.g. silane in plasma

beams may be underestimated so far, and even be more important than ions and electrons [7].

In the framework of a broad Euratom program on Neutral Beam Injection (NBI) for the heating of TOKAMAK plasmas, the use of the cascaded arc plasma as a hydrogen ion source has been investigated. In the course of this work, the importance of molecular kinetics and the internal energy of molecules has become evident. The anomalous fast recombination mechanism that is proposed in this thesis is expected to be important in any plasma where sufficient vibrationally and/or rotationally excited molecules are available. This is certainly the case in the expanding cascaded arc plasma setups as used at the Eindhoven University of Technology. A clear example of such a plasma may also be found in negative ion volume sources, that need high densities of vibrational excited molecules for negative ion formation. Another example is found in interstellar clouds, in which high vibrational temperatures are observed.

A short characterization of the source plasma and the plasma beam is given in the following.

Source plasma

The cascaded arc plasma is operated at high current densities (35-70 A through a 4 mm diameter channel) and at near-atmospheric pressures (0.1-1 bar). Under these conditions the coupling between electron and heavy particle temperature is good. The cascaded arc plasma has been studied extensively for argon gas operation. In that case the electron temperature and the heavy particle temperature both are ~ 1 eV. The ionization degree in the source plasma is around 5%. The high electron density, high heavy particle temperature and density and low electron temperature compared to most other discharges make that the plasma is strongly collision dominated. Radiative losses are relatively small and the energy efficiency for dissociation and ionization is high compared to other types of discharge.

When operated on hydrogen gas, a molecular component is added to the gas. The lighter mass of hydrogen compared to argon and the dissociation of molecules in the plasma and the re-association of atoms to molecules at the walls of the source give rise to an increased heat conductivity. Due to larger heat losses to the walls, at the edges of the plasma channel temperatures can be substantially lower in a hydrogen plasma than in the argon case. At the center of the cascaded arc source the conditions are still expected to be comparable to the argon plasma.

Plasma beam

The plasma beam has been studied intensively for argon plasmas. The hot source plasma expands into a low pressure chamber, 0.1 to 10 mbar background pressure. After a supersonic expansion and a shock, a subsonic plasma beam is obtained. This is the region that is studied here in more detail for hydrogen. The plasma beam has a low electron temperature (~ 0.3 eV) and an electron density of a few times 10^{17} to a few times 10^{19} m^{-3} . The plasma beam is a recombining plasma afterglow; no power input takes place. The electron temperature is far too low to make excitation of electronic states possible (all excited states have energies above 10 eV in hydrogen/argon plasmas). Yet the plasma emits a spectrum. The excited states that are observed in emission are populated by recombination processes from atomic or molecular ions. The emission spectrum consequently contains information on the ions in the plasma and not on the bulk of the neutral particles. The electron energy distribution function (EEDF) is still expected to be Maxwellian in most cases.

Outline of the thesis

The hydrogen cascaded arc setup is discussed in chapter 2. Here the relevant technical information for the construction and operation of the plasma machine on hydrogen gas is given. The application of the setup as an atomic hydrogen source is characterized in chapter 3. Here also the new RF probe activated actinometry technique is introduced. Chapters 4 and 5 are related to the molecular kinetics in the plasma. The anomalous fast recombination process that has been observed with Langmuir double probe measurements is described in chapter 4. Molecular processes leave their 'fingerprints' in the atomic Balmer emission spectrum. The emission spectroscopy is described in chapter 5. The interpretation of the molecular hydrogen plasma is subject to chapter 6. Molecular spectroscopy can yield information on the rotational and vibrational temperature and can be used to estimate the dissociation degree of the plasma. This chapter offers the theoretical basis for the active actinometry and for the molecular spectroscopy performed at AMOLF, Amsterdam. At AMOLF the emission spectrum of the plasma of the FOM Surface Conversion Experiment (FOMSCE) was measured (chapter 7. This work represents the link to the negative ion production in the framework of the Euratom program. The spectroscopic work also served as a pilot experiment for the interpretation of the molecular Fulcher spectrum. Chapter 8 deals with the treatment of iron archeological artifacts in a hydrogen plasma beam. This chapter describes the promising results of a survey program in the twilight zone between plasma physics, surface physics and archeology. The main conclusions of the preceding chapters are shortly summarized in chapter 9.

The experimental setup

The hydrogen plasma setup is based on the same concept as the Eindhoven plasma beam deposition machines [1, 4]: a cascaded arc thermal plasma source at moderate pressure (0.1-1 bar), expanding into a low pressure (0.1-50 mbar) vessel. The thermal plasma is efficient in the production of ions and radicals. The expansion into the low pressure chamber results in a fast plasma beam, that takes care of a directed transport of the reactive particles from the source to a target region. This concept has proven to be very succesful in the application of fast deposition of a:C-H and a:Si-H layers [2, 4].

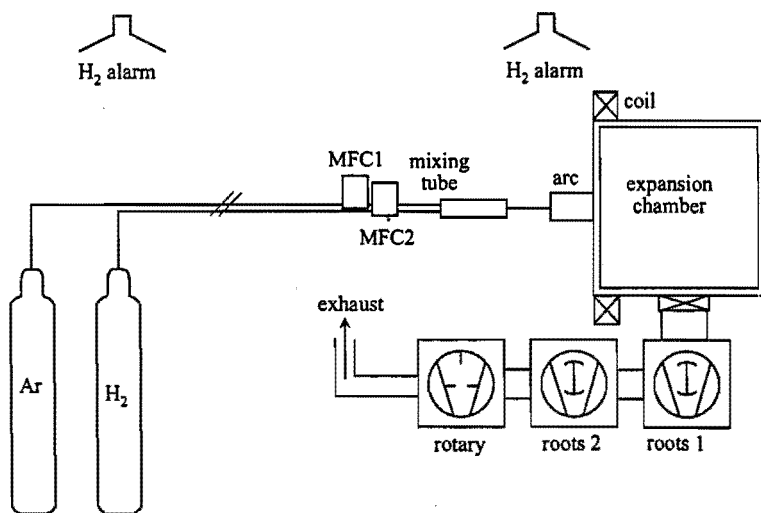


Figure 2.1. *The hydrogen plasma machine. MFC1 and MFC2 are the mass flow controllers for the argon and hydrogen gas feeding.*

In the hydrogen plasma machine the objective is a large flux of hydrogen ions, or, in other applications, hydrogen atoms. An overview of the plasma setup is given in Fig. 2.1. Indicated in the figure are the cascaded arc source, the gas feed system, the expansion chamber, the pumping system and the

hydrogen alarms. The plasma reactor and vacuum system are described in section 2.1. In order to be able to operate on large hydrogen fractions, modifications of the source were necessary. These are discussed in section 2.2. The operation of the plasma machine is subject to section 2.3. Here characteristics of the source like energy efficiency and heat load to the cascaded arc at varying hydrogen fraction in the plasma are given. Also items like stability and reproducibility of the plasma are addressed here. Hydrogen is a highly flammable and explosive gas. A hydrogen plasma machine therefore demands provisions to ensure safe operation, even in the case of malfunctioning of the system. Section 2.4 deals with this. Conclusions are summarized in section 2.5.

2.1 The expansion chamber

The plasma emanating from the cascaded arc source expands into the low pressure expansion chamber. This chamber is a cylindrical stainless steel vessel ($l=0.4$ m, $\varnothing=0.4$ m), with at the front and back side an aluminum circular flange. Flanges and chamber are water cooled. On the front side flange the cascaded arc source is mounted. A quartz window at the left side of the reactor allows spectroscopic measurements. Two other flanges at the top and right side are used to mount various diagnostic equipment. An MKS 122 A Baratron pressure transducer and a Balzers TPG 040 Pirani are used to measure the pressure in the reactor. The reactor is pumped by a line of two roots pumps and a rotary pump. The maximum pumping capacity is 1000 m³/hour and can be regulated by a valve between the low pressure chamber and the pumps. At full pumping capacity a pressure of ~ 0.4 mbar can be maintained at a gas flow of 3.5 standard liter per minute, which is the default gas flow. The pumping speed and therewith the pressure in the reactor can be regulated by a manually adjustable valve between the reactor and the pumps. The pumping speed of the vacuum system is equal for argon and hydrogen gas.

At the source side of the reactor, at the nozzle position, a magnetic field coil is mounted. The axial field strength as a function of position in the reactor is given in Fig. 2.2 (a). The shape of the magnetic field is seen in Fig. 2.2 (b). This magnetic field can be used to confine the plasma and thus increase the electron density in the plasma.

2.2 The cascaded arc source

The cascaded arc thermal plasma source is depicted in Fig. 2.3. It is of the same design as the one presented by Kroesen [3] for argon plasma generation, with some additional features to enable stable plasma operation on

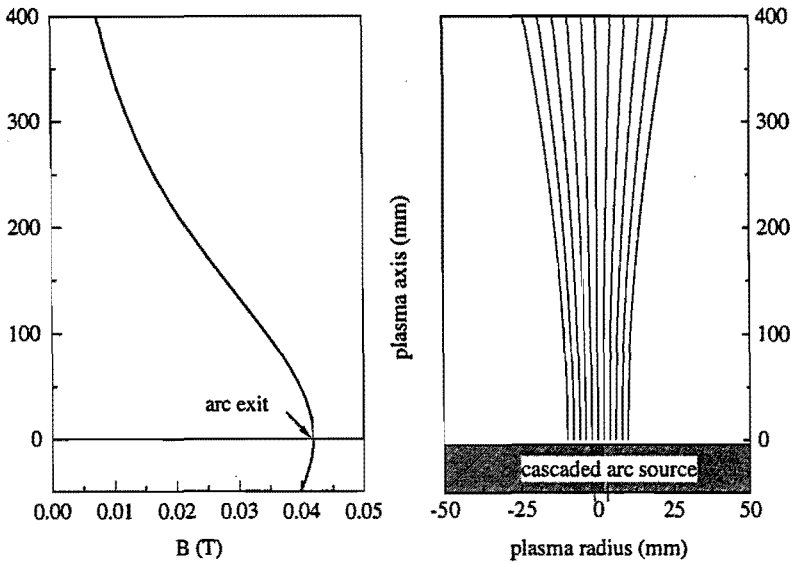


Figure 2.2. (a) The axial magnetic field strength at a coil current of 250 A. (b) Calculated traces of the magnetic field lines in the expansion chamber. The field is slightly divergent. The plasma beam emanates from the source at position $(0,0)$. Note that the horizontal and vertical scale are different in the figure.

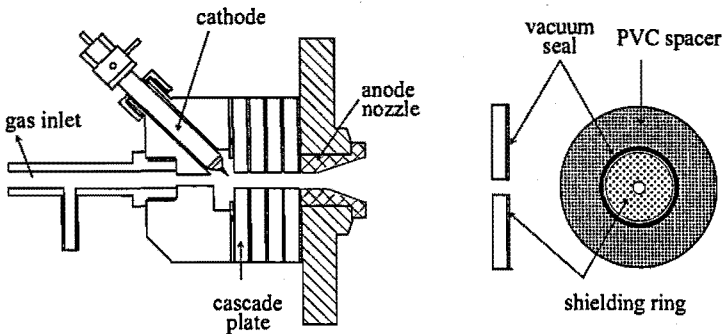


Figure 2.3. The cascaded arc source.

hydrogen gas. In the cascaded arc a discharge is sustained between three concentrically placed cathodes and an anode plate. The plasma is thermally confined by a stack of water-cooled copper plates with a central bore of 4 mm, forming a plasma channel. Thus a so-called wall-stabilized plasma is obtained. The plates are electrically isolated by polyvinylchloride spacing rings with a thickness of 1 mm. Inside these rings a Viton O-ring is mounted as a vacuum seal. These O-rings are protected from the plasma by shielding rings, made of boron nitride. The arc length can be varied by changing the number of cascaded plates.

Gas is fed in at the cathode side and the plasma can leave the source through a nozzle plug that is screwed into the anode plate. The argon and hydrogen gas flows are regulated by mass flow controllers. After the mass flow controllers the argon and hydrogen flows come together in a small cylinder (volume 0.5 l). In this cylinder the gases are mixed and are fed to the arc together. At the arc inlet also a Baratron pressure transducer is mounted. Without the mixing cylinder the plasma tends to go to a mode of operation in which the argon and hydrogen flows start oscillating and eventually the entire plasma may be seen to switch between a pure argon mode and an argon/hydrogen mode. The cylinder acts as a gas buffer and keeps the composition of the gas flow to the arc constant, and a stable plasma is obtained. In order to enable the operation of a plasma on hydrogen gas, furthermore the implementation of the cascaded arc is modified at a few points compared to the original design by Kroesen. A hydrogen plasma generally has a larger heat conductivity than an argon plasma, cf. Fig. 2.4, where an increase in power loss to the cooling water is seen with increasing hydrogen fraction. The available power supply did not allow higher hydrogen fractions than 56%. However, recent experiments by Qing [8] show that the results from Fig. 2.4 can be extrapolated linearly towards 100% hydrogen. All parts directly exposed to the plasma are therefore charged with a higher heat load. Therefore these parts are made quartz (shafts around cathode holders) or boron nitride (shielding rings) instead of teflon or polyvinylchloride as usual in the argon cascaded arc.

The cathode tips are getting much hotter too in hydrogen. If the default 1 mm cathode tips are used, a shower of metal droplets is observed in the plasma beam emanating from the source and the tips are eroded away completely within one hour. If the arc is to be used for hydrogen plasma thicker cathode tips are required. With 2 mm diameter tips and a proper starting and stopping of the plasma (cf. section 2.3) no sputtering is observed and the standing time of the cathodes is very long.

The operation voltage and consequently the electric field strength is also higher for a hydrogen plasma than for argon, cf. Fig. 2.5. This invokes the risk of discharges between cascade plates instead of through the plasma channel. To avoid this, the inner diameter of the boron nitride shielding

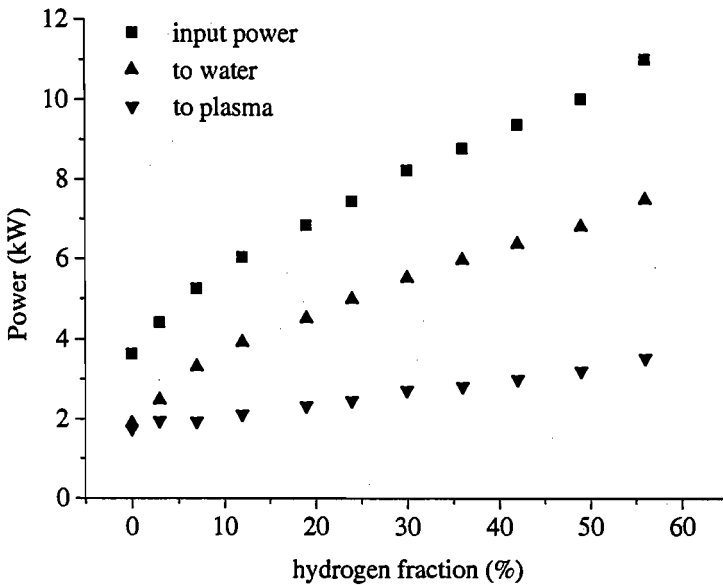


Figure 2.4. The heat balance for argon and hydrogen plasmas. Both the total power input and the heat loss to the cooling water are several times larger in a hydrogen plasma than in an argon plasma. Results are for a 10 plate cascaded arc. The discharge current is 45 A, the total gas flow is 3.5 slm.

rings reaches the plasma channel. It has been found empirically, that the top shielding ring, between the cathode holder and the first plate, must have a larger internal diameter (~ 10 mm) than the other rings. Furthermore sharp edges inside the source are rounded, in order to minimize electric field gradients.

Finally, it appeared that the shape of the nozzle has a large influence on the outflowing plasma in the case of hydrogen operation. A nozzle with a straight channel [1] produces a weak plasma beam. With a conical channel this improves, and a parabolically diverging channel yields the best results. This type of nozzle is used in all experiments. It is sketched in Fig. 2.3. The design of an optimized nozzle is beyond the scope of this work. Considerations in the nozzle design are discussed in e.g. [9].

There have been no dedicated experiments to determine the standing time of this cascaded arc. However, over the years it has not occurred that parts had to be replaced due to regular wear. The largest period of experiments without modifications on the arc lasted over 2000 hours. During this period the arc operation conditions were varied over a wide range of currents and gas flows, and the plasma has been started and extinguished hundreds of times. As the starting of the plasma is probably the most damaging part of the operation, it seems justified to conclude that the standing time of the

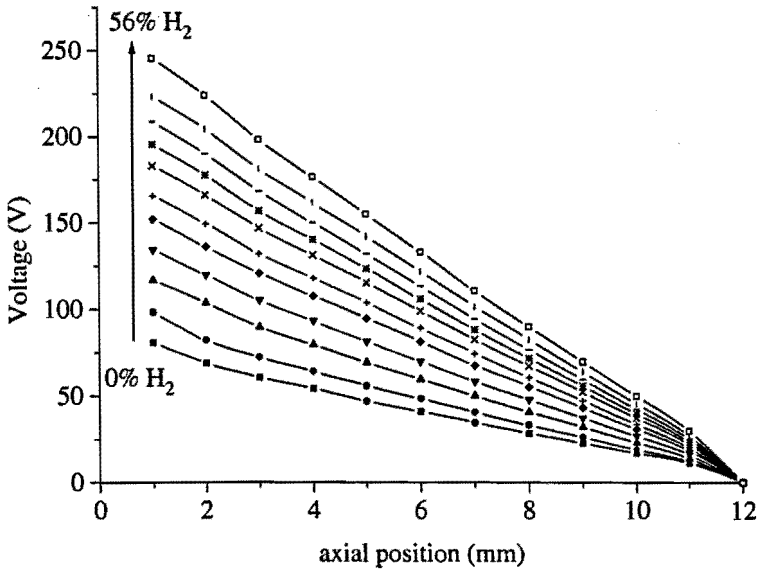


Figure 2.5. The voltage in the arc channel versus hydrogen fraction. The axial position is the distance from the cathodes. The operation voltage and consequently the electric field increases linear with the hydrogen fraction in the gas flow. The same plasma settings are used as in Fig. 2.4.

arc is by far more than 2000 hours.

2.3 Plasma operation

Most of the operation of the hydrogen plasma machine is PLC controlled. The plasma is started at argon gas. A high voltage, low current power supply starts a glow discharge with a current of ~ 1 mA for a period of 4 seconds. At the same time the main arc power supply is started. This is a slow start supply with a rise time of 1-2 seconds. This way a smooth start is obtained without a voltage or current overshoot. The electric scheme of the arc source is shown in Fig. 2.6. It appeared to be important to start on 100% argon, as even small traces of hydrogen present during starting result in damage of the cathodes. Before switching off the plasma, approximately 1 minute pure argon operation is applied to remove all hydrogen absorbed in the metal parts of the cascaded arc. This prevents damage in subsequent plasma startups.

Hydrogen gas feeding changes the operation characteristics of the source considerably. Fig. 2.7 shows the energy efficiency as a function of the gas ratio. This is the fraction of the energy input to the arc that is converted to the emanating plasma flow. The efficiency decreases from approximately 50%

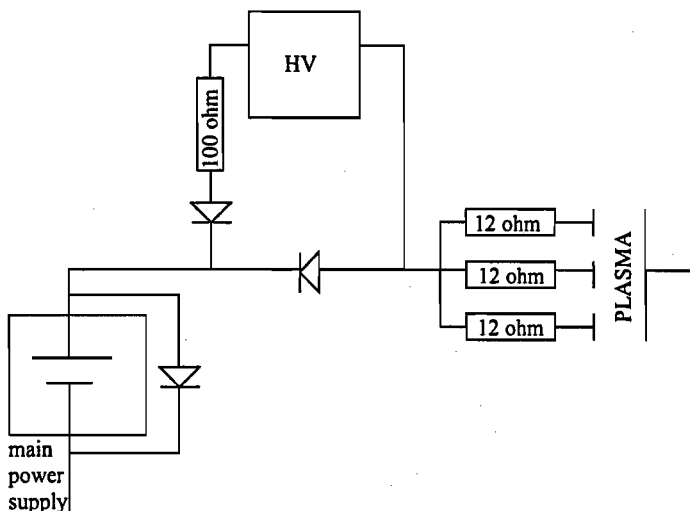


Figure 2.6. Electric scheme of the cascaded arc source. A glow discharge is started with the high voltage power supply HV. The arc power supply then takes over and starts the higher current arc discharge. The resistors of 12 Ω in line with each cathode help to stabilize the discharge.

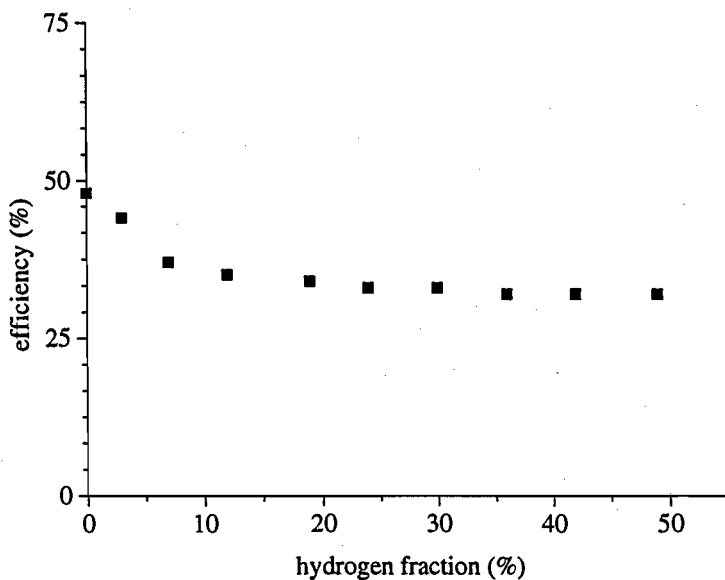


Figure 2.7. The energy efficiency -the fraction of the ohmic power input that is ends up in the outflowing plasma- versus the hydrogen fraction. The same settings as in Fig. 2.4 apply.

for full argon to 35% for hydrogen. Evidently the larger heat conductivity of the hydrogen plasma leads to more energy loss. The efficiency decreases until a hydrogen seeding fraction of $\sim 7\%$ is reached and then remains nearly constant. At the same seeding fraction, in the plasma beam, emanating from the source, the argon spectral lines have disappeared from the emission spectrum. The latter indicates in a recombining plasma that there are no argon ions left. This suggests that the ions play a central role in the heat loss to the walls of the arc channel. The ambipolar diffusion is larger for hydrogen than for argon due to the smaller ion mass.

Another effect is that the viscosity of a hydrogen plasma is much lower. At equal gas flows therefore the pressure at the inlet side of the cascaded arc is much lower in the latter case. This is seen in Fig. 2.8. An important

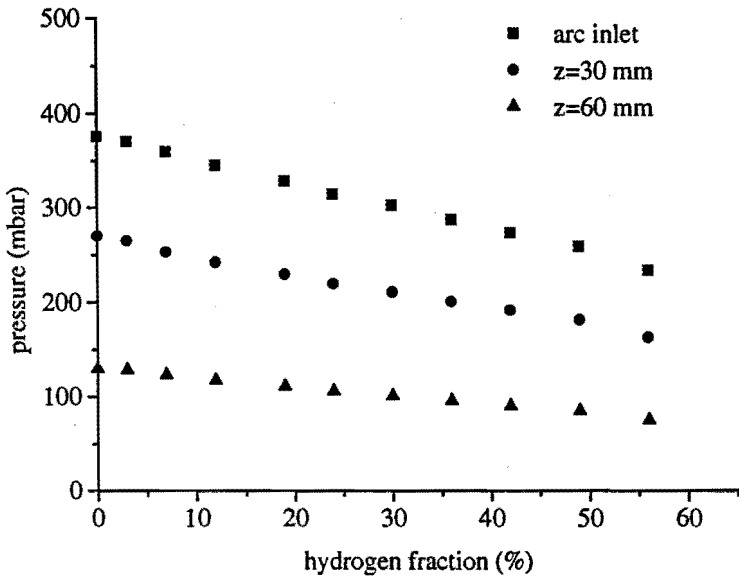


Figure 2.8. *The arc pressure at inlet, halfway the arc and at the anode as a function of hydrogen fraction in the plasma.*

feature of the cascaded arc source is the stability of the plasma. In general arc discharges tend to show poor stability and/or reproducibility. Comparing a cascaded arc discharge to conventional arc discharges with similar power density and gas flows, an important difference is that the arc in the cascaded arc is longer, and the same power input is obtained at a lower current and a higher voltage. Consequently the influence of the cathodes on the total arc behaviour is small. As instabilities occur especially in the cathode region, this improves the overall stability of the source. The stability of operation is further improved by the addition of resistors in line with the cathodes, cf. Fig. 2.6.

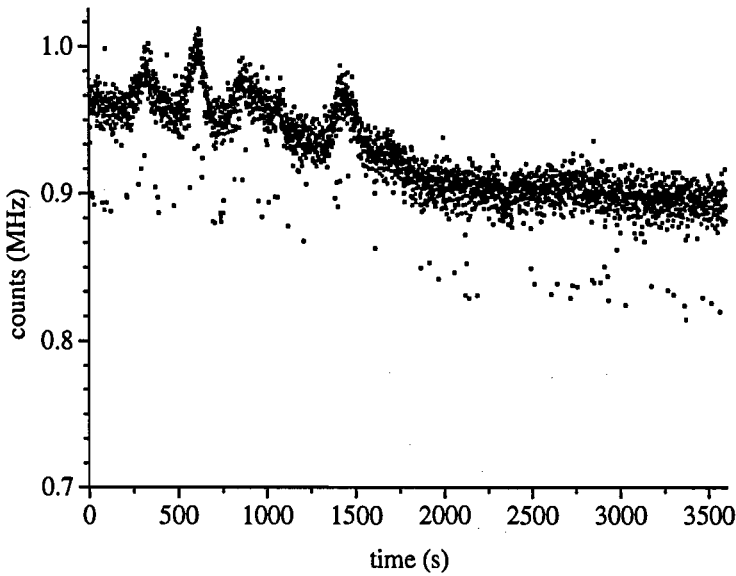


Figure 2.9. The intensity of the H_{β} spectral line versus time after plasma startup.

The stability and reproducibility of the plasma have been measured for on the intensity of the hydrogen H_{β} spectral line. The intensity is measured in the expansion chamber at an axial position 24 cm downstream the plasma source. Plasma settings are 20% atomic hydrogen in a total gas flow of 3.5 slm, discharge current 65 A, pressure 0.5 mbar and a coil current of 250 A. The sample time was 1 second, equal to the sample time in spectroscopic measurements. Fig. 2.9 shows the measured intensity of the H_{β} spectral line in the first hour after plasma startup. The figure shows that during the first half hour the intensity is slowly increasing and then remains constant within an error of 5%. The initial drift can be attributed to warming up of the arc power supply. It is observed that the discharge current setting drifts during this initial period. Fig. 2.10 concerns the reproducibility of the plasma system. It shows the intensity of the H_{β} line over a few runs. Between two runs, the plasma is switched off and all gas flows are put to zero. The power supply is kept at standby, to avoid the above mentioned warming up time. Then the plasma is restarted, and all settings are restored. Between the second last and last measurement the entire vacuum system was shut down, the reactor was pressurized and the cathodes were replaced. The latter was to study the influence of cathode condition and alignment. It is evident from the figure that the signal reproduces within 5% in all cases.

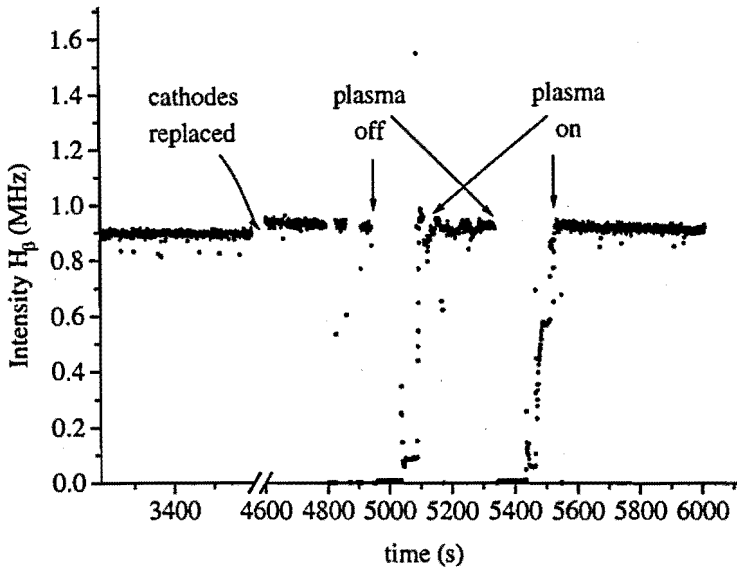


Figure 2.10. The intensity of the H_{β} spectral line during several plasma runs. The same plasma settings as in Fig.2.9 apply. Between two plasma runs, the plasma has been switched off and all flow and current settings have been set to zero. Before the last run, the arc source was dismantled and the cathodes were replaced.

2.4 Safety considerations

Hydrogen is a highly flammable and explosive gas and therefore requires safety measures. In the current setup, an important consideration in the safety strategy is that the amount of hydrogen in the system is small at all times: the volume in the gas feeds at the high pressure side is very small and the pressure in the reactor is in the order of 1 mbar under plasma conditions. If therefore a hydrogen alarm situation occurs, shutting down the system immediately eliminates a dangerous situation in the system. The system is shut down if one of the hydrogen detectors gives alarm - there is a detector above the gas bottles and one above the source, see Fig. 2.1 -, if the gas exhaust system fails, at malfunctioning of any part of the vacuum system or if an alarm button is hit. The gas exhaust system starts at the high pressure side of the pumps. Gas from the plasma machine is mixed with a large volume of air in a grounded metal mixing piece to values far below the flammability limit of hydrogen. A ventilator with a capacity of $800 \text{ m}^3 \text{ hour}^{-1}$ takes care of this.

2.5 Conclusions

When the $H^{+/-}$ project was started, operation on high hydrogen seeding fractions or even full hydrogen was expected to be difficult. It has appeared, however, that only minor modifications on the argon cascaded arc design used by Kroesen [1] were needed to obtain a reliable hydrogen plasma source. Necessary modifications are related to the higher electric field and the larger heat load in the source, if operated on hydrogen. With this modifications and a careful plasma starting and stopping procedure, the cascaded arc is a plasma source with a very long ($\gg 2000$ hours) standing time that produces a stable plasma beam. An important factor in the stability are the cascaded arc plates. These yield a long and stable arc, diminishing the relative influence of instabilities in the cathode region on the total arc behaviour.

3

Atomic hydrogen source featuring recirculation

3.1 Introduction

Atomic hydrogen is an important species in numerous plasma chemical applications. Examples are found in plasma deposition of a-C:H and a-Si:H layers, where the hydrogen radicals abstract or passivate dangling bonds during deposition [1, 4]. Another application is described in chapter 8: the treatment of iron archaeological artifacts. The number of chemical bulk processes in which atomic hydrogen could be used is enormous. As an example, the work subject to this chapter was started in cooperation with SHELL Recherche, France, with the aim to develop an efficient atomic hydrogen source for use in volume chemical processes. For application in bulk processes economic considerations are important. Therefore the energy efficiency of the source and the dissociation degree of the feeded gas are important features. Section 3.2 describes the cascaded arc characteristics. These have been estimated for the produced plasma from the heat balance in the source.

The dissociation degree has also been determined downstream the plasma beam in the low pressure reactor. Hereto a new diagnostical technique was developed, RF excited active actinometry. This technique and results for the plasma beam are found in section 3.3.

The dissociation degree that was measured downstream the plasma beam is found to be significantly lower than that at the exit of the source. In section 3.4 it will be argued that recirculation processes in the reactor, mixing background gas with the plasma emanating from the source, have an important influence on the plasma beam characteristics.

The relation between the source plasma, the plasma beam and the recirculation process are discussed in section 3.5.

3.2 The plasma source

The cascaded arc source is described in detail in chapter 2. For the atomic hydrogen source application subject to this chapter the number of cascade plates was 3 or 4. The source has been operated on hydrogen gas flows of 3, 6 and 9 slm at two different discharge currents, 35 and 50 A. The heat loss of the plasma to the cooling water was measured for the cathodes, the anode and for each cascade plate. The heat loss was measured by an array of water flow meters and temperature sensors at the inlet and outlet side of the cooling water channels. The Ohmic input power along the plasma axis was determined from the arc current and the voltage at each part of the arc. The experimental setup that has been used for the characterization of the cascaded arc plasma is sketched in Fig. 3.1. In the following the energy effi-

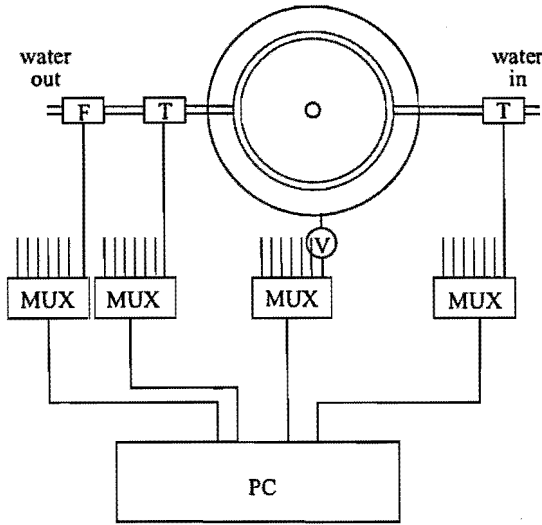


Figure 3.1. Schematic representation of the setup used for the characterization of the cascaded arc plasma. The voltage is measured at the cathodes and at each cascade plate. The water flow to each part is measured with a flow meter at the water inlet side. The water temperature is measured at the inlet and outlet side of the cooling channels of the cathodes, each plate and the anode separately.

ciency, the dissociation degree, and the ionization degree are defined. With these definitions a relation between the Ohmic input power, the gas flow and the dissociation and ionization degree is established. The energy efficiency η is defined by

$$\eta = \frac{P_{\text{plasma}}}{P_{\text{Ohmic}}} = 1 - \frac{P_{\text{cool}}}{P_{\text{Ohmic}}} \quad (3.1)$$

where P_{plasma} is the power which is effectively coupled into the plasma, P_{Ohmic} the Ohmic input (total electric power input) and P_{cool} the heat loss to the

cooling water. The efficiency is determined for the cathode, anode and each plate. P_{Ohmic} is calculated from the arc current and the voltage drop between adjacent plates. P_{cool} is determined by measuring the water flow and the increase in temperature of the cooling water.

The dissociation degree of the particle flow leaving the cascaded arc is defined by

$$\beta = \frac{\Phi_H}{2\Phi_{H_2}^0} \quad (3.2)$$

where Φ_H is the atomic hydrogen particle flow and $\Phi_{H_2}^0$ is the molecular gas flow at the arc inlet. This is the fraction of the incoming hydrogen atoms that is not bound in molecules but exists as free radicals.

The ionization degree is in a similar way defined in relation to the inlet gas flow,

$$\alpha = \frac{\Phi_{\text{ion}}}{2\Phi_{H_2}^0} \quad (3.3)$$

with Φ_{ion} the total ion flow.

Starting from the analysis of the energy balance analysis, an upper and lower limit for the dissociation degree can be estimated. The power that is effectively coupled into the plasma is used to heat, dissociate and ionize the hydrogen content,

$$P_{\text{plasma}} = P_{\text{heat}} + P_{\text{diss}} + P_{\text{ion}} \quad (3.4)$$

Note that only atomic ions are considered as the high electron density in the plasma guarantees immediate destruction of molecular ions by dissociative recombination. The four terms at the right hand side will be regarded successively.

An upper limit estimate of the energy needed for heating is made as follows. Consider the thermal energies of the different species, molecules, atoms, ions and electrons,

$$P_{\text{heat}} = \Phi_{H_2} \cdot \frac{5}{2} k\Delta T_{H_2} + \Phi_H \cdot \frac{3}{2} k\Delta T_H + \Phi_i \cdot \frac{3}{2} k\Delta T_i + \Phi_e \cdot \frac{3}{2} k\Delta T_e \quad (3.5)$$

The average temperature of the molecules leaving the arc is certain to be below 0.4 eV (4500 K) because above this temperature dissociation is almost complete, cf. table 3.1. In the periphery of the arc, near the cold walls, molecules can still exist. The atoms, ions and electrons are assumed to be at an average temperature of 1 eV (11500 K). This is a typical temperature for the hot center of the plasma channel [10]. In this treatment the kinetic energy, that is carried in the plasma flow, is not separately accounted for. Calculations by Vallinga [11] show that the flow velocity is < 0.2 Mach number in the first 90% of the plasma channel. At this position the plasma has almost reached its final composition. If the temperatures in Eq. 3.2 are considered to be stagnation temperatures, an estimated error of 10% is made here.

The power used for dissociation is presented by

$$P_{\text{diss}} = 2 \cdot \beta \cdot \Phi_{\text{H}_2}^0 \cdot E_{\text{diss}} \quad (3.6)$$

where $E_{\text{diss}}=2.3$ eV is the dissociation energy per atom, so half the energy needed to dissociate a molecule. For ionization the expression is similar,

$$P_{\text{ion}} = 2 \cdot \alpha \cdot \Phi_{\text{H}_2}^0 \cdot E_{\text{ion}} \quad (3.7)$$

Here $E_{\text{ion}}=13.6$ eV is the ionization degree. Combining Eqs (3.2) - (3.7) and substituting the dissociation energy per atom 2.3 eV and the ionization energy 13.6 eV the following expression is obtained:

$$\frac{P_{\text{plasma}}}{\Phi_{\text{H}_2}^0} = 1 + 6.5\beta + 34.5\alpha \quad (3.8)$$

where the power is given in eV/sec and the flow in particles/sec. Equation

T (°C)	H ₂	H	H ⁺
300	$2.7 \cdot 10^{19}$		
1000	$8.1 \cdot 10^{18}$		
2000	$4.1 \cdot 10^{18}$	$6.5 \cdot 10^{15}$	
3000	$2.3 \cdot 10^{18}$	$3.9 \cdot 10^{17}$	
4000	$4.7 \cdot 10^{17}$	$1.5 \cdot 10^{18}$	
5000	$3.7 \cdot 10^{16}$	$1.6 \cdot 10^{18}$	
6000	$5.1 \cdot 10^{15}$	$1.3 \cdot 10^{18}$	$8.1 \cdot 10^{13}$
8000	$3.5 \cdot 10^{14}$	$1 \cdot 10^{18}$	$2.5 \cdot 10^{15}$
10000	$6.8 \cdot 10^{13}$	$7.7 \cdot 10^{17}$	$1.9 \cdot 10^{16}$
12000		$5.3 \cdot 10^{17}$	$7.1 \cdot 10^{16}$
14000		$2.8 \cdot 10^{17}$	$1.5 \cdot 10^{17}$
16000		$1.1 \cdot 10^{17}$	$2.0 \cdot 10^{17}$
18000		$3.5 \cdot 10^{16}$	$2.1 \cdot 10^{17}$
20000		$1.2 \cdot 10^{16}$	$2.0 \cdot 10^{17}$

Table 3.1. Hydrogen plasma composition as a function of temperature. Densities are calculated values per m³ at a total pressure of 1 bar.

(3.8) establishes a relation between the ionization degree and the dissociation degree of the plasma.

In order to be able to estimate the dissociation degree of the plasma, according to Eq. (3.8) the ionization degree must be known. Here an upper and lower limit of the ionization degree are made. These yield a low and a high estimate of the dissociation degree. It will be seen that the relative difference between these two values does not exceed 20%.

Table 3.1 shows that in full equilibrium plasma ionization only occurs after full dissociation has taken place. However, in the cascaded arc there is no thermal equilibrium over the plasma radius. To be able to estimate a dissociation degree, according to Eq. (3.8) the ionization degree must be known. For a lower limit estimate, a comparison with an argon plasma at similar circumstances can be made [10]. In the arc center the temperature is 1 eV as well in argon as in hydrogen. There the ionization degree is typical 5-10% and for molecular gases the dissociation is complete. The situation is different closer to the wall; in monoatomic gases the T_e profile is rather flat and only close to the wall a transition layer occurs. In hydrogen however the conductive high T_e plasma channel is considerably smaller due to heat conduction. In the now extended wall layer a substantial residual molecule density may exist; this in fact is the very reason why the dissociation degree is not 100%. Hence the smaller the central hot channel the more escape of molecules and the smaller the average ionization degree averaged over the arc exit area. A first information on the effective surface of the central, ionized channel comes from the plasma resistance. The conductivity in the plasma is only high in the central, high T_e channel. Here it is governed by Coulomb e-i scattering and is proportional to $T_e^{3/2} \ln \Lambda$, in which Λ is the Coulomb logarithm [12]. As the electron temperature is 1 eV both for argon and hydrogen the change in resistance is fully caused by a change of the cross section of the conducting channel, i.e. the hot plasma center. Experiments show a four times larger voltage drop in a hydrogen plasma than in an argon plasma. For the overall ionization degree in a hydrogen plasma this would mean a four times smaller value than in a corresponding argon case. As a safe high estimate only a factor two lower ionization is taken. This allows for a somewhat higher value of the axial electron density in the hydrogen case. At the used flows, the cross section averaged ionization degree for argon is less than 5%. For the hydrogen case the lower limit of the calculated dissociation degrees and atomic hydrogen flows are obtained by assuming 2.5% ionization, the higher limit by assuming a negligible contribution of ionization.

3.2.1 Results

Fig. 3.2 shows for a three and a four plate arc the total Ohmic input power, the heat loss to the cooling water and the power that remains in the plasma, all as a function of flow. At increasing flow the Ohmic input power increases. This increase goes fully to the plasma; there is no significant increase in heat loss to the cooling water. At the higher current, 50 A, the magnitudes of the Ohmic input, of the heat loss and of the remaining power to the plasma all are higher than at 35 A. The ratios between these three quantities however does not change significantly. More current therefore means a higher power input without a change in efficiency. Fig. 3.3(a) shows the efficiency according

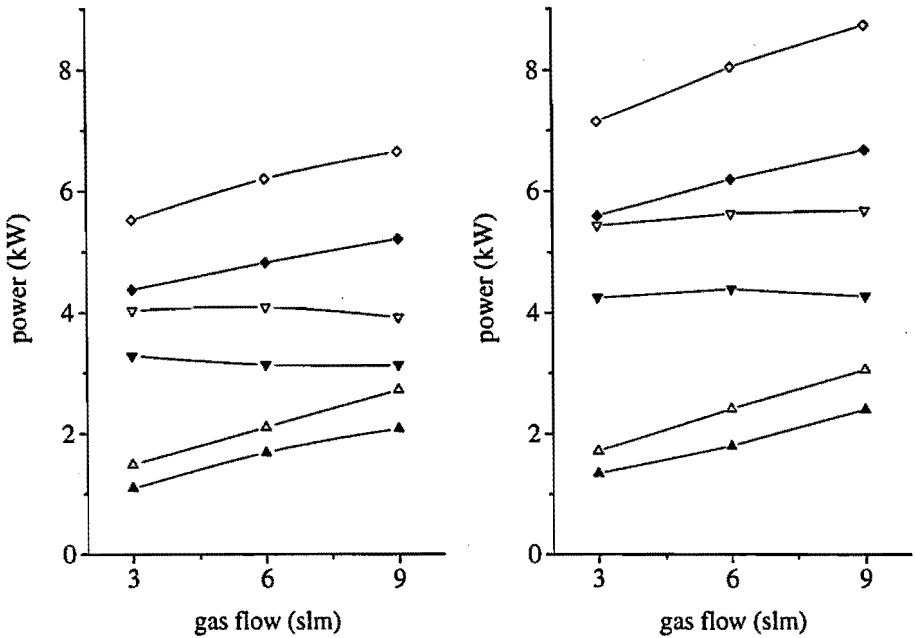


Figure 3.2. The power balance in the source for (a) a three plate arc and (b) a four plate arc. The open markers correspond to a 50 A plasma current, the closed markers to 35 A. The diamonds represent the total Ohmic power input to the source, the down triangles to the heat loss to the cooling water and the up triangles to the power that remains in the plasma.

to Eq. (3.2) calculated from the data of Fig. 3.2. It shows an increasing efficiency at increasing gas flow. The four plate arc shows a lower efficiency than the shorter one. The influence of the current is not significant. The dissociation degree, calculated from Eq. (3.8) is given in Fig. 3.3 (b). It shows that at the lowest flows the dissociation degree has the highest values. The power input per slm hydrogen gas is then maximum. The point in Fig. 3.3 (b) that indicates full dissociation is for some reasons inaccurate: first, the efficiency is very low and therefore the determination of P_{plasma} is inaccurate. Second, at such low flow and high power input the ionization degree of the plasma may exceed the estimated maximum of 2.5%. The atomic hydrogen flow emanating from the cascaded arc source is plotted versus gas flow in Fig. 3.4 for a three and a four plate cascaded arc. It shows that although the dissociation degree is highest at low gas flows, this fact is more than compensated for by the larger gas flow; maximum H^0 flow is reached at high flow and high current.

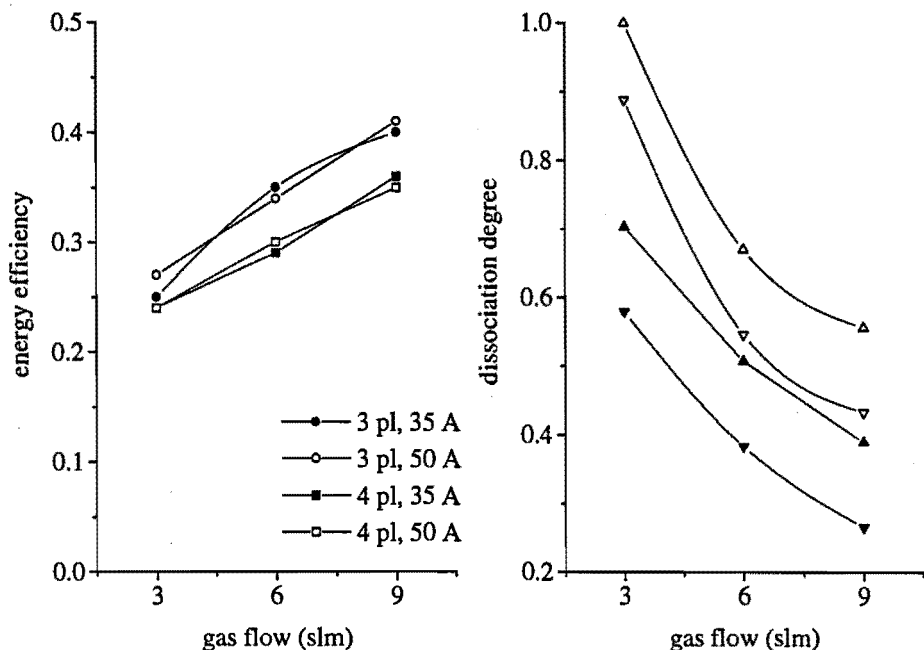


Figure 3.3. (a) The energy efficiency of the source for the 3 and 4 plate arc. (b) Upper (triangles up) and lower (triangles down) estimate of the dissociation degree of the plasma emanating from the source. Open markers correspond to the 50 A plasma current, solid markers to 35 A.

The efficiency of the cascaded arc as an atomic hydrogen source increases with increasing gas flow and current. The four plate arc gives a higher dissociation degree than the three plate arc, however, the efficiency goes down. Therefore, to obtain a higher dissociation degree, an increase in current is more appropriate than an increase in arc length. If the primary goal is to obtain a high dissociation degree and energy efficiency is not important, a longer arc is an alternative to high current operation. This situation might for example occur if an atomic beam is needed for research applications.

Finally, it is mentioned that at lower gas flows the ionization degree is expected to be higher than at higher gas flows. As a consequence, it is likely that the dissociation degree at low gas flows is closer to the estimated lower limit (2.5% ionization assumed) and at high gas flow closer to the estimated no ionization limit.

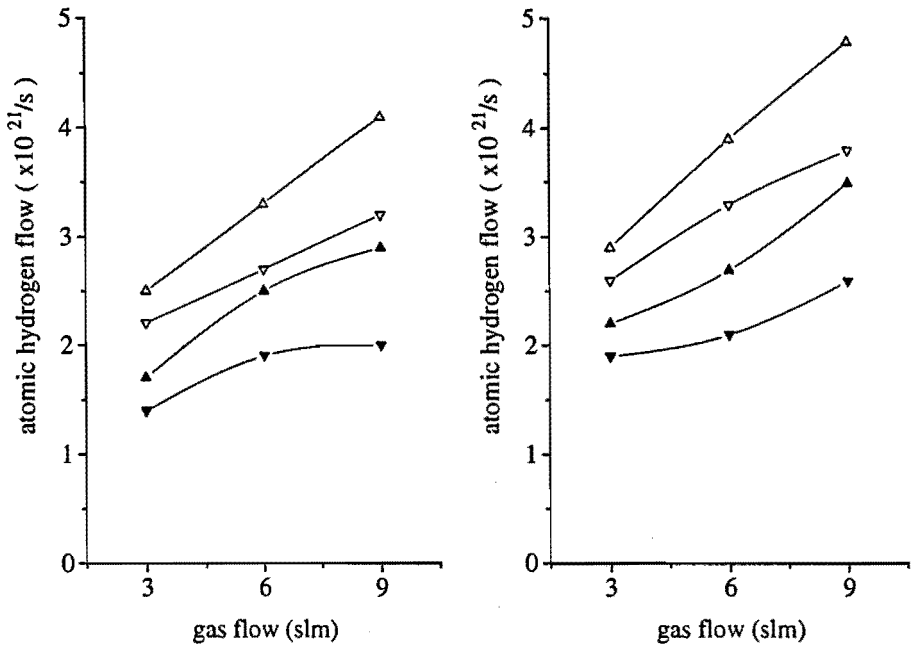


Figure 3.4. The atomic hydrogen flow from the cascaded arc source for the three (left) and four (right) plate arc. Again open markers indicate $I=50$ A, closed markers $I=35$ A. Triangles down correspond to the lower estimate, up to the higher estimate.

3.3 Plasma beam

The dissociation degree has also been measured in the plasma beam at a position of 25 cm downstream of the source exit. Hereto a new diagnostic was developed and implemented, based upon actinometry on the atomic Balmer H_α ($H(n=3) \rightarrow H(n=2)$) and the molecular Fulcher α ($d^3\Pi \rightarrow a^3\Sigma$) spectrum. If actinometry is to produce information on the ground state densities of atoms and molecules, it is required that the levels that are observed in emission are populated by direct electron impact excitation from the ground state. The electron temperature in the recombining plasma beam is low, ~ 0.3 eV, too low to deliver a significant excitation of ground state atoms ($E_{H(n=3)} = 12.1$ eV), or molecules $E_{d^3\Pi} = 14$ eV). Therefore an active method is required. Here RF excited active actinometry is introduced. In the plasma beam a RF probe exciter is placed, that locally heats the electrons. The electron temperature is increased enough to produce excited atomic and molecular states that can be observed in emission. The RF probe setup and

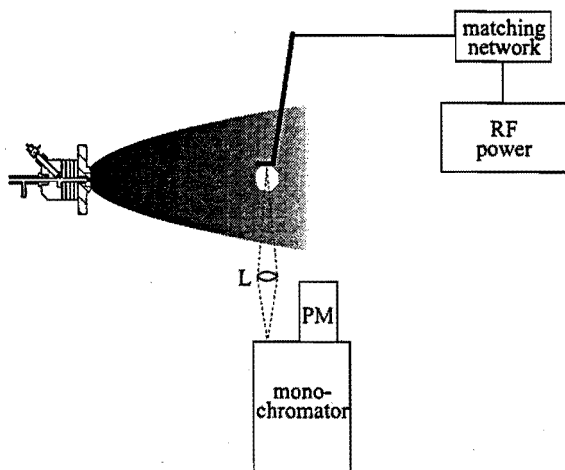


Figure 3.5. The RF excited actinometry setup. The probe surface is a thin stainless steel platelet, 20×10 mm, with rounded edges. The probe is placed 25 cm from the source exit, with the length axis of the platelet aligned to the plasma axis.

spectroscopic system are depicted in Fig. 3.5. The RF power is kept at ~ 15 W during the experiments. The intensity of the emitted light increases

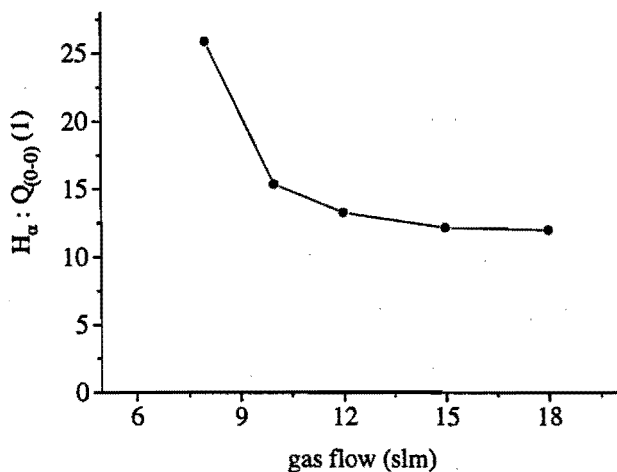


Figure 3.6. The ratio of the atomic H_α to the molecular $Q_{(0-0)}(1)$ spectral line as a function of applied RF power.

with the applied power. The ratio of atomic-to-molecular light as a function of power is given in Fig. 3.6. Between 10 and 20 W this ratio shows a slight decrease. If the RF probe changes the dissociation degree of the plasma,

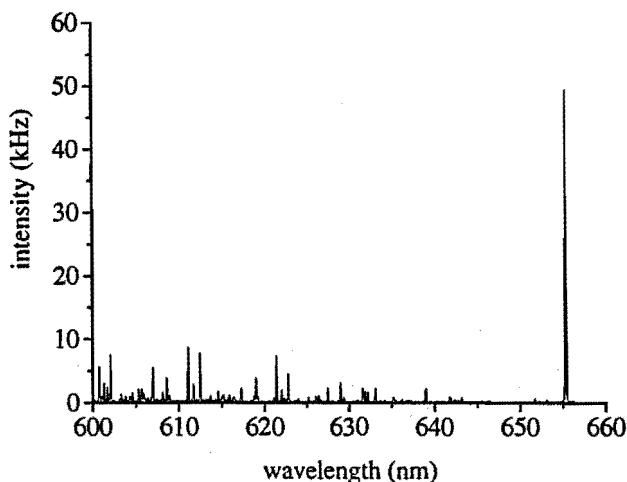


Figure 3.7. A recorded spectrum from the RF probe excited plasma.

an increase with applied power must be expected. From this observation is concluded that the plasma dissociation degree is not significantly influenced by the RF probe. The obvious decrease of the atomic-to-molecular emission below 10 W may correspond to an increase in electron temperature, as will be argued later.

Under the experimental conditions during the here presented measurements, the plasma beam hardly emitted any light. If the RF power was switched on, a bright plasma plume with a diameter of approximately 2 cm was observed. Fig. 3.7 shows an example of a recorded spectrum. A relation between the atomic and molecular densities on the one hand and the observed intensities of the atomic line and the molecular band on the other, is established in chapter 6:

$$\frac{I_{H_{pq}}}{I_{n'n''}} = \frac{n_H}{n_{H_2}} \times \frac{A_{pq} \tau_{rad}}{\sum_{v^0} q_{v^0 v'} q_{v' v''} \frac{Q'_{rot}}{F'_{rot}(K')}} \times \frac{\sigma_p^{max}}{\sigma_{F_a}^{max}} \times [1 + C_{thr}(\varepsilon)] \quad (3.9)$$

Here A_{pq} is the radiative transition probability for a transition $p \rightarrow q$, and τ_{rad}^p the radiative lifetime of the excited level p . Values for these parameters are taken from [13]. The Franck-Condon factors $q_{v^0 v'}$ and the atomic and molecular cross sections σ_p^{max} and $\sigma_{F_a}^{max}$ are found in chapter 6. The term F'_{rot}/Q'_{rot} was calculated for a rotational temperature of ~ 1300 K, that was determined from the rotational spectrum following the procedure described in chapter 6. The value for the correction factor $C_{thr}(\varepsilon)$ that accounts for the difference in threshold energy for excitation of the atomic and molecular lines is calculated from Eq. (6.47) for an electron temperature of 4 eV. The dissociation degree has been measured on the plasma beam axis 25 cm

downstream the source as a function of the gas flow, Fig. 3.8. In the same figure the dissociation degree as determined at the arc exit from the power balance is plotted. Apparently the dissociation degree is significantly lower

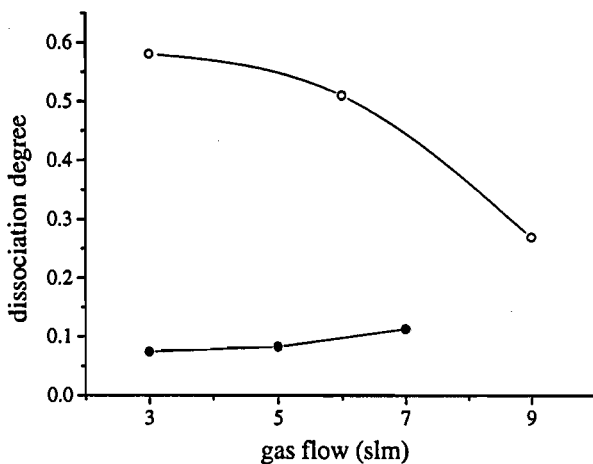


Figure 3.8. The dissociation degree in the plasma beam determined with active actinometry 25 cm downstream the source (•), and determined from the power balance at the source exit (o). Plasma settings are 3 slm H_2 as flow, arc current 35 A.

in the plasma beam than in the plasma emanating from the source (cf. Fig. 3.3). Furthermore in the plasma beam there is a (weak) positive correlation between the gas flow and the dissociation degree, whereas in the source the opposite is the case. It will be argued in the next section, that recirculation of background molecular gas has an important influence on the plasma beam characteristics.

3.4 Recirculation

Understanding the discrepancy between the dissociation degree measured in the source and in the plasma beam requires a closer look at the transport of the plasma in the expansion chamber. In the following an order-of-magnitude discussion will be presented, that is of value for a wider range of experimental conditions. The transit time of the plasma from the source exit to the back wall of the chamber depends on settings as gas flow and pump speed, but is in the order of 0.5 ms. The average residence time of a particle in the expansion chamber is much longer: at a gas flow of 3 slm, a background pressure of 0.5 mbar, and an average background gas temperature of 600 K the 50 liter chamber will be refreshed every 0.2 s. Therefore, by comparing these two transport times it is concluded that particles have many recirculations

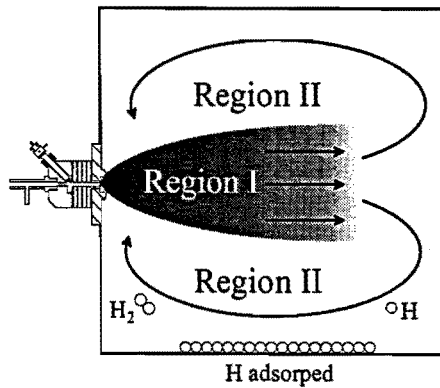


Figure 3.9. A schematic model of the flow in the reactor. The plasma beam flows through region I, the gas flow returning from the back wall recirculates through region II. Region II is the surface of a cross section of the reactor minus the plasma beam cross section.

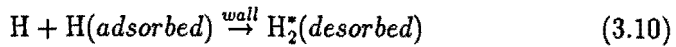
before they are pumped away. Moreover, seeding of background gas in the main plasma flow must be considered. A schematic model of the flow in the reactor is depicted in Fig. 3.9. The region through which the plasma beam flows is annotated region I, the background area region II. If the pumping is neglected for the moment ($\tau_{res} \gg \tau_{transit,recirc}$) a gas flow through region I to the right must be compensated by an equal gas flow in the opposite direction through region II. The ratio of region I to region II is estimated $\propto 1/10$ from visual information of the plasma beam size. The recirculation time consequently is 10x larger than the transit time, but still one or two orders of magnitude less than the residence time. Particles will therefore recirculate many times before being evacuated from the reactor. Typical transport times are listed in table 3.2. Besides this, hydrogen atoms will be

$\tau_{transit}$	$\tau_{recirculation}$	$\tau_{residence}$
0.5 msec	5 msec	0.2 sec

Table 3.2. Transport times in the expansion chamber

able to 'see' the walls frequently before they are evacuated to the pumps. On metal walls an atomic hydrogen layer is adsorbed. The sticking probability of a hydrogen atom can be up to 1 on a clean metal wall. Eventually, if an incoming hydrogen atom hits an adsorbed atom, association may occur and a molecule can be desorbed. Resuming, atomic hydrogen is very likely to be adsorbed at the walls and by associative desorption it will come off as

molecular hydrogen, cf. Eq. (3.10):



The hydrogen molecules coming from the walls are rovibrationally excited [14, 15, 16]. The consequences of this rovibrational excitation for the ionization degree will be dealt with in chapter 4. In chapter 5 the possible impact on the plasma emission is discussed. For the proceeding of this chapter, the rovibrational excitation of the molecules is not important, and will be ignored.

In the region 20 to 30 cm downstream the source the plasma composition is already dominated by the background gas. As an example, for a hydrogen gas flow of 3 slm the plasma is expected to be nearly fully dissociated at the source exit (cf. Fig. 3.3), whereas the measured dissociation degree at $z=25$ cm is $\sim 10\%$. If the background gas is assumed to be fully molecular, at $z=30$ cm the plasma is a mixture of 10% source plasma with 90% background gas.

Another experiment has been performed to investigate the importance of recirculation. An argon plasma beam is exposed to hydrogen puffs of 100 μsec of hydrogen gas. The setup for this is sketched in Fig. 3.10. The effect

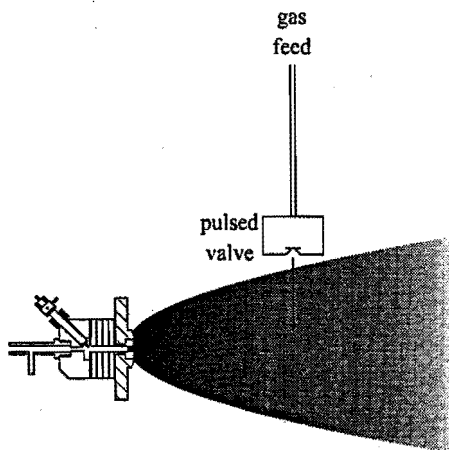


Figure 3.10. *The experimental setup for the pulsed valve experiments.*

of the hydrogen puffs on the argon plasma has been studied by emission spectroscopy on the hydrogen Balmer H_α line, the argon 696.5 nm spectral line and by a Langmuir probe. Experimental conditions are tabulated in table 3.4. Although a hydrogen plasma and an argon plasma are not entirely comparable, still these experiments can give a good indication of the effect

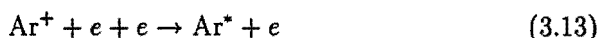
Plasma settings		Pulsed valve settings	
Φ_{Ar}	3.5 slm	pulse time	100 μ sec
I_{arc}	40 A	pulse frequency	10 Hz
p_{back}	0.4 mbar	$\Phi_{H_2}^{peak}$	10 slm
n_e	$\sim 10^{19} \text{ m}^{-3}$	$\Phi_{H_2}^{mean}$	0.01 slm

Table 3.3. *Experimental conditions for pulsed valve experiments*

of background molecular hydrogen on a plasma beam. The excitation of the H_α line occurs through the reaction



the excitation of the Ar line through 3 particle recombination



The effect of a hydrogen puff on the intensity of the H_α line is shown in Fig. 3.11. Initially the intensity of the H_α is low. This is the level determined

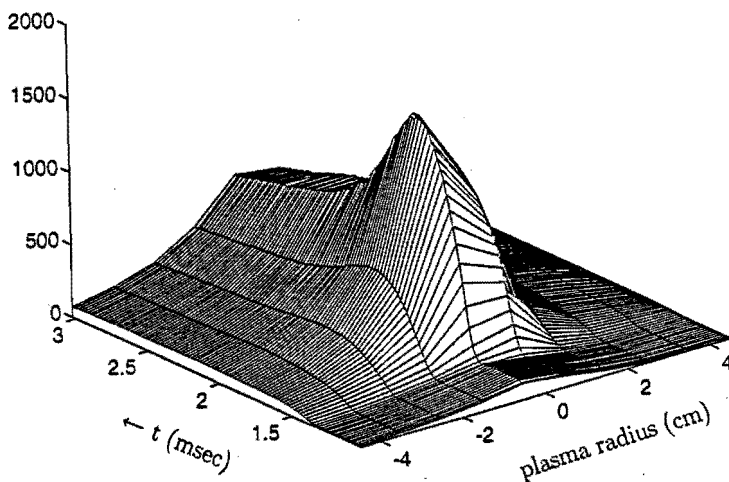


Figure 3.11. *The intensity of the H_α line in emission measured on the plasma beam.*

by the residual hydrogen background from the previous gas puff. After the next puff, initially a peak is observed with a duration determined by the pulse open time. After this peak the intensity remains high; a slow decay is observed. A similar picture arises from measurement of the Ar 696.5 nm spectral line, although for the argon line intensity a depletion rather than an

increase intensity is observed (cf. Eqs (3.12, 3.13)). The floating potential of the Langmuir probe has a slightly longer time scale.

3.5 Discussion

A comparison between the dissociation degree of the plasma emanating from the source and the plasma further downstream shows that the dissociation degree is much lower in the latter case. First the experimental methods are discussed in section 3.5.1. The recirculation concept and implications of this for the expanding cascaded arc plasma setup are discussed in section 3.5.2.

3.5.1 Experimental techniques

The dissociation degree in the source is determined from the power balance and an estimated ionization degree. The estimate of the ionization degree is based on a comparison with an argon cascaded arc plasma under similar conditions. As the major part of the energy coupled into the plasma is consumed by dissociation of the molecular hydrogen, the thus obtained dissociation degree is not very sensitive to the ionization degree used in the calculations. Furthermore, according to the dissociative recombination process described in chapter 4, each ion emanating from the source will produce 3 atoms in its loss process. Thus chemical energy stored in ions is 're-used' for dissociation with an efficiency of $\sim 50\%$. Consequently, the dissociation degree calculated with the upper limit ionization degree estimate is expected to give a good lower limit estimate of the dissociation degree.

Downstream the dissociation degree is measured with RF excited active actinometry. This is a new method that has not yet been confronted with other measurement techniques yet. The consequences of possible erroneous assumptions in the interpretation of measurements can be addressed. If the electron temperature, that is assumed to be 4 eV in reality is higher, this influences the correction factor $C_{thr}(\epsilon)$. From Fig. 6.11 it can be seen that this gives an underestimation of the dissociation degree of $\leq 25\%$ if T_e approaches infinity. If on the contrary the electron temperature in reality is lower, the atomic density is overestimated and consequently the dissociation degree is overestimated. This would only strengthen the recirculation model presented here.

The pulsed valve experiments are used to illustrate the influence of gas in the background on the plasma beam.

3.5.2 Implications of the recirculation process

Due to the recirculating background gas that is mixed into the plasma beam, the actual dissociation degree in the beam can be several times lower than

expected from the source. This is not necessarily a problem. The hydrogen atoms are rather diluted with molecular gas than lost. The issue is that the atoms must reach their target before they are lost at the walls of the reactor. Consequently, the reactor design is important. The choice of the wall material has a strong influence on the chance that hydrogen atoms associate on the walls. The geometry of the reactor determines the recirculation patterns. For example, a narrow reactor diminishes the ratio of recirculation over residence time. Concluding, the plasma beam characteristics are strongly influenced by the recirculation of background gas and the walls. In this context, the often used expression 'free expanding plasma' suggests that there is no influence from the walls and is regarded misleading.

Anomalous recombination in a hydrogen plasma jet

4.1 Introduction

Rotational and vibrational excitation of hydrogen molecules is known to be essential in negative ion formation, as the dissociative attachment reaction is endothermic. In this chapter it is argued on the basis of ion density measurements in a hydrogen plasma jet, that rovibrational excitation also can cause an anomalous fast recombination loss of protons. The mechanism involved is a charge transfer from a proton with a rovibrationally excited molecule, followed by a molecular dissociative recombination. The rovibrational excitation is needed as also the charge transfer is endothermic. The experiments discussed in this chapter concern the jet of a thermal plasma expanding into a low background pressure (0.5 mbar). The source, a cascaded arc, is a hot thermal plasma (1 eV) and produces predominantly atomic ions. The resulting plasma jet is cooled by expansion down to temperatures of 0.2 eV both for the heavy particles and for the electrons. The plasma is free expanding, i.e. the walls of the reactor are far from the plasma. There is no important negative ion formation expected under the experimental conditions. Yet a strong decrease in the ion density is observed in the hydrogen plasma jet, which can be explained only by the above mentioned charge transfer mechanism. This mechanism can be important in any plasma where hydrogen atomic ions and rovibrationally excited molecules are present. Examples are volume negative ion sources [17, 18, 19], interstellar shock waves [20], plasma deposition [2, 21] and hydrogen atom and ion sources [22]. The experimental arrangement under research (cf. chapter 2), can be divided in a source part, where the plasma is generated, and a low pressure chamber, where the plasma expands to a recombining jet. The source is a cascaded arc. For a detailed description of the cascade arc plasma we refer to other publications [3, 10]. Here it will be described in a condensed manner. It consists of three tungsten cathodes at one end, a stack of eight water cooled copper plates insulated electrically from each other by PVC spacers and vacuum sealed by

O rings, and an anode plate at the other end. Through the copper plates there is a central bore diverging from three to four mm, forming a central channel of approximately 50 mm length. The center of the anode plate is a 4 mm nozzle, connecting the cascaded arc to the vacuum chamber. The discharge is created between the cathodes and the anode plate. The pressure in the arc is subatmospheric (0.1-0.5 mbar).

The vacuum chamber is a vessel with a diameter and a length of 400 mm. A set of two rotary pumps and a roots blower keeps the pressure at 0.5 mbar in the described experiments. At the given flows the residence time of a particle in the vessel is in the order of 0.1 sec. The ion density measurements are performed using a Langmuir double probe. The Langmuir probe could be positioned at 200 to 310 mm from the exit of the cascaded arc. A radial scan from -50 to +50 mm from the plasma axis could be made. The probe characteristics were interpreted using the classical Langmuir theory, assuming a negligible sheath thickness. The probe dimensions were chosen such, that the probe diameter is much smaller than all relevant mean free path lengths and much larger than the Debye length in all experiments. The tungsten probe wires have a diameter of 400 μm , a length of 7 mm and the distance between the two wires is 2 mm.

In what follows we first will discuss the plasma source and then the plasma expansion. Three plasma compositions have been studied: pure argon, 10% hydrogen in argon and 95% hydrogen in argon, hereafter referred to as pure argon, low hydrogen and high hydrogen case respectively. The latter case is very close to a full hydrogen operated source; 5% argon was added near the cathodes to protect them from erosion.

4.1.1 The plasma source

The source is characterized by a high particle and power density. This results in a plasma that is strongly collision dominated and the excited states are in equilibrium, the so called pLTE state [23]. The ionization degree is high and the temperature is in the 1 eV range. As a consequence, the excitation from the ground state to the first excited level, which is the largest energy step, invariably leads to ionization due to ladder excitation. Furthermore, in this type of collision dominated plasma the ions will preferably be from the species with the lowest ionization energy, as charge exchange is very effective. The source is operated on 3 slm (standard liter per minute) at a power input of 3 kW in the pure argon case, and up to three times more if hydrogen is admixed. This yields a plasma with an ionization degree of 10% at the exit (anode side) of the source [10].

Now consider the situation in the plasma if hydrogen is added. Relating measurements on stationary cascaded arc plasmas to the presented situation, the same arc current gives the same axial temperatures for hydrogen and ar-

gon within 10% [24]. Vallinga [11] has shown that in a flowing cascaded arc hydrogen plasma the axial electron density is somewhat higher than in argon at the same electron temperature and gas flow. Furthermore, if the ionization degree is more than 1% the plasma conductivity is determined by Coulomb collisions, independent of the electron density and $\propto T_e^{-3/2}$ [3]. As the electron temperature is equal within 10% for the two cases, the plasma resistance is reversely proportional to the effective plasma channel cross section. In the low hydrogen case the plasma resistance is found to be almost 2 times higher than in argon, indicating a two times smaller plasma channel cross section. Combining this with the foregoing we conclude that the average electron density in the low hydrogen case will be less than a factor of 2 lower than that in argon. Experimental confirmation of this statement is available for low admixtures up to 1.4% hydrogen [26], showing no difference with the full argon case at the arc exit up to the gasdynamical shock. As mentioned above, the ionized particles in the source plasma will preferably be from the species with the lowest ionization energy, in casu hydrogen. If the percentage of atomic hydrogen admixed is below the ionization degree in pure argon, the plasma ionizes the added hydrogen by means of the charge transfer between argon ions and hydrogen atoms. This process is very effective until the full amount of argon ions is consumed; at above roughly 5% molecular hydrogen gas flow in argon the ions will mainly be H^+ . Experimental support for this is found in emission spectroscopy in the expansion close to the exit of the same plasma source [22]. In a situation where 10% hydrogen was added in the plasma source, the only spectral lines measured in the expansion section were the atomic hydrogen Balmer series. Since the temperature in the expansion is decreasing fast to values of about 0.3 eV [6], the light emission in the argon case can only originate from dielectronic recombination. The absence of argon lines, therefore, implies the absence of a significant argon ion density.

4.1.2 The plasma jet

The outflowing plasma jet in pure argon was studied thoroughly by Van de Sanden [6] by means of accurate Thomson-Rayleigh scattering measurements. The main characteristics are listed here. Directly after the source the plasma expands supersonically and cools down to 0.3 eV. The plasma composition is frozen in as a result of the high velocity and low density. After a few centimeters, when the stagnation pressure in the plasma jet becomes equal to the background pressure, a shock occurs. After the shock the flow is subsonic and only slightly decelerates over the studied region (200 to 310 mm downstream the source). The plasma jet in pure argon does not recombine significantly, in accordance to theoretical expectations: radiative and three particle recombination are too slow. The absence of recombination is con-

firmed by Langmuir double probe measurements, that show good agreement with Thomson-Rayleigh scattering results [8]. Figure 4.1 shows three radial

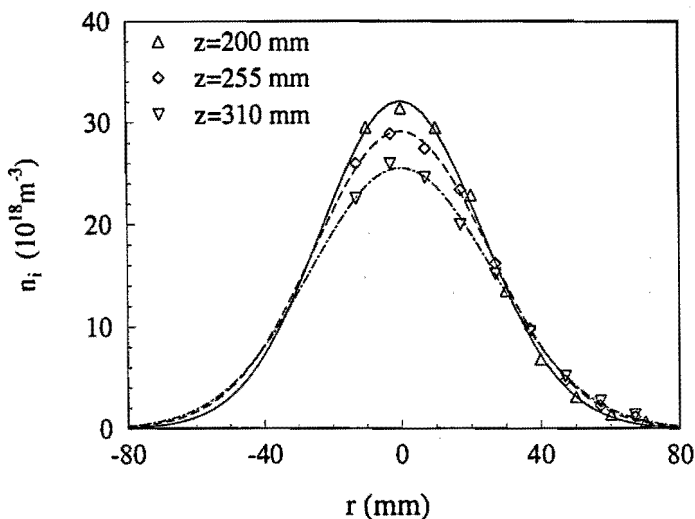


Figure 4.1. Radial ion densities in the plasma jet for pure argon at 200, 255 and 310 mm downstream the plasma source. The arc current is 45 A, the reactor pressure is 0.5 mbar.

ion density profiles at 200, 255 and 310 mm from the source, which can be described by Gaussian profiles. The surface under these Gaussian profiles remains approximately constant for the three different axial profiles. This indicates that the ion line density N_i , i.e. the ion density integrated over the cross section of the jet, is constant. As the flow velocity w_{plasma} is approximately constant, this implies that the ion flux is approximately constant for the three axial positions, confirming that no significant recombination occurs for argon.

If hydrogen is added to the plasma the situation changes drastically in the plasma jet. The plasma temperature is lower, 0.2 eV in the low hydrogen case and somewhat more than 0.1 eV in the high hydrogen case. Fig. 4.2 gives the radial density profiles as measured with a Langmuir double probe at 200, 255 and 310 mm downstream the source for the three studied plasma compositions. Apparently the presence of hydrogen can lead to a decrease of the ion density of three to four orders of magnitude. The low hydrogen case plasma has almost the same acoustic properties and can therefore directly be related to the argon plasma. The acoustic properties of the high hydrogen case plasma will be closer to the full hydrogen case. In this case the velocities can be up to a factor of $\sqrt{(m_H/m_{Ar})}$ larger, where m_H and m_{Ar} are the

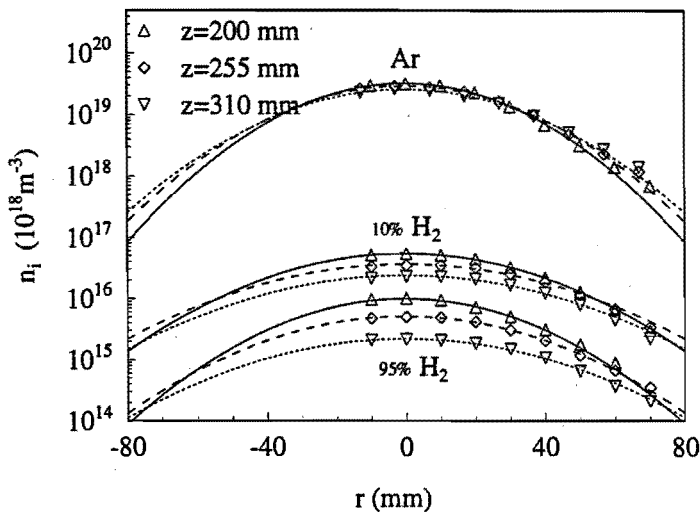
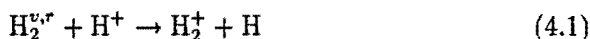


Figure 4.2. Radial ion density profiles for Ar and Ar/H₂ mixtures. The arc current is 45 A and reactor pressure is 0.5 mbar in all cases. The y-scale is now logarithmic.

mass of the hydrogen and argon atom. In the following we will concentrate on the low hydrogen case in comparison with the pure argon case. The radial density profiles measured in the hydrogen mixtures are not significantly broader than in a pure argon plasma (cf. Fig. 4.2), confirming similar transport behaviour. As the ion density at the source and the flow behaviour are similar for the first two cases, the addition of hydrogen must cause a new and strong recombination channel in the bulk plasma. To establish the cause of this decrease several items have to be addressed. As mainly atomic hydrogen ions leave the source, the responsible mechanism must start with these ions. It can easily be shown that two and three particle recombination are not effective at the given time scale and plasma densities, as is also evident from the pure argon case. The same thing accounts for the formation of negative ions in combination with mutual annihilation. Here we present a mechanism based on charge exchange and dissociative recombination that explains for the observed electron density decay. First step in this reaction mechanism is the charge transfer between a proton and a rovibrationally excited molecule



The molecular ion formed by the charge transfer reaction can directly recombine dissociatively,



or by formation of H_3^+



again followed by dissociative recombination:



or



Reaction 4.2 is very fast. Under the plasma conditions as presented in this chapter, due to the low ionization degree reactions 4.3 to 4.5 will be dominant, as was confirmed by the presence of a significant amount of H_3^+ in mass spectroscopy measurements and the total absence of H_2^+ [22]. The rate coefficient for reaction 4.5 has been subject to discussion in several publications over the years [27, 28, 29, 30, 31]. It is likely to be very large. Therefore, in the molecular recombination channel the charge transfer reaction is an essential step. For ground state molecules this is an endothermic reaction. Niedner et al. [32] have shown that this charge transfer is a two step mechanism: a vibrational excitation to $v \geq 4$ followed by a resonant, exothermic charge transfer. In a plasma, a fraction of the molecules will already be in the vibrational states $v \geq 4$. Cross sections for the second step, the exothermic charge transfer, are not available. However, in an exothermic charge transfer reaction the Langevin limit [33] usually is a good estimate for the charge transfer cross section σ_{CT} . The corresponding charge transfer rate k_{CT} has a value of approximately $2.5 \cdot 10^{-15} \text{ m}^3\text{s}^{-1}$. Now the time dependent behaviour of the atomic ion density is given by

$$dn_{H^+}(t)/dt = -k_{CT}n_{H^+}n_{H_2^{v,r}} \quad (4.6)$$

which has the solution

$$n_{H^+}(t) = n_{H^+}(0)\exp(-n_{H_2^{v,r}}k_{CT}t) \quad (4.7)$$

The evolution of $n_{H^+}(t)$ in time due to the charge exchange channel now depends on $n_{H_2^{v,r}}$ and k_{CT} . At the position of the measurements the ion density has decreased by almost three orders of magnitude, so $n_{H_2^{v,r}}k_{CT} \approx \ln(1000)$. At a typical temperature of 2000 K and a time of flight of 0.4 msec, a population density for $H_2^{v,r}$ of $\approx 10^{19} \text{ m}^{-3}$ is required. It has been measured that in the vessel and in the plasma jet the abundance of H_2 is much larger than that of H atoms, even though the source delivers mainly atoms and atomic ions. The reason for the dominance of molecular hydrogen is the wall association of atoms to molecules and the finite residence time of ~ 0.1 second. The molecular hydrogen density is approximately $2.5 \cdot 10^{21} \text{ m}^{-3}$ at a pressure of 0.5 mbar and temperature of 2000 K. A vibrational temperature of approximately 3000 K yields a sufficient thermal population of the higher vibrational

levels. The vibrational temperature can be 'frozen' in the expanding plasma jet [34]. Upstream the temperature is higher, so there may be an overpopulation of higher vibrational levels. Another source of vibrational excited molecules can be the Eley-Rideal associative desorption of hydrogen atoms at the walls. It is suggested [14] that up to 40% of the thus formed molecules reenters the plasma in a vibrational excited state $v \geq 4$. As the reentering molecules form the main part of the residual H_2 abundance, this again makes a significant vibrational population plausible. So far we followed the two-step reaction, *vibrational* excitation followed by charge transfer. However, as the gas temperature is close to the electron temperature in the presented experiments, the internal energy of the molecules in reaction (1) may well originate from rotational excitation. The increasing statistical weights of the higher rotational levels ($2K+1$) will enhance their importance. In this sense the experimental situation here presented is different from the usual low pressure gas discharges where the rotational excitation is negligible. Resuming, the main points of the above are:

1. charge exchange followed by dissociative recombination is the dominant ion loss processes; 2. both are fast; 3. vibrational and/or rotational excitation are essential to have a fast charge exchange.

A last point will be addressed here. The charge transfer is assumed to be the rate limiting step in the above described recombination process. This is certainly true in the first part of the plasma jet, as the electron density is high and $n_e k_{DR} > n_{H_2^{v,r}} k_{CT}$, where k_{DR} is the dissociative recombination rate coefficient, k_{CT} the charge transfer rate coefficient and $n_{H_2^{v,r}}$ the density of rotationally and vibrationally sufficiently excited molecules. However, under the assumption that the density of excited molecules is not decreasing very fast, the observed efficient molecular recombination process decreases the ion and electron density decrease fast to such low values that the dissociative recombination becomes the rate limiting process. This actually is the case between $z=200$ and $z=310$ mm, where the electron density is a few times 10^{16} m^{-3} in the low hydrogen case and even lower in the high hydrogen case, see Fig. 4.2. The ratio $H^+ : H_3^+$ can be estimated by balancing the production and destruction of the molecular ion. The production is governed by reaction 4.1 and the destruction by 4.4, 4.5. Balancing destruction and production we obtain:

$$n_e n_{H_3^+} k_{DR} = n_H^+ n_{H_2^{v,r}} \quad (4.8)$$

For $n_e = 5 \cdot 10^{16}$, the maximum value in the low hydrogen case, this yields a ratio $H^+ : H_3^+$ of 1:10. As a consequence, the dominant ion at these positions will be H_3^+ rather than H^+ . Therefore, for the Langmuir probe measurements the H_3^+ ion mass is used in both the low and high hydrogen case. This implies that almost all atomic ions emanating from the source already have been transferred to molecular ions, confirming that reaction 4.1 is very fast. In Fig. 4.3 the radial profiles from Fig. 4.2 are integrated to line

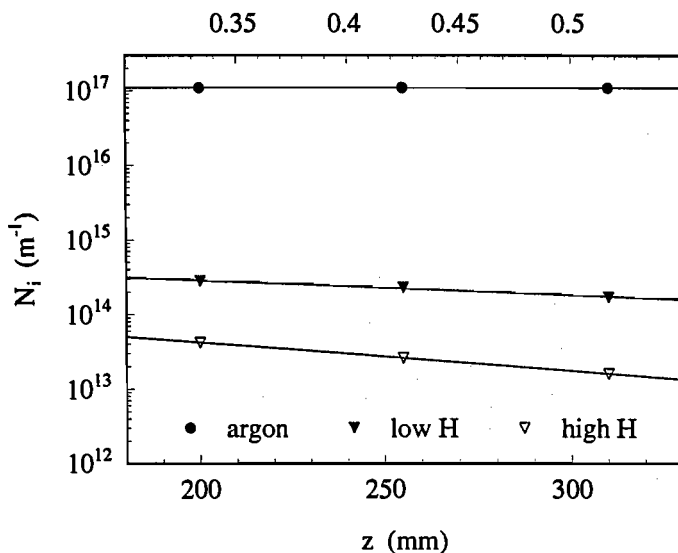


Figure 4.3. Axial line ion densities for the three plasma compositions.

ion densities N_i , i.e. the ion densities are integrated over the cross section of the plasma jet. At the top of this Fig. a time scale is added. The time scale along the plasma axis is given by $t = z/w_{plasma}$, where w_{plasma} is the plasma flow velocity. After the shock the plasma is only slightly decelerating. The magnitude of the velocity depends on the pressure in the expansion chamber, and has a value between 500 and 1000 ms^{-1} [3]. Under the given conditions it is estimated to be 600 ms^{-1} . The addition of a time axis allows us to estimate the rate for dissociative recombination for H_3^+ ions. Using the molecular ion mass for the probe measurements and the decrease in ion density observed from Fig. 4.3 k_{DR} is estimated at a value of $6 \cdot 10^{-14} m^3 s^{-1}$ at a plasma temperature of 2000 K. The accuracy of this value is estimated to be 50%. If we assume that the T_e^{-1} dependence of the dissociative recombination cross section on the electron temperature as found in literature [30] is still valid around 2000 K, the agreement is good: we find $2 \cdot 10^{-13} m^3 s^{-1}$, extrapolated to 300 K, whereas in literature values from $1.7-2.3 \cdot 10^{-14} m^3 s^{-1}$ are reported [28, 29, 30, 31].

4.2 Conclusions

The presented experiments show, that expansion leads to an electron density of down to $10^{19} m^{-3}$ in a pure argon plasma jet, with a marginal influence of recombinative atomic processes. In a hydrogen containing plasma jet three

to four orders of magnitude lower ion densities are found. The anomalous fast recombination in hydrogen can not be explained with two- or three particle recombination in the pure hydrogen and argon/hydrogen mixtures. It is shown that the observed ionization loss can be described by the molecular dissociative recombination process. However, the cascaded arc source is known to contain only atomic ions. In this chapter a molecular channel is proposed that is based on the conversion of atomic to molecular ions by charge transfer. This charge transfer reaction is endothermic if the molecules don't have an important internal energy, vibrational and/or rotational. However, if the internal energy of the ion is sufficient the reaction becomes exothermic and can become very fast. It is shown that with the charge transfer cross section according to the Langevin limit and with reasonable assumptions on the rovibrational population, the charge transfer reaction is fast enough to explain the observed time scale behaviour of the recombination process in the plasma jet, whereas no reasonable alternative explanations seem to be available. This implies, that in any hydrogen dominated plasma that contains a sufficient rovibrational population and atomic ions charge exchange can be an important source of molecular hydrogen ions.

5

The atomic hydrogen Balmer spectrum

5.1 Introduction

In the recombining plasma beam the emitted spectrum originates from recombination processes. The in gas discharges prevalent excitation of particles from the ground state is not possible (first excited level at ~ 10 eV). This is a natural consequence of the low electron temperature of the plasma (~ 0.3 eV). For the argon expanding cascaded arc plasma beam, it has been shown that the dominant process that populates excited states that are observed in emission is three particle recombination $\text{Ar}^+ + e + e \rightarrow \text{Ar}^* + e$ [35]. In the hydrogen plasma beam, besides the atomic three particle recombination $\text{H}^+ + e + e \rightarrow \text{H}^* + e$ also recombination with molecular ions is possible [36]. An example of a recorded emission spectrum from a hydrogen plasma beam is given in Fig. 5.1. Only the atomic Balmer spectrum is observed. Apparently the atomic recombination processes only populate *atomic* excited levels.

From the atomic spectrum an AtomState Distribution Function (ASDF) can be determined. It appears that in a recombining plasma this ASDF shows an inversion. Whereas in e.g. a helium plasma this effect is marginal, in a hydrogen plasma the inversion can be very strong [37]. Several studies have been dedicated to this phenomenon in recombining hydrogen plasma beams. Up to now all efforts to explain the observed inversion theoretically have been restricted to atomic models (only H^+ ions) [38, 39, 40, 41]. As it appears that these atomic models are inadequate to explain the experimental results, additional sources must be present that populate excited atomic states. In this work also molecular recombination processes are considered. Based on the abundance of rovibrationally excited molecules that is argued in chapter 4, possible sources are suggested for excited states.

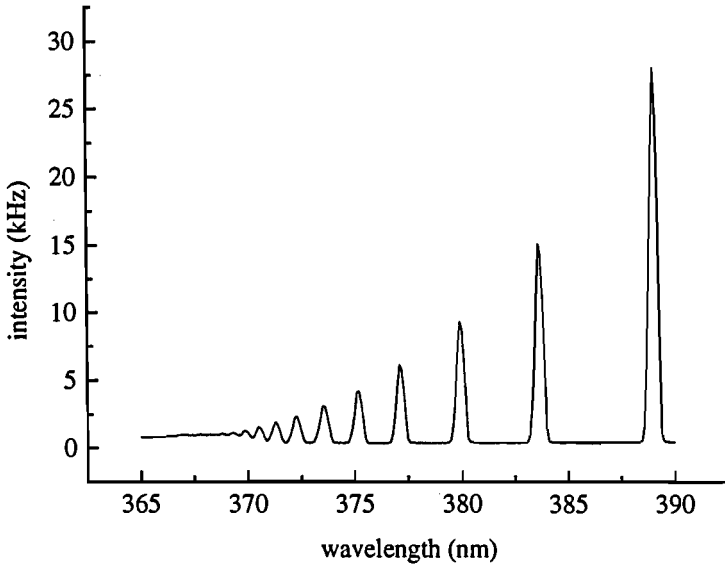


Figure 5.1. A part of the measured spectrum from a hydrogen plasma beam. Only the atomic Balmer lines are observed. Default plasma settings are used, with a hydrogen seeding fraction of 20%.

5.2 Experimental setup

The plasma machine is discussed in detail in chapter 2. At a central position in the reactor, a Langmuir double probe was placed. This probe was put perpendicular to the magnetic field in order to minimize shadowing effects in the case of magnetic field. The probe length was ~ 6 mm, the probe radius

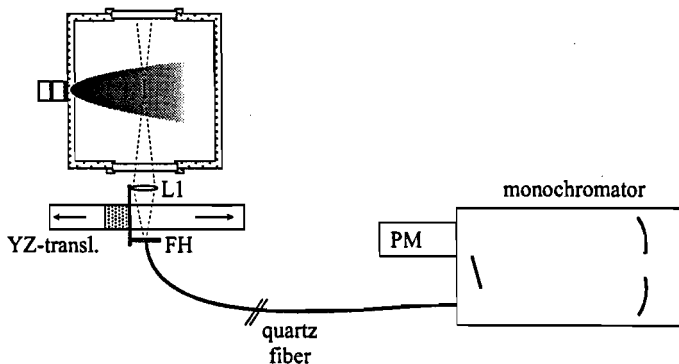


Figure 5.2. The optical setup

200 μm .

An optical system was used to scan the plasma emission in the region 200-300 mm downstream the source. A schematic representation of the optical system is given in Fig. 5.2. Lense L focuses the plasma light on the circular aperture of a quartz fiber bundle. The fiber bundle is mounted on a y,z positioning system. This system allows axial and radial scans of the plasma beam. The other end of the fiber is mounted on the entrance slit of a Jarrel Ash 0.5 m monochromator. This end of the fiber bundle is rectangular (0.5 \times 20 mm) in order to improve the transmission of the optical system. The light is detected by a ENI 9698 QB photo-multiplier tube. The pulses that are generated in the photo-multiplier tube when a photon is detected, are converted to TTL pulses. A PC, that also controls the monochromator wavelength setting and the positioning system, further processes the measured signal. The optical system is calibrated absolutely with the use of a tungsten ribbon lamp.

5.3 Atomic state distribution function

In an optical thin plasma in a stationary situation the density of a state p is balanced by production P_p

$$P_p = \overset{\text{3 PARTICLE RECOMB.}}{n_e^2 n_i k_{3r}(p)} + \overset{\text{2 PARTICLE RECOMB.}}{n_e n_i k_{2r}(p)} + \overset{\text{COLLISIONAL (DE)EXC.}}{\sum_{q \neq p} n_e n_q k_{qp}} + \overset{\text{CASCADE RAD.}}{\sum_q A_{qp} n_q} + \overset{\text{OTHER SOURCES}}{S_{mol,p}} \quad (5.1)$$

Here $k_{3r}(p)$ is the three particle recombination rate coefficient, $k_{2r}(p)$ is the two-particle recombination rate coefficient, k_{pq} is the collisional deexcitation rate coefficient from level q to p . Cascade radiation from a level q to a level p is proportional to A_{qp} , the transition probability belonging to the radiative transition $q \rightarrow p$. The source term S_{mol} is reserved for molecular sources for n_p . The destruction D_p of a state p is given by

$$n_p D_p = \overset{\text{COLLISIONAL (DE)EXC.}}{n_p \sum_{q \neq p} n_e k_{pq}} + \overset{\text{IONIZATION}}{n_e n_p k_{pi}} + \overset{\text{RAD. DECAY}}{n_p \sum_{q < p} A_{pq}} \quad (5.2)$$

Here k_{pi} is the ionization rate coefficient from a level p , k_{pq} is the rate coefficient for collisional deexcitation from the level p , and A_{pq} the transition probability for radiative decay. The destruction of levels can either happen collisionally or radiatively. At low p values radiative decay will be the main loss process, at high p values collisional deexcitation is dominant ¹. For an

¹The radiative decay is proportional to $\sum_{q < p} A_{pq}$. This sum scales with p^{-5} [42]. In collisional deexcitation the stepwise process $k_{p,p-1}$ is dominant. Based on classical consid-

atomic plasma Van der Mullen derived for the critical level p_{cr} , where collisional and radiative decay are equal $n_e p_{cr}^9 = 4.20 \cdot 10^{23} \tilde{T}^{-0.5} \text{m}^{-3}$, with \tilde{T} the electron temperature in eV. At this value of p the derivative of production over destruction, $\frac{d}{dp} \left(\frac{P_p}{D_p} \right) = 0$.

For high excited states the collisional processes become increasingly effective, and eventually ionization and recombination processes establish an equilibrium situation between the highest excited states and the ions and free electrons. If a level n_p is in equilibrium with the ion density, its density is described by the *Saha-Boltzmann* equilibrium equation with $T = T_e$ [43, 44],

$$\frac{n_p^S}{g_p} = \left(\frac{h^2}{2\pi m_e k T_e} \right)^{3/2} \frac{n_e^2}{g_e g_i} e^{E_{pi}/kT_e} \quad (5.3)$$

Here n_p^S is the density of state p in Saha-equilibrium, g_p the statistical weight of state p , and E_{pi} the ionization energy from level p . In a purely atomic recombining plasma Eq. (5.3) is valid for $p > p_{cr}$. In the molecular plasma additional excitation sources are present and the situation can be different.

A commonly used representation of ASDFs is the Boltzmann plot. In a Boltzmann plot $\ln(n_p/g_p)$ is plotted versus E_{pi} . Note that $E_{pi} = Ry/p^2$, and a decreasing energy scale corresponds to an increasing principal quantum number p . An example is given in Fig. 5.3(a). This representation is convenient in the case of an atomic plasma, as the high p part of the ASDF is in Saha-Boltzmann equilibrium: the slope of the distribution yields the electron temperature (cf. Eq. (5.3)). At the position of p_{cr} a local maximum appears in the Boltzmann plot, an inversion. Below this position, the radiative decay is dominant over collisional processes and the n_p/g_p value will be below the Saha-Boltzmann density.

A useful parameter is the over- or underpopulation factor b_p ,

$$b_p = \frac{n_p}{n_p^S} \quad (5.4)$$

that gives the population relative to the Saha-Boltzmann equilibrium density. In a b_p -plot b_p is plotted versus E_{pi} . An example of a b_p -plot is given in Fig. 5.3(b). For the high levels, that are in Saha-Boltzmann equilibrium, $b_p=1$. At the inversion point p_{cr} the radiative decay starts to contribute significantly to the depopulation and consequently $b_p < 1$. In an atomic recombining plasma values of b_p above 1 are not possible [26]. An advantage of this representation is that it helps to identify sources in the excitation space. A clear situation is found if $b_p > 1$; this situation can only occur if molecular sources ($S_{mol,p}$ in Eq. 5.1) are available.

erations (atom radius $\propto p^2$) the collisional cross section scales with p^4 [42]. Consequently, for lower excited levels radiative decay is dominant, for high excited levels collisions dominate the decay. The ratio of collisional to radiative decay scales with $p^4/p^{-5} = p^9$.

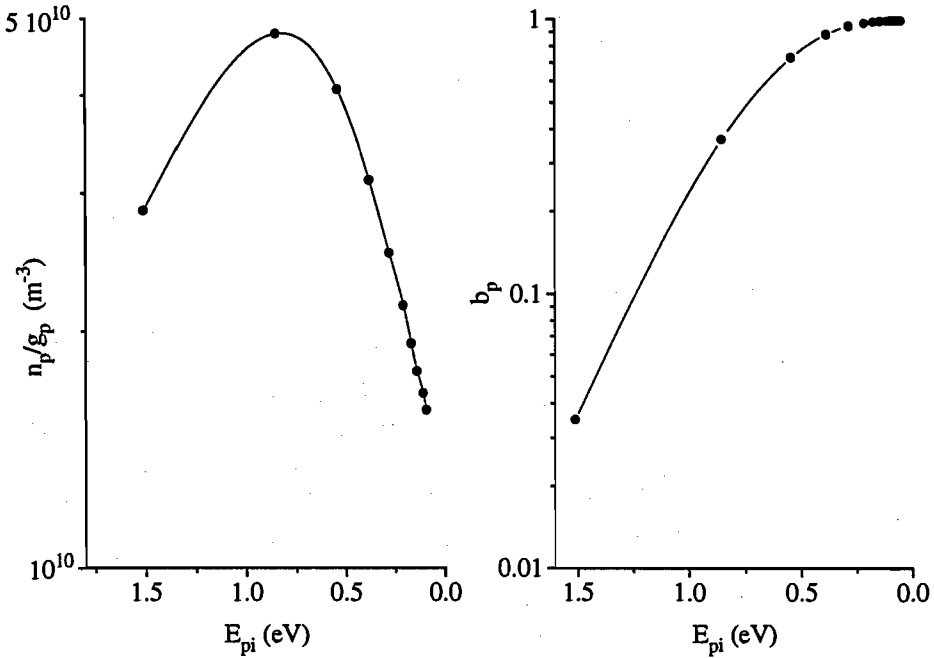


Figure 5.3. (a) Boltzmann plot of the ASDF of an atomic recombining system. (b) b_p plot of the same ASDF.

5.4 Experiments

Atomic spectra have been recorded for axial positions $z=18, 21, 24, 27$ and 30 cm. On each axial position a radial scan was made. This has been done to enable Abel inversion of the measured intensity profiles. This way local values of the intensity can be calculated from the measured line integrated intensities. The image of the optical fiber on the plasma is ~ 5 mm. The plasma radius is typically 5 cm. The radial step size was taken 5 mm.

The radial profiles were fitted with a sum of Gaussians at the same lateral position. As the Abel inversion of a Gaussian is a Gaussian [45], the inversion can be performed analytically. The locally determined intensities immediately yield the absolute state density (with the optical system calibrated absolutely).

In order to increase the electron density and thus to obtain a large intensity also for the higher Balmer lines, a magnetic field has been applied in the expansion chamber. Unless mentioned otherwise, the coil current is 250 A, producing a field strength of ≈ 0.04 T near the source decreasing to ≈ 0.0125 T at $z=300$ mm (cf. chapter 2, Fig. 2.2). The magnetic field

increases the electron temperature and density. The arc was operated on a high current, 70 A, for the same reason. The total gas flow was kept at 3.5 slm in all measurements. The pressure in the reactor was 0.4 mbar.

For each condition the electron temperature and density has been measured at an axial position $z=24$ using a double Langmuir probe, that was placed perpendicular to the magnetic field. The orientation of the Langmuir probe relative to the magnetic field is important. It appeared that if the probe was placed parallel to the magnetic field lines, the measured electron density could be up to a factor of ten lower compared to the perpendicular orientation. The measured electron temperature was up to 50% higher in the parallel orientation. The use of a Langmuir probe in a magnetized plasma must be done with great care. Several complications can occur in the interpretation of measurements. To address this matter, ratios of the Larmor radius r_L^e of the electrons, the probe radius r_p and the sheath thickness r_s must be considered. Typical plasma conditions are $T_e=0.3$ eV, $n_e = 3 \cdot 10^{18} \text{ m}^{-3}$. The magnetic field strength at the center of the reactor is 0.02 T at a coil current of 250 A. At these values $r_L^e \approx 100 \mu\text{m}$, $r_p \approx 200 \mu\text{m}$ and $r_s \approx 2 \mu\text{m}$. If $r_L^e < r_s$, the sheath is disturbed and magnetosheath effects should be considered. This is not the case here. If $r_L^e < r_p$, geometrical effects are involved which result in magnetic field shadowing of the probe. This is the case here. It has been shown [46] that this effect is minimal if the probe is oriented at 90° perpendicular to the magnetic field. Figure 5.4 shows a Boltzmann plot of a 90% hydrogen, 10% argon plasma. An inversion on $p=6$ is observed. The electron density and temperature were $T_e=0.31$ eV, $n_e=2.8 \cdot 10^{18} \text{ m}^{-3}$. A b_p plot shows that all levels are overpopulated compared to atomic three particle recombination. The large b_p values show that a source must be present in the ASDF at high p values ($p=4-7$). The excited levels will not be in Saha equilibrium and therefore it is not allowed to determine the electron temperature from the Boltzmann plot. As a matter of fact, if this is done anyway from Fig. 5.4 a temperature of ~ 0.1 eV is obtained.

A similar picture is obtained from a 20% hydrogen plasma, cf. Fig.5.5. The electron temperature now is 0.31 eV, the electron density $3 \cdot 10^{18} \text{ m}^{-3}$. The electron temperature derived from the Boltzmann plot would now be 0.32 eV. The observed densities are still an order-of-magnitude too high compared to the atomic model.

If the magnetic field is switched off, n_e decreases to $2.4 \cdot 10^{17} \text{ m}^{-3}$, and T_e to 0.21 eV. The n_p/g_p are much smaller, cf. Fig. 5.6. It is noted that different from Figs. 5.4 and 5.5 the n_3 density is relatively high compared to the higher excited states. This distribution, with a local minimum at $p = 4$, can not be obtained from an atomic collisional radiative model for hydrogen. Therefore a source must be present that strongly populates $n = 3$.

Figure 5.7 shows n_p/g_p and b_p for a 3% hydrogen plasma at a coil current of 125 A. The Langmuir probe gave an electron density of $2 \cdot 10^{18} \text{ m}^{-3}$,

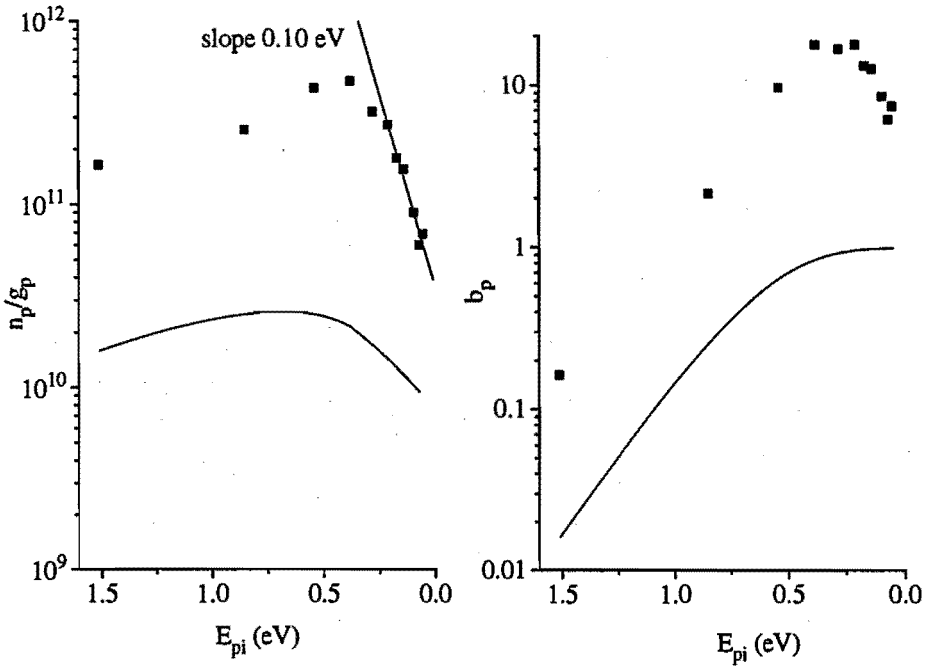


Figure 5.4. (left) Boltzmann plot of the ASDF measured on a 90% hydrogen plasma. The drawn curve is calculated with $T_e=0.31$ eV, $n_e=2.8 \cdot 10^{18} \text{ m}^{-3}$ and a purely atomic model. (right) b_p plot of the same ASDF.

$T_e=0.34$ eV. Although the state densities are much higher than in Fig. 5.6, a similar behaviour is observed. Also here a source must be present, that strongly populates $p = 3$. If a temperature is derived from the Boltzmann plot, a low value of <0.08 eV is obtained. Also at high p values the atomic model can not explain the observed state distribution. Sources near $p=6-9$ are suggested by the b_p -plot.

If the magnetic field is increased to its default value of 250 A, the Boltzmann plot of the 3% hydrogen plasma changes drastically. The Langmuir probe gave an electron density of $4 \cdot 10^{18} \text{ m}^{-3}$, $T_e=0.35$ eV. An electron temperature taken from the slope of the Boltzmann plot would yields a value $T_e = 0.29$ eV. The n_p/g_p of $p = 3$ and 4 are high; in the b_p plot the overpopulation of these levels is even larger than that of higher lying levels. In an atomic recombining model, these levels have $b_p \ll 1$. as they are strongly depopulated radiatively. This implies that a source at $p=2-4$ must be present.

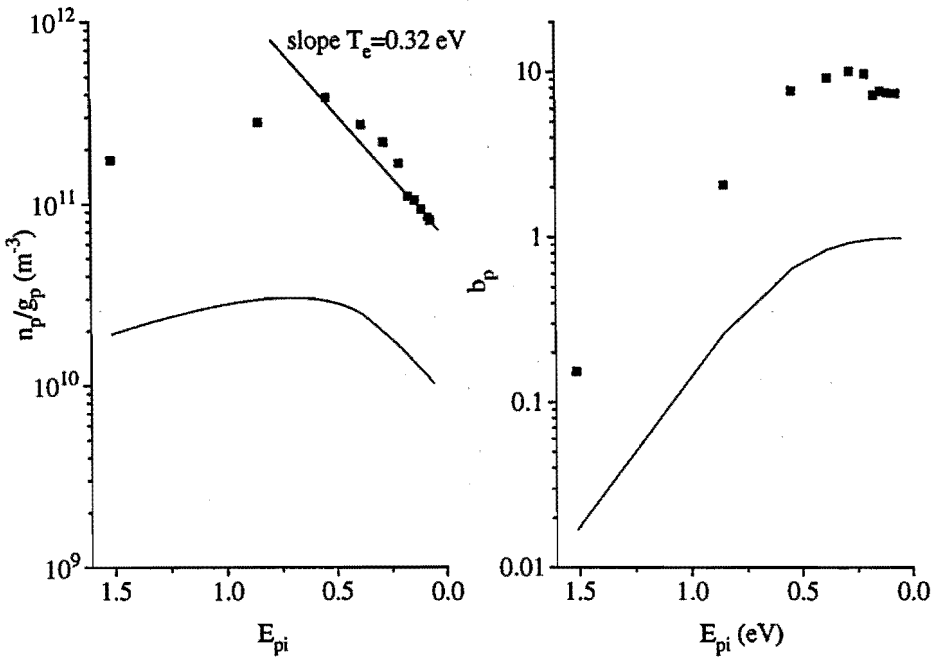


Figure 5.5. (left) Boltzmann plot of the ASDF measured on a 20% hydrogen plasma. The drawn curve is calculated with $T_e=0.31$ eV, $n_e=3 \cdot 10^{18}$ m^{-3} and a purely atomic model. (right) b_p plot of the same ASDF.

5.5 Discussion

In all figures the calculated ASDF from the atomic model gives lower populations than the experimental values. The shape of the Boltzmann and b_p plots reveals sources on $p \leq 3$ and at higher p -values (5-8). This observation is not unique in this work. Van de Sanden [47] showed for several publications, addressing the inversion in recombining hydrogen plasmas, $b_p \gg 1$ for some excited levels if independent n_e , T_e measurements were available. Atomic models are not adequate to explain this kind of results. Strong sources must be present in the ASDF. Molecular processes are considered here. In ref. [36] it is argued that in the hydrogen plasma beam a considerable fraction of the hydrogen molecules can be in a rovibrationally high excited state, leading to a high density of H_2^+ ions. The high internal (rovibrational) energy can also lead to high H^- densities [47]. Assuming that these ion densities are sufficiently high ($\sim 10^{17} - 10^{18}$ m^{-3} , cf. ref. [47]), speculations can be made on possible molecular sources for the ASDF. The first reaction considered is

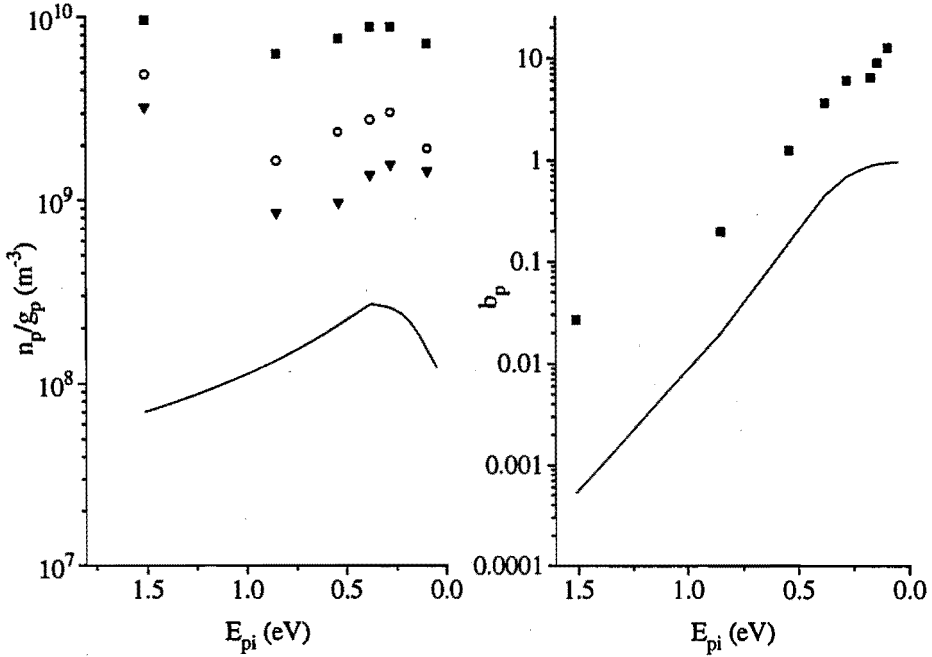
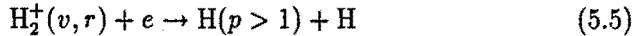
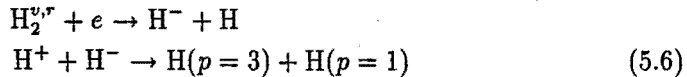


Figure 5.6. (left) Boltzmann plot of the ASDF measured on a 20% hydrogen plasma with no magnetic field applied. The drawn curve is calculated with $T_e=0.21$ eV, $n_e=2.4 \cdot 10^{17} \text{ m}^{-3}$ and a purely atomic model. (right) b_p plot of the same ASDF.

the dissociative recombination



If the molecular ion has no vibrational (or rotational) energy, only $p=2$ is energetically accessible. If however the ion has internal energy, higher excited states might be accessible. A second molecular channel is mutual annihilation,



The mutual annihilation can only populate $p=3$; higher levels are not accessible. The sources on $p=3$ that are observed in Figs 5.6, 5.7, 5.8 can be explained with this reaction. Take for example the 3% hydrogen, 250 A coil current measurement. The state density $n_3 \approx 2 \cdot 10^{14}$. If $n_H^+ \approx n_e = 4 \cdot 10^{18}$, balancing production and radiative decay of n_3 , $k_{ma} n_H n_H^+ = n_3 (A_{31} + A_{32})$ yields $n_{H^-} \approx 10^{17} \text{ m}^{-3}$.

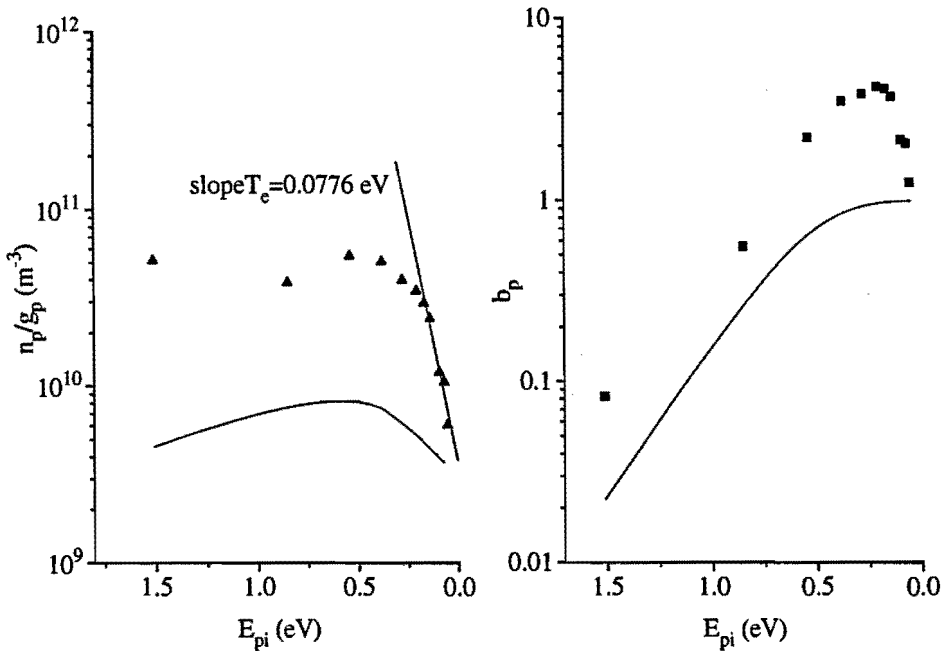
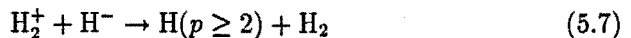


Figure 5.7. (left) Boltzmann plot of the ASDF measured on a 3% hydrogen plasma with a coil current of 125 A. The drawn curve is calculated with $T_e=0.34$ eV, $n_e=2 \cdot 10^{18} \text{ m}^{-3}$ and a purely atomic model. (right) b_p plot of the same ASDF.

The atomic mutual annihilation can not explain the observed sources at higher p values. In molecular annihilation more energy is available, as the ionization energy of the molecule is 1.8 eV higher,



Data on the final state of the excited atom are not available. An estimate can be obtained if the cross sections are calculated with the Landau-Zener approximation [48]. These calculations show, that a wide range of excited atomic states is accessible, and the cross section is largest near $p=4-7$. The molecular mutual annihilation reaction may therefore explain the sources at high excited levels.

The three molecular reactions suggested above depend on the densities of the involved ions. These densities are determined by the dominant production and destruction processes. Production of H_2^+ and H^- depends strongly on the abundance of rovibrationally excited molecules. Measuring of the rovibrational populations by e.g. CARS, and measuring of the various ion fractions H^+ , H_2^+ , and H^- is desired before further speculation to take place.

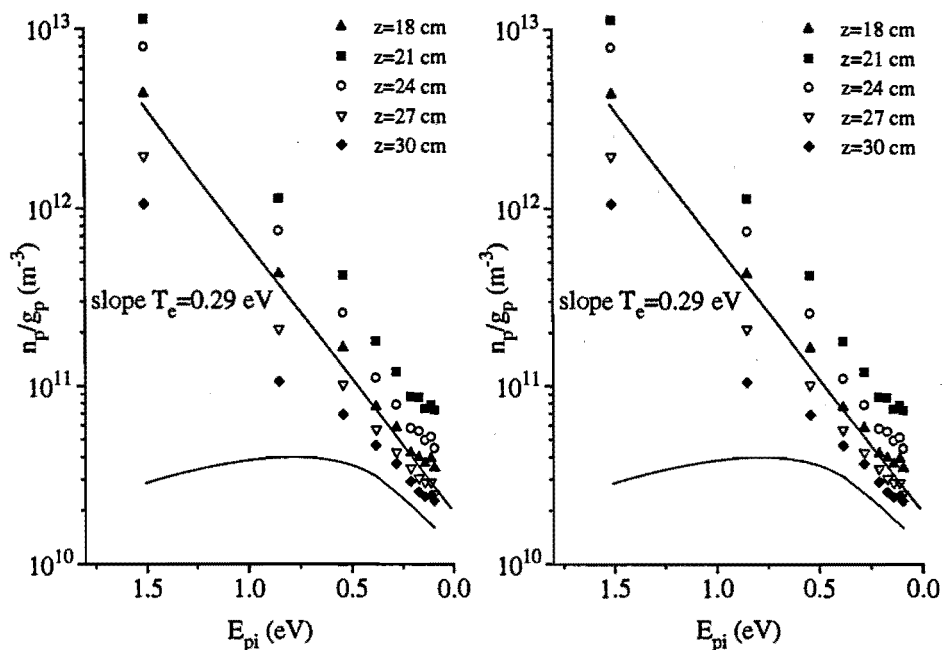


Figure 5.8. (left) Boltzmann plot of the ASDF measured on a 3% hydrogen plasma with a coil current of 250 A. The drawn curve is calculated with $T_e = 0.95 \text{ eV}$, $n_e = 4 \cdot 10^{18} \text{ m}^{-3}$ and a purely atomic model. (right) b_p plot of the same ASDF.

Particularly interesting is also the influence of recirculation of wall produced excited molecules. The strong deviations in the ASDF from an atomic model make clear that molecular processes have to be included in a proper description of the excitation of the Balmer spectrum in a recombining hydrogen plasma beam.

6

Molecular excitation and the Fulcher α spectrum

6.1 Introduction

The relevance of molecular spectroscopy on hydrogen plasmas is based upon the information that can be obtained about rotational and vibrational structure of the spectrum and the related positioning of the energy over the degrees of freedom of the system. This work focuses on the so-called Fulcher α spectrum. The reason for this choice is that, unlike other bands in the visible, the Fulcher α bands have well known radiative properties. Furthermore most molecular levels are not disturbed by interaction with other electronic states. Especially the Q -lines (no change in rotational quantum number in the radiative decay) are very well-behaved. The Fulcher α spectrum originates from transitions of the electronic $d^3\Pi$ state to the $a^3\Sigma$ state.

The population and depopulation of the upper, radiative $d^3\Pi_u$ level can be described by a balance equation. The discussion is limited to plasma conditions under which the levels relevant to the Fulcher band are in the *Corona phase* [23]: all population of the excited state occurs through electron impact excitation on the ground state, all decay is radiative. Under this assumption no complicated collisional-radiative model including vibrational and rotational excitation is needed. Figure 6.1 depicts the potential energy diagram of the levels involved in this balance equation. Indicated are the ground level, $X^1\Sigma_g^+$, the upper level $d^3\Pi_u$ and the lower level of the decay $a^3\Sigma_g^+$. The objective of this chapter is to relate the observed spectrum to the rovibrational population of the electronic ground state. The molecular structure and all aspects of collisional excitation and radiative decay are addressed in sections 6.2 to 6.5. Practical implications for the interpretation of the Fulcher α spectrum are found in section 6.6. This section concerns the ground state vibrational and rotational temperature and an actinometric method that can be used to determine the dissociation degree of a hydrogen plasma.

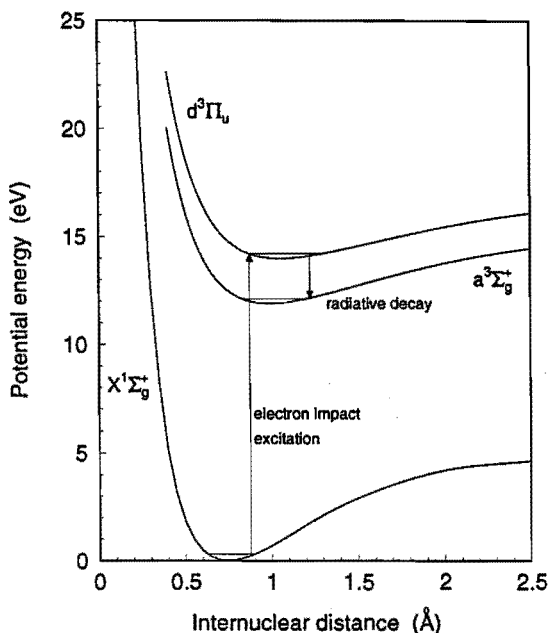


Figure 6.1. Potential energy diagram for the H_2 levels involved in the Fulcher spectrum. Population of the $d^3\Pi$ state usually originates from excitation from the ground state by electron impact, radiative decay can only go to the $a^3\Sigma_g^+$ state.

6.2 Molecular structure

The understanding of a molecular spectrum involves insight in the electronic, vibrational and rotational energy levels of the molecules and the possible transitions between these. The following treatment is aimed on the interpretation of the Fulcher α spectrum, starting from the Schrödinger wave equation.

The wave equation for the hydrogen molecule reads

$$\left(-\frac{\hbar^2}{2m_e} \sum_{1,2} \nabla_i^2 - \frac{\hbar^2}{2m_H} \sum_{1,2} \nabla_k^2 + V \right) \psi = E\psi \quad , \quad (6.1)$$

where the i -subscripts refer to electrons (mass m_e), the k -subscripts to nuclei (mass m_H) and V is the total potential energy, the sum of the electronic and the nuclear potential energy. The Born-Oppenheimer approximation takes advantage of the large mass ratio between an atomic nucleus and an electron. This allows an adiabatic approach, in which the electrons move in the field of fixed nuclei. In this approximation the electronic and nuclear wave functions can be separated:

$$\psi(\vec{x}_i, \vec{x}_k) = \psi_e(\vec{x}_i) \psi_{nr}(\vec{x}_k) \quad . \quad (6.2)$$

The wave equation can now be split into two parts, one describing the motion of electrons in the field of the fixed nuclei

$$\left(\frac{\hbar^2}{2m_e} \sum_i \nabla_i^2 + E_{el} - V_e \right) \psi_e = 0 \quad (6.3)$$

and an equation describing the motion of the nuclei under the potential $E_{el} + V_n$

$$\left(\frac{\hbar^2}{2} \sum_i \frac{1}{M_k} \nabla_k^2 + E_{v,J} - E_{el} - V_n \right) \psi_{vr} = 0 \quad (6.4)$$

Here $E_{v,J}$ denotes the vibrational (quantum number v) and rotational (quantum number J) energy of the molecule. Solving Eq. (6.4) leads to the term values of the vibrating rotator

$$\begin{aligned} \frac{E_{v,J}}{hc} &= \omega_e(v + \frac{1}{2}) - \omega_e x_e(v + \frac{1}{2})^2 + B_e J(J + 1) \\ &+ D_e J^2(J + 1)^2 - \alpha_e(v + \frac{1}{2})J(J + 1) + \dots \end{aligned} \quad (6.5)$$

where ω_e , $\omega_e x_e$, B_e , D_e , α_e are rovibrational molecular constants. Commonly this equation can be split in to a vibrational and a rotational part, the so-called term values

$$G(v) = \omega_e(v + \frac{1}{2}) - \omega_e x_e(v + \frac{1}{2})^2 + \dots \quad (6.6)$$

$$F_v(J) = B_v J(J + 1) - D_v J^2(J + 1)^2 + \dots, \quad (6.7)$$

in which

$$\begin{aligned} B_v &= B_e - \alpha_e(v + \frac{1}{2}) + \dots \\ D_v &= D_e + \dots \end{aligned} \quad (6.8)$$

In Eq. (6.6) and (6.7) the higher order contributions describe deviations from the harmonic oscillator and rigid rotator, respectively. In the electronic states relevant to the Fulcher α band $D_v \ll B_v$ and $\omega_e x_e \ll \omega_e$. This implies that for low values of v and J the models of the harmonic oscillator and rigid rotator are accurate and higher order terms can be neglected. The vibrational and rotational constants depend on the electronic state of the molecule (as indicated by the subscript e). The values of the molecular constants for the $X^1\Sigma_g^+$, the $a^3\Sigma_u^+$ and the $d^3\Pi_u$ state of hydrogen, used for the calculations of the term values are provided in table (6.1) [49]. In the following a superscript 0 to a symbol indicates that it is related to the electronic ground state of the molecule, 1 relates to the $d^3\Pi_u$ state and 2 to the $a^3\Sigma_u^+$ state.

6.2.1 Angular-momentum coupling: Hund's case (b)

The fine structure of a molecule is determined by interactions between the angular momenta of electrons, nuclei and their spins. In a molecule there is an

internal field along the internuclear axis, there is nuclear rotation, and orbital and spin angular momentum of the electrons. As a consequence, all angular momenta can influence each other and none of them may really be a constant of motion. Hund [50] has introduced a classification for several limiting coupling cases, the so-called Hund cases. Here only the Hund's case (b) will be treated, as this describes all molecular states relevant to the Fulcher α spectrum. In the Hund's case (b) the orbital angular momentum and the angular momentum of nuclear rotation are coupled to the internuclear axis, but the electron spin is not. If we ignore for a moment the electron spin influence, the total angular momentum is given by

$$\vec{K} = \vec{N} + \vec{\Lambda} \quad (6.9)$$

Here \vec{K} is the total angular momentum apart from spin, \vec{N} the angular momentum of nuclear rotation and $\vec{\Lambda}$ the component of the orbital angular momentum along the internuclear axis. The values that K can take are

$$K = \Lambda, \Lambda + 1, \Lambda + 2, \dots \quad (6.10)$$

Note that for the $d^3\Pi$ state this implies that $K = 0$ does not exist, as $\Lambda = 1$.

In principle if the electron spin $\neq 0$ this leads to a further splitting

$$\vec{J} = \vec{K} + \vec{S} \quad (6.11)$$

However, in the case of the Fulcher α band the triplet splitting is very weak and can be neglected in spectroscopic applications. As a consequence, K instead of J can be used as the effective quantum number.

6.2.2 Symmetry rules

Not all states are quantum-mechanically allowed. The total wave function describing the molecule has to obey certain symmetry rules. Consider the symmetry properties of the hydrogen molecule. The complete wave function can be represented by a product of five functions [51]

$$\psi = \begin{pmatrix} \text{electronic} \\ \text{orbital} \\ \text{motion} \end{pmatrix} \begin{pmatrix} \text{electronic} \\ \text{spin} \\ \text{orientation} \end{pmatrix} \begin{pmatrix} \text{nuclear} \\ \text{vibration} \end{pmatrix} \begin{pmatrix} \text{nuclear} \\ \text{rotation} \end{pmatrix} \begin{pmatrix} \text{nuclear} \\ \text{spin} \\ \text{orientation} \end{pmatrix} \quad (6.12)$$

The Pauli's Principle implies for the electrons, that the wave function must be anti-symmetric under exchange of two electrons. As only the first two functions of Eq. (6.12) involve electrons, these two must always have opposite symmetry. The nuclei of the hydrogen molecule are protons and also have half-integral spin. They also obey Fermi-Dirac statistics and the total wave function should also be anti-symmetric under exchange of the two nuclei.

Consider Eq. (6.12) under such an exchange. The second function, describing the electronic spin, does not depend on the nuclei. The vibration depends only on the internuclear distance and is always symmetric. The first function describes the electronic orbital motion. It is defined relative to the position of the nuclei, and can either be symmetric or antisymmetric under nuclear exchange. The corresponding symmetry property is called *gerade* or *ungerade* respectively. The symmetry of the rotational term of Eq. (6.12) depends on the characteristics of the electronic wave function. Another symmetry property is needed here: if reflection in a plane through the internuclear axis changes the sign of the electronic wave function, it is called *negative* (-), if the sign does not change it is called *positive* (+). For a homonuclear molecule like hydrogen, it can be shown that for *positive gerade* and *negative ungerade* states Σ_g^+ , Σ_u^- even rotational states are symmetric and odd are anti-symmetric. For Σ_u^+ and Σ_g^- states the opposite symmetry applies [49]. States Π , Δ , ... have a two-fold degeneracy due to Λ -type doubling. One of the levels of this splitting has a similar symmetry behaviour as a Σ^+ state and is designated Π^+ , Δ^+ , ..., the other behaves like a Σ^- state and is designated Π^- , Δ^- , ...

Finally consider the nuclear spin function. The spins of the nuclei can either be parallel, total nuclear spin $I = 1$, or antiparallel, $I = 0$. If the spins of the nuclei are parallel, their wave function is symmetric, otherwise it is anti-symmetric. It appears that these nuclear-spin states are only very slowly interconverted (timescale of months); one can distinguish two modifications of molecular hydrogen, *para-hydrogen* with nuclear spin 0 and *ortho-hydrogen* with nuclear spin 1. As the degeneracy of the nuclear spin function is $(2I+1)$, the ortho modification occurs three times more often than the para modification. For a homonuclear diatomic molecule as hydrogen this has some interesting consequences. The total wave function has to be anti-symmetric under exchange of two identical particles. Consider the ground electronic state $X^1\Sigma_g^+$. The first term from Eq. (6.12) is symmetric under exchange of nuclei. Even rotational levels have a symmetric wave function for Σ^+ states so in order to have an overall antisymmetric wave function the nuclear spin function must be antisymmetric; for the electronic ground state of hydrogen even rotational levels occur only for para-hydrogen. Similarly, odd rotational levels only occur for ortho-hydrogen. This results in an intensity-alternation in the rotational spectrum: as ortho-hydrogen occurs three times more than para, the odd rotational levels are three times more populated than the even levels. The $d^3\Pi_u$ has two series of levels due to Λ -splitting, the $d^3\Pi^+$ and the $d^3\Pi^-$. The symmetry properties discussed above have different consequences for the ortho- and para hydrogen. For ortho hydrogen odd rotational levels are only allowed for the negative series, even rotational levels occur only in the positive branch of the Λ -splitting. For the negative branch therefore the same intensity alternation is observed as for the ground state: odd

rotational levels occur three times more often than even rotational levels. For the positive branch the situation is reversed. The allowed levels with the appropriate symmetry properties are represented in Fig. (6.2).

6.3 Radiative transitions

In this section the radiative decay of excited molecular states is treated. In section 6.3.1 the selection rules for dipole transitions are summarized. Other than dipole transitions are not considered, as their amplitude is generally very low. Section 6.3.2 treats the line strengths of the radiation.

6.3.1 Selection rules

Selection rules for dipole transitions are related to the symmetry properties of the initial and final state as introduced in section (6.2.2). They are listed below:

- positive rotational terms combine only with negative

$$+ \longleftrightarrow - \quad + \longleftrightarrow + \quad - \longleftrightarrow - \quad (6.13)$$

- *gerade* electronic states combine only with *ungerade*

$$g \longleftrightarrow u \quad g \longleftrightarrow g \quad u \longleftrightarrow u \quad (6.14)$$

Here " \longleftrightarrow " means that the transition is allowed, " \longleftrightarrow " means that the transition is forbidden. Further selection rules can be deduced specific for Hund's case (b). In this case the quantum numbers Λ and S are defined. The corresponding selection rules are

$$\Delta\Lambda = 0, \pm 1 \quad (6.15)$$

$$\Delta S = 0 \quad (6.16)$$

The latter has as consequence that only states of the same multiplicity can combine with one another. Although this rule in general is not rigid, it is strict for the $X^1\Sigma_g$, $d^3\Pi_u$ and $a^3\Sigma_g$ state. As the triplet splitting is neglected the quantum number K is used, and its selection rule is

$$\Delta K = 0, \pm 1 \quad (6.17)$$

The branch with $\Delta K = 0$ is called the Q -branch, the branches with $\Delta K = +1, -1$ are called P and R branch respectively. Note that in order to satisfy Eqs. (6.13) and (6.17) simultaneously, the electronic wave function has to reverse for Q branch transitions ($\Pi^- \rightarrow \Sigma^+$).

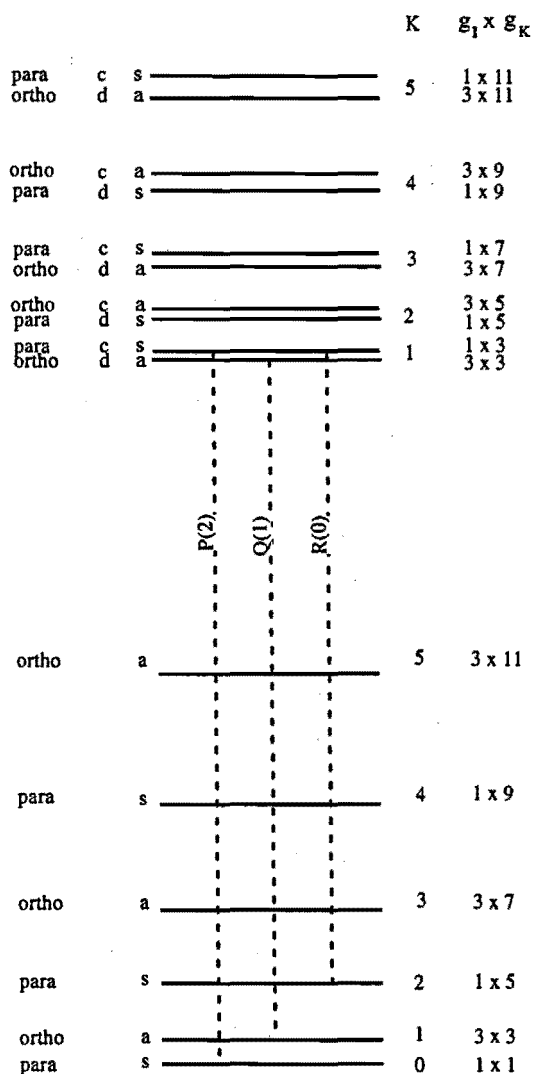


Figure 6.2. Transition scheme of the ${}^1\Pi_u \rightarrow {}^1\Sigma_g^+$ transition. P, Q, and R denote the three possible rotational branches in a radiative transition. The total statistical weight of a rotational state is the product of the nuclear spin degeneracy g_1 and the rotational degeneracy $g_K = 2K + 1$ (cf. next section).

6.3.2 Line strengths

A general expression for the intensity of a molecular line is given by [49]

$$I_{n''}^{n'} = \frac{64\pi^4\nu^3}{3h} \frac{1}{2J'+1} N_{n'} A_{n''}^{n'} \quad (6.18)$$

The intensity is given in photons $\text{m}^{-3}\text{s}^{-1}$. $N_{n'}$ is the number density of a state $n' = n'(e', v', K')$. The upper and lower level of the transition are denoted by n' and n'' respectively. $A_{n''}^{n'}$ is the transition probability for spontaneous emission. In the Born-Oppenheimer approximation the transition moment can be separated into an electronic, a vibrational and a rotational part [52]

$$\begin{aligned} A_{n''}^{n'} &= \sum |R_{n''}^{n'}|^2 = |R_e^{e'e''}|^2 |R_v^{v'v''}|^2 \sum |R_r^{J'J''}|^2 \\ &= A_{e'e''} q_{v'v''} S_{J'J''} \end{aligned} \quad (6.19)$$

The $q_{v'v''}$ are the so-called Franck-Condon factors, that describe the distribution over the various vibrational transitions in the Fulcher band. They are tabulated in table (6.5). The Hönl-London factors describe the line strengths of the rotational transitions. Hönl-London factors have a very simple form in a pure Hund's case (b) [52]:

$$\begin{aligned} S_{J,J+1} &= \frac{J}{2} && \text{(P-branch)} \\ S_{J,J} &= \frac{2J+1}{2} && \text{(Q-branch)} \\ S_{J,J-1} &= \frac{J+1}{2} && \text{(R-branch)} \end{aligned} \quad (6.20)$$

The expression for the intensity of a molecular line Eq. (6.18) can now be written as

$$I_{n''}^{n'} = \frac{64\pi^4\nu^3}{3h} \frac{1}{2J'+1} A_{e'e''} q_{v'v''} S_{J'J''} N_{n'} \quad (6.21)$$

This expression can be simplified for the Q lines, as the Hönl-London factors are $2J'+1$ in this case

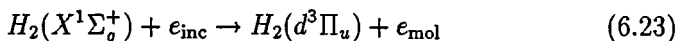
$$I_{n''}^{n'} = \frac{64\pi^4\nu^3}{3h} A_{e'e''} q_{v'v''} N_{n'} \quad (6.22)$$

6.4 Direct excitation process

A semi-empirical method is adapted here to determine the excitation cross-sections for transitions $n(e^0, v^0, K^0) \rightarrow n(e', v', K')$: the dependence on vibration and rotation follows from an adiabatic approximation combining theoretical and experimental results. As the energy difference between the initial and final state depends on the initial and final rovibrational states, the

distribution over the excited state is also depending on the electron energy distribution function (EEDF). This matter will be addressed for thermal EEDF's.

In figure 6.1 the excitation is indicated as an electron collision induced process, the direct excitation. The excitation of the $d^3\Pi_u$ state by direct electron impact on the ground state involves a change in the spin multiplicity. A singlet-triplet transition in the excitation process can only occur through exchange of an incident electron with an electron in the molecule. The spin of the two exchanging electrons must be antiparallel [53]. This can be expressed by



Unlike most other molecules, hydrogen can have a significant change in rotation during the direct excitation, as the small mass of the hydrogen atoms makes momentum transfer from the incoming electron possible¹.

6.4.1 Direct excitation: semi-empirical treatment

Starting point is the theoretical treatment for electron excitation cross sections derived in the sudden approximation by Ostrovsky and Ustinov [55]. Based on this treatment the theoretical expression for the $d^3\Pi \leftarrow X^1\Sigma$ transition in the hydrogen molecule is:

$$\begin{aligned} \sigma_{\Pi_{v',K'}^{\pm} \leftarrow \Sigma_{v^0,K^0}^+}(\varepsilon - \varepsilon_{thr}) &= \frac{1}{2} [1 \mp (-1)^{K'+K^0}] (2K' + 1) \\ &\times \sum_{L \geq 1} \begin{pmatrix} K' & L & K^0 \\ 1 & -1 & 0 \end{pmatrix}^2 \sigma_{\Pi_{v',L} \leftarrow \Sigma_{v^0,0}^+}(\varepsilon - \varepsilon_{thr}) \end{aligned} \quad (6.24)$$

In this equation L characterizes the order of the transition multipole from the final to the initial state, e.g. $L = 1$ for a dipole transition. The term

$$\begin{pmatrix} K' & L & K^0 \\ \Lambda & -\Lambda & 0 \end{pmatrix} \quad (6.25)$$

¹This change in rotation due to electron impact has been demonstrated experimentally by Otorbaev et al. [54]. In their experiments the gas temperature is kept at values for which only the lowest rotational levels (1 for ortho- and 0,2 for para hydrogen) are expected to be populated, and yet a full developed rotational distribution was observed in the Fulcher α emission spectrum. This point is of great importance for the interpretation of the measured spectra and we will come back to this later. We note that even more direct evidence for this rotational excitation through electron impact is found in the sheer existence of the P and R bands. In the ground state the rotational quantum number must always be odd for ortho and even for para hydrogen, without a change in rotation this must also be true for the $d^3\Pi$ states. However, all P and R lines originate from states, which have even rotational quantum numbers for ortho hydrogen and odd for para hydrogen. These levels can therefore only be populated from the ground state if the electronic excitation is accompanied by a rotational (de-)excitation. As the strength of the P and R band are comparable to the Q bands the coupling must be important.

is a scalar, the so-called 3-j symbol. It is tabulated in [56]. The energy is given as $\varepsilon - \varepsilon_{thr}$, the energy above excitation threshold. This is convenient as the threshold energy depends on the rovibrational energies of the initial and final state of the transition ². With Eq. (6.24) the excitation cross section $\sigma_{\Pi_{v',K'} \leftarrow \Sigma_{v^0,K^0}^+}(\varepsilon - \varepsilon_{thr})$ of any rovibrational transition can be calculated directly, provided the excitation cross sections starting from the ground rotational state, $\sigma_{\Pi_{v',L} \leftarrow \Sigma_{v^0,0}^+}(\varepsilon - \varepsilon_{thr})$ are known. Here L , the order of the transition multipole, takes the place of K' . The latter can be simplified, using the fact that the electronic transition time is very short in relation to rotational or vibrational movement of the nuclei. In this so-called Franck-Condon approach electronic, rotational and vibrational excitation are treated independently:

$$\sigma_{\Pi_{v',L} \leftarrow \Sigma_{v^0,K^0}^+}(\varepsilon - \varepsilon_{thr}) = \sigma_{\Pi \leftarrow \Sigma}(\varepsilon - \varepsilon_{thr}) q_{v^0 v'} Q_L \quad (6.26)$$

The total electronic excitation cross section $\sigma_{\Pi \leftarrow \Sigma^+}(\varepsilon - \varepsilon_{thr})$ for the $d^3\Pi$ state is

$$\sigma_{\Pi \leftarrow \Sigma}(\varepsilon - \varepsilon_{thr}) = b f(\varepsilon - \varepsilon_{thr}) \quad (6.27)$$

where b is the maximum of the excitation cross section and $f(\varepsilon - \varepsilon_{thr})$ is a form function. The threshold energy ε_{thr} accounts for the vibrational and rotational energy difference of the lower and upper of the excitation in this definition. The vibrational terms $q_{v^0 v'}$ are the Franck-Condon factors, that describe the redistribution of the ground vibrational states over the excited state. The Franck-Condon factors are normalized for summation over v^0 or v' . They are tabulated in table (6.2). The Q_L are factors that represent the rotational part of the $\sigma_{\Pi_{v',L} \leftarrow \Sigma_{v^0,0}^+}(\varepsilon - \varepsilon_{thr})$ in Eq. (6.26).

These are tabulated in table 6.3. The total rotational part in Eq. (6.24) then equals

$$R_{K^0 K'} = \left[\frac{1 \mp (-1)^{K'+K^0}}{2} \right] (2K'+1) \times \sum_{L \geq 1} \begin{pmatrix} K' & L & K^0 \\ 1 & -1 & 0 \end{pmatrix}^2 Q_L \quad (6.28)$$

The Q_L are scaled such that the rotational part of Eq. (6.24) is normalized:

$$\sum_{K'} R_{K^0 K'} = 1 \quad (6.29)$$

The $R_{K^0 K'}$ are given in table 6.4. From the above an expression for the excitation rate coefficient from a state (v^0, K^0) to a state (v', k') can be formulated:

$$k_{v',K'}^{v^0,K^0} = R_{K^0 K'} q_{v^0 v'} \int_{\varepsilon_{thr}}^{\infty} F_e(\varepsilon) b f(\varepsilon - \varepsilon_{thr}) d\varepsilon \quad (6.30)$$

²Note that the \pm and \mp in the formula imply that the $d^3\Pi^+$ state can only be excited from transitions with odd $\Delta K = K - K'$ and the $d^3\Pi^-$ state only from transitions with even ΔK . This is in agreement with the symmetry rules discussed before (cf. section 6.3.1).

6.5 Thermal rotational and vibrational populations

The vibrational distribution function in the case of a thermal vibrational population is given by

$$f_v = \frac{1}{Q_v} e^{-G(v)hc/kT_{vib}} \quad (6.31)$$

with $G(v)$ the term value in cm^{-1} as defined in Eq. (6.6), c the speed of light in cm/s , and Q_v the vibrational partition function

$$Q_v = \sum_v e^{-G(v)hc/kT_{vib}} \quad (6.32)$$

Thermal vibrational distribution functions for the electronic ground state of hydrogen are plotted in Fig. 6.3 for different vibrational temperatures. Below 0.2 eV the vast majority of the molecules is in the vibrational ground

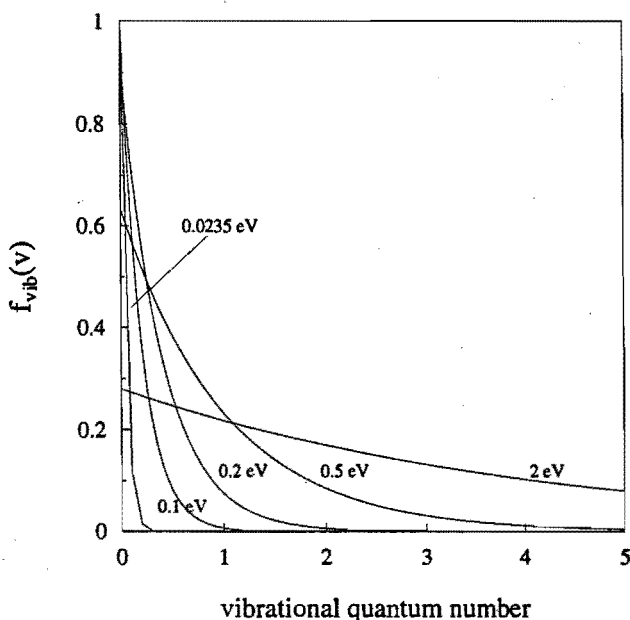


Figure 6.3. Ground state vibrational distribution functions for different vibrational temperatures.

state. Above this temperature also higher vibrational states are populated.

The rotational levels are degenerate by a factor of $(2K + 1)$. Even rotational levels occur only for para-hydrogen in the electronic ground state,

odd only for ortho-hydrogen. The degeneracy due to the nuclear spin I is $g_I = 2I + 1$. For para-hydrogen $I = 0$, for ortho-hydrogen $I = 1$. The rotational distribution function is

$$f_K = \frac{g_I(2K + 1)}{Q_r} e^{-F(K)hc/kT_{rot}} \quad (6.33)$$

Here $g_I = 1$ must be substituted for even rotational levels and $g_I = 3$ for odd rotational levels. $F(K)$ is the rotational energy term and Q_r the rotational partition function

$$Q_r = \sum_K g_I(2K + 1) e^{-F(K)hc/kT_{rot}} \quad (6.34)$$

Thermal rotational distribution functions for the electronic ground state of hydrogen are plotted in Fig. 6.4 for different rotational temperatures. Already at room temperature ($T_{rot} \simeq 0.0235$ eV) there is a well developed ro-

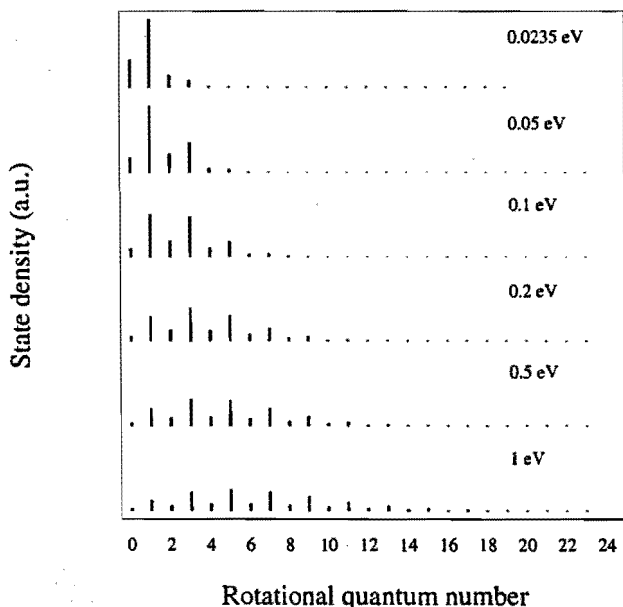


Figure 6.4. Ground state rotational distribution functions for different rotational temperatures. The intensity alternation is a consequence of the nuclear spin degeneracy. It is 1 for even rotational states, that only occur for para hydrogen, and 3 for odd rotational states, that only occur for ortho hydrogen.

tational state distribution. At higher rotational temperatures the maximum of the distribution function shifts towards higher K numbers; the degeneracy

term $2K + 1$ initially dominates over the Boltzmann-exponent $e^{-F(K)hc/kT_{rot}}$ in Eq. (6.33). The density of molecules with a high rotational energy can be large due to this $2K + 1$ factor. Especially for molecular reactions that require a significant internal energy of the molecules this is an important observation.

6.6 Applications

The density of excited states is related to a balance equation. The discussion is limited here to plasma conditions under which the levels relevant to the Fulcher α band are in the *Corona phase*: all population of the excited state occurs through electron impact excitation from the ground state, all decay is radiative. The balance equation for a rovibrational state of the $d^3\Pi$ level then equals

$$\frac{dn_{d^3\Pi(v',K')}}{dt} = n_e \sum_{v^0} \sum_{K^0} n^0(v^0, K^0) k_{v',K'}^{v^0, K^0} - n'(v', K') \sum_{v''} \sum_{K''} A_{v'',K''}^{v',K'} \quad (6.35)$$

In a quasi-steady state approximation excitation and radiation balance [57]:

$$n_e \sum_{v^0} \sum_{K^0} n^0(v^0, K^0) k_{v',K'}^{v^0, K^0} = n'(v', K') \sum_{v''} \sum_{K''} A_{v'',K''}^{v',K'} \quad (6.36)$$

In relation to this balance equation the vibrational and rotational structure are discussed. An actinometric method to determine the dissociation degree of the plasma is introduced.

6.6.1 Vibration

Combining Eqs. 6.26 and 6.31, the vibrational population of the excited state is related to the ground state distribution by

$$f'_v(v') \propto \sum_{v^0} q_{v^0, v'} f_v(v^0) e^{-\Delta E_{vib}/kT_e} \quad (6.37)$$

Here $e^{-\Delta E_{vib}/kT_e}$ accounts for the difference in vibrational energies of the transitions, if a Maxwellian EEDF with a temperature T_e is assumed. The intensity distribution is determined by the Franck-Condon factors of the decay process:

$$I_{v',v''} \propto f'_v(v') q_{v',v''} \quad (6.38)$$

Here the relation between the ground state vibrational distribution and the observed intensity distribution is subject to discussion. The vibrational distribution functions in Fig. 6.3 show that below a vibrational temperature of 0.2 eV almost all molecules are in the vibrational ground state. Above this

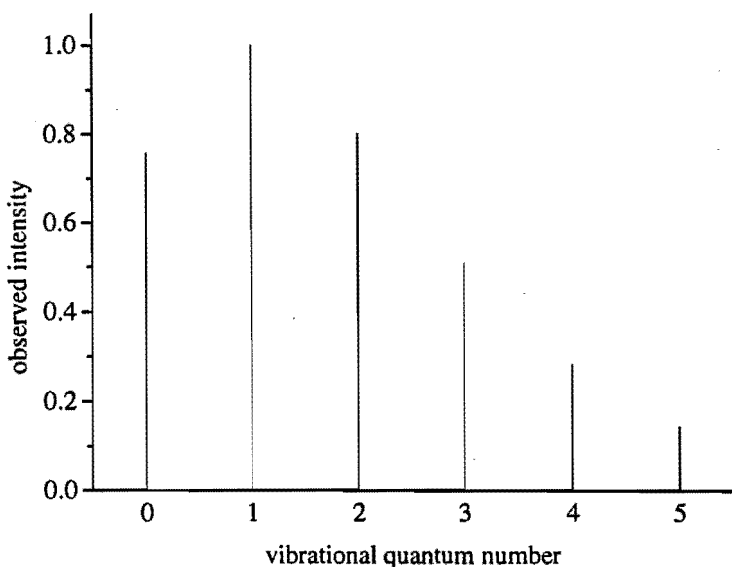


Figure 6.5. *The computed intensity distribution in the vibrational spectrum if all molecules in the electronic ground state have $v = 0$. The vibrational structure is a consequence of the Franck-Condon factors in the electron excitation process and the radiative decay.*

temperature a vibrational distribution is developed. Fig. 6.5 shows the computed vibrational intensity distribution observed in emission of the Fulcher α band if all molecules in the electronic ground state have $v = 0$. An electron temperature of 3 eV has been used in the computations. Apparently in the spectrum a full developed vibrational structure is observed, even though the vibrational temperature of the ground state is low. The reason for this is found in the Franck-Condon factors, describing the vibrational transition probabilities in the excitation process (table (6.2)). There is no preference for vibrational transitions $\Delta v = 0$ in the excitation of hydrogen. This is due to the fact that the potential curve of the $d^3\Pi$ state is both shifted and different in shape than that of the $X^1\Sigma$ state (cf. Fig. 6.1, [58]). Fig. 6.6 shows the influence of the ground state vibrational temperature on the observed spectrum. The intensities for the different vibrational temperatures are normalized on the intensity of the $v', v'' = 1$ band intensity in the situation with zero vibrational temperature. At increasing vibrational temperature especially the level $v^0 = 1$ will become populated. As can be seen from the Franck-Condon factors from table 6.2 this will lead to a stronger input to $v' = 0$ and a decrease of $v' = 2, 3, 4, 5$. Above 0.2 eV this effect becomes significant.

Another issue is non-thermal vibrational distributions in the electronic

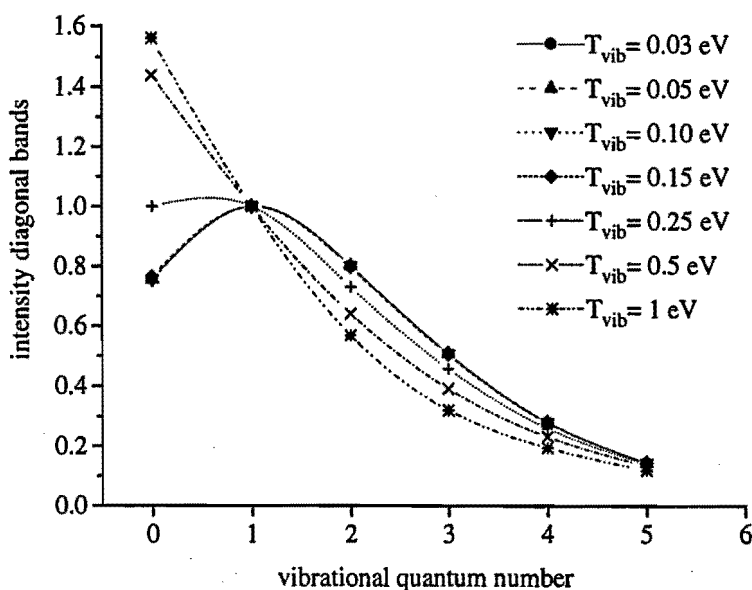


Figure 6.6. *The influence of the ground state vibrational temperature on the computed intensity distribution. The intensities are normalized on the intensity computed at $T_{vib} = 0$.*

ground state. To get a feeling of the sensitivity of the observed spectral intensity distribution for non-thermal ground state vibrational populations, the intensity distribution is calculated for 10% populations of the levels $v^0 = 1, 2, 3, 4$ respectively with the other 90% of the ground state molecules in $v^0 = 0$. The result is shown in Fig. 6.7. Apparently non-equilibrium inputs on $v^0 = 1..4$ all have similar effects on the intensity distribution, i.e. an increased intensity at $v' = 0$ and a decrease at $v' = 2, 3, 4$. Therefore it is concluded that distributions of ground state vibrational levels that are non-thermal can not be distinguished from thermal distributions from the observed spectrum.

In the Fig.'s 6.5-6.7 an electron temperature of 3 eV was assumed. The influence of the electron temperature on the vibrational intensity distribution is presented in Fig. 6.8. For any electron temperature above 2 eV the maximum error made by assuming 3 eV is smaller than 10% for any vibrational intensity $v' = 0..5$. Only if the electron temperature is below 2 eV the error can become larger. In most practical applications where the Corona assumption is valid, there will hardly be a molecular spectrum observed at these lower temperatures, as the excitation rates will be very low.

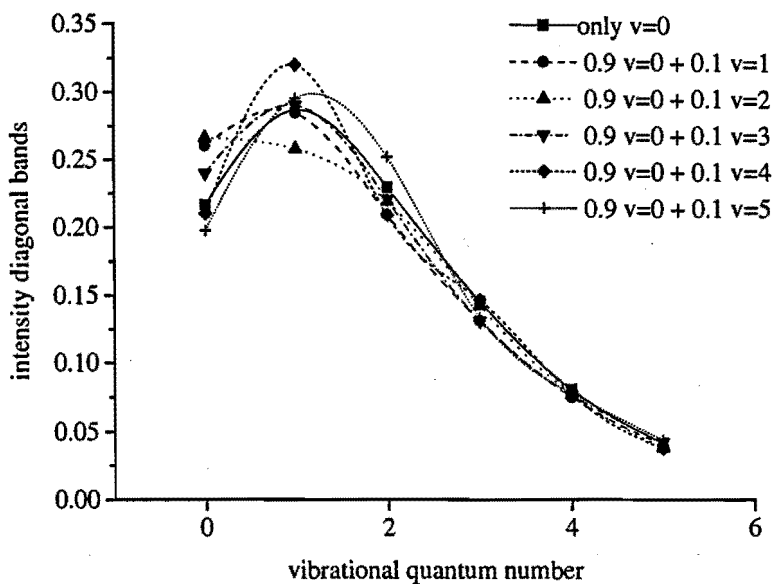


Figure 6.7. *The influence of non-thermal vibrational distributions on the observed intensity distribution.*

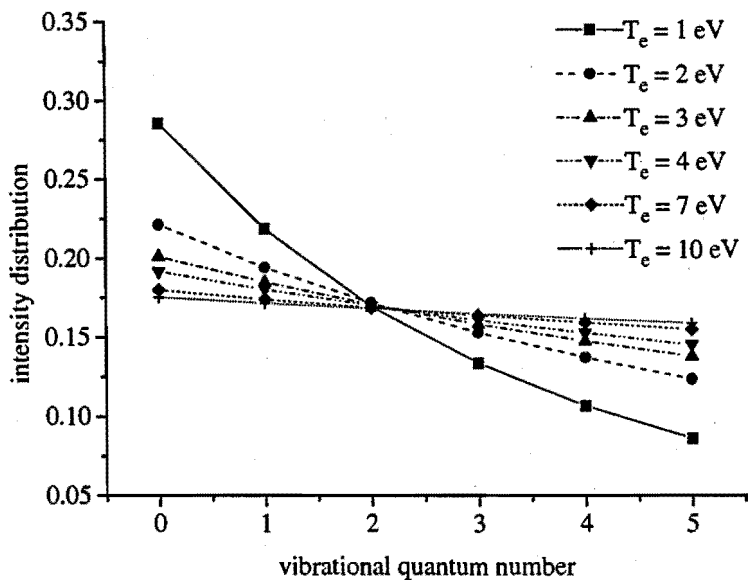


Figure 6.8. *The influence of the electron temperature on the observed intensity distribution.*

6.6.2 Rotation

If the differences in threshold energy for the different rotational states are neglected ($\varepsilon - \varepsilon_{thr} \leq 0.1$ eV in all cases), the $R_{K^0 K'}$ from table 6.4 relate the excited state rotational distribution f_{rot}^0 to the ground state rotational distribution f'_{rot} :

$$f'_{rot}(K') = \sum_{K^0} R_{K^0 K'} f_{rot}^0(K^0) \quad (6.39)$$

The intensity distribution of rotational lines in a vibrational band now follows from Eq. (6.18). If we restrict ourselves to the Q lines ($d^3\Pi^-$ series) the Hönl-London factor simply becomes $2K' + 1$ (cf. Eq. (6.20)) and the line intensity is given by

$$I_{K'=K''} \propto \nu^3 f'_{rot}(K') \quad (6.40)$$

The relation between the ground state rotational distribution and the observed rotational spectrum will be discussed starting from a thermal ground state population. Fig. 6.9 (a) shows rotational populations of the ground and upper state at $T_{rot} = 300$ K. The distribution function of the $d^3\Pi$ state is somewhat broadened compared to the ground state. In a Boltzmann plot a thermal distribution is represented by a straight line. The broadened upper level distribution will give a slightly hollow profile. This is seen in Fig. 6.9 (b). If the rotational population of the electronic ground state is thermal, the corresponding rotational temperature can be determined from the experimentally determined f'_{rot} . An iterative method can be applied, that searches the temperature that minimizes the discrepancy between the experimentally determined f'_{rot} and the calculated one. An additional feature of this approach is that it can be applied to any subset of rotational states K' . For example, if only the levels $K' = 1, 2, 4$ can be determined accurately (e.g. due to overlap of the $K' = 3$ line and weakness of lines with $K' \geq 5$) the above fit procedure is applied to these levels only.

A quicker and cruder way to determine the rotational temperature is found in figure 6.10. In this figure all state densities are calculated from a thermal distribution in the ground state. Although the hollow shape of a Boltzmann plot (Fig. 6.9) shows that the rotational state distribution is not thermal, still an effective rotational temperature was derived from it by a linear fit. The figure gives the ratio between the rotational temperatures determined from the rotational distribution functions from the excited levels and the rotational temperature from the ground state. For both the temperature determination of the upper and ground state the rotational constants from the ground state were used. As the excitation process gives a diffuse image of the ground state distribution, the higher states will be overpopulated and the effective temperature will be too high. This effect is strongest at low temperatures, when the rotational distribution function is narrow. Note that this crude method can also be applied for subsets of rotational states. As an

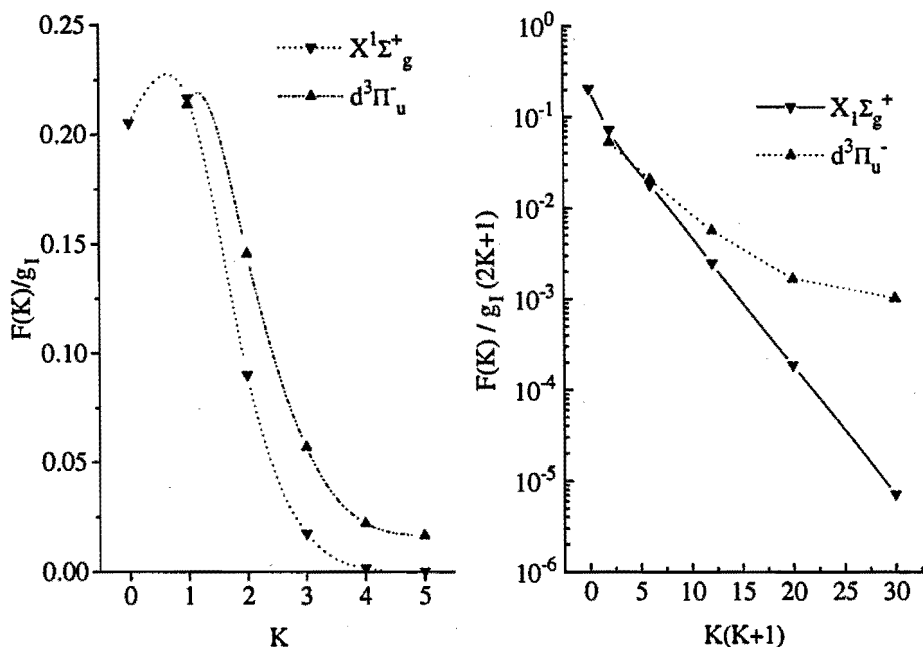


Figure 6.9. (a) Calculated rotational distribution function of the electronic ground state $X^1\Sigma_g^+$ (solid line) and of the $d^3\Pi_u^+$ state (dashed line) after electron impact excitation. A ground state temperature of 0.0235 eV was assumed. The population densities are normalized on the nuclear spin statistical weight. (b) Boltzmann plot from the same data.

example, this is done in Fig 6.10 for the excited rotational levels $K' = 2, 4, 5$.

Finally the issue of non-thermal ground state rotational distributions needs to be addressed. The inverse matrix of $R_{K^0K'}$ seems to enable the determination of the ground state rotational distribution from an experimentally determined rotational distribution of the excited level. However, a number of reasons make this not feasible. One principal reason is that the number of bound rotational states is larger for the ground state than for electronic excited states, making the inversion operation underdetermined. Limitations are also found from an experimental point of view: levels with higher K' will be weak in emission, and in the molecular spectrum of hydrogen some spectral lines will be likely to be overlapping with lines from other bands.

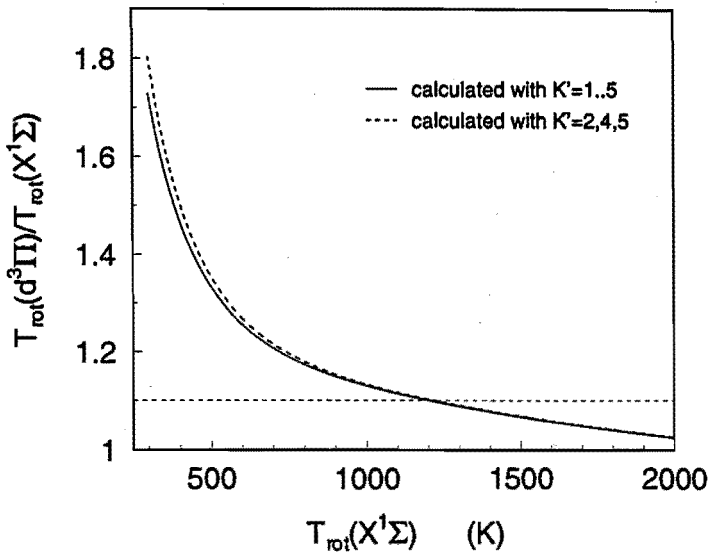


Figure 6.10. Ratio of the effective rotational temperature of the $d^3\Pi_u$ and ground state as a function of the rotational temperature of the ground state.

6.6.3 Actinometry

The observation of a molecular spectrum in a plasma implies a sufficient amount of high energetic electrons. If atomic hydrogen is present, there will also be an atomic spectrum. Under certain conditions the ratio of atomic to molecular line intensity can be used to determine the dissociation degree of the plasma: actinometry on H and H_2 . A first condition to do this, is that the observed spectral emissivity originates from levels that are in the Corona phase [23]: excitation is strongly dominated by collisions, deexcitation is radiative. A second condition is that the dissociation degree is not too low, as there is always some dissociative excitation from molecules, giving an atomic spectrum. Also recombination processes can populate excited atomic levels.

In the following the radiative excitation rates for atomic and molecular hydrogen will be discussed. As the excitation processes for the two are not identical in threshold and energy dependence, some additional steps must be taken before the line intensity ratios can be related to the dissociation degree.

In the Corona phase the balance equation of an atomic level p reads:

$$\left(\frac{dn_p}{dt}\right)_{exc} = n_e n_H k_p - n_p \sum_{r < p} A_{pr} \quad (6.41)$$

The excitation rate coefficient of atomic hydrogen from the ground state to an excited level p is given by

$$k_p = \langle \sigma_p v_e \rangle = \int_{E_p}^{\infty} \sigma_p^{max} f_p(\varepsilon) \varepsilon^{1/2} F_e(\varepsilon) d\varepsilon \quad (6.42)$$

Here $F_e(\varepsilon)$ is the electron energy distribution function. The excitation cross section σ_p is written as the product of the maximum of the cross section σ_p^{max} and a form function $f_p(\varepsilon)$. E_p is the threshold energy for excitation of the level p . Using $\sum_{r < p} A_{pr} = \tau_p^{-1}$, τ_p being the radiative lifetime of state p , and Eqs. (6.41) and (6.42) the intensity of the emission I_{pq} in a stationary state equals

$$I_{pq} = A_{pq} \tau_p n_e n_H \int_{E_p}^{\infty} F_e(\varepsilon) \sigma_p^{max} f_p(\varepsilon) d\varepsilon \quad (6.43)$$

For the excitation of the molecular Fulcher α band a similar treatment is followed. It is common use in literature [53] to give the radiative lifetime and excitation cross section for the entire Fulcher α band, summed over all vibrational and rotational states. The total band intensity is in analogy to Eq. (6.43):

$$I_{d^3\Pi} = n_e n_{H_2} \int_{E_{d^3\Pi}}^{\infty} F_e(\varepsilon) \sigma_{d^3\Pi}^{max} f_{d^3\Pi}(\varepsilon) d\varepsilon \tau_{d^3\Pi} \quad (6.44)$$

Here $\sigma_{d^3\Pi}^{max} f_{d^3\Pi}(\varepsilon)$ is the excitation cross section for the entire $d^3\Pi$ band, summed over all rotational and vibrational levels. For actinometric applications it is more convenient to relate the intensity of one atomic line to one molecular line, i.e. one rovibrational transition. The fraction of molecules that is observed in a vibrational emission band $v'v''$ is represented by $q_{v^0v'} q_{v'v''}$. The fraction of molecules observed within one vibrational band in one rotational line relative to the full rotational distribution is $f'_{rot}(K')/Q'_{rot}$. The intensity of one spectral line can now be written as

$$I_{F_{v',K'-v'',K''}} = q_{v^0v'} q_{v'v''} \frac{f'_{rot}(K')}{Q'_{rot}} n_e n_{H_2} \tau_{d^3\Pi} \int_{E_{d^3\Pi}}^{\infty} F_e(\varepsilon) \sigma_{d^3\Pi}^{max} f_{d^3\Pi}(\varepsilon) d\varepsilon \quad (6.45)$$

The ratio of the intensity of an atomic and a molecular line can now be related to the density ratio H/H_2

$$\frac{I_{pq}}{I_{n'n''}} = \frac{n_H}{n_{H_2}} \times \frac{A_{pq} \tau_p}{q_{v^0v'} q_{v'v''} \tau_{d^3\Pi} F'_{rot}(K')/Q'_{rot}} \times \frac{\sigma_p^{max} \int_{E_p}^{\infty} F_e(\varepsilon) f_p(\varepsilon) d\varepsilon}{\sigma_{d^3\Pi}^{max} \int_{E_{d^3\Pi}}^{\infty} F_e(\varepsilon) f_{d^3\Pi}(\varepsilon) d\varepsilon} \quad (6.46)$$

The first fraction at the right hand side of Eq. 6.46 is to be determined. The second fraction consists of known constants except for Q'_{rot} and $F'_{rot}(K')$, that can be determined from experimentally determined rotational bands. The last fraction concerns the electronic excitation processes of the atomic and

molecular states. A convenient situation is found if the atomic and molecular spectral line have similar excitation processes, i.e. identical threshold energies and similarly shaped excitation cross sections. This situation is not found for hydrogen. The molecular levels have slightly higher energies than the atomic and also the form of the excitation cross section is different. The exact shape of the form function at the high energy side is not important, as the EEDF is exponentially decreasing. Only the near-threshold behaviour of the form functions is important. As both excitation reactions are resonant processes. The cross sections are expected to increase very fast to their maximum. For the excitation of the atomic $p = 3$ state experiments and calculations confirm that within a few hundreds of an eV the cross section reaches its maximum [59]. Near-threshold behaviour of the excitation of the molecular $d^3\Pi$ state has not been resolved yet. However, the excitation occurs in an exchange collision and this type of collisions is known to have very steep near-threshold behaviour. Therefore it seems allowed to leave out the form functions in Eq. (6.46) and use only the maximum values of the cross sections. The difference in threshold energy can be compensated for by a correction factor

$$C_{thr}(\varepsilon) = \frac{\int_{E_p}^{\infty} \varepsilon^{1/2} F_e(\varepsilon) d\varepsilon}{\int_{E_{d^3\Pi}}^{\infty} \varepsilon^{1/2} F_e(\varepsilon) d\varepsilon} - 1 = \frac{\int_{E_p}^{E_{d^3\Pi}} \varepsilon^{1/2} F_e(\varepsilon) d\varepsilon}{\int_{E_{d^3\Pi}}^{\infty} \varepsilon^{1/2} F_e(\varepsilon) d\varepsilon} \quad (6.47)$$

For a Maxwellian electron energy distribution function this correction factor is given as a function of electron temperature in Fig. 6.11. With this correction factor Eq. 6.46 can finally be written as

$$\frac{I_{pq}}{I_{n'n''}} = \frac{n_H}{n_{H_2}} \times \frac{A_{pq} \tau_p}{q_{v^0 v'} q_{v' v''} \tau_{d^3\Pi} F'_{rot}(K') / Q'_{rot}} \times \frac{\sigma_p^{max}}{\sigma_{d^3\Pi}^{max}} \times (1 + C_{thr}(\varepsilon)) \quad (6.48)$$

With this expression the ratio of atomic-to-molecular hydrogen in a plasma can be determined from a measured atomic spectral line and a rotational molecular band.

6.7 Spectroscopic data

In order to interpret the Fulcher α spectrum, data are required concerning the molecular structure, the excitation process and concerning the radiative decay. These are summarized here.

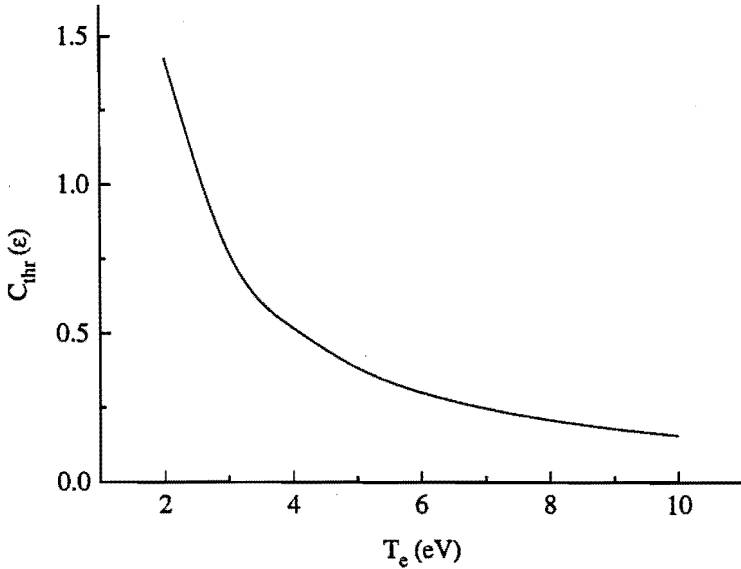


Figure 6.11. Correction factor that compensates different excitation rates due to different threshold energies for the atomic H_{α} and the molecular $Q_{(0-0)(1)}$ band head.

State	T_e	ω_e	$\omega_e x_e$	B_e	α_e
$d^3\Pi_u$	112702	2371.58	66.27	30.364	1.545
$a^3\Sigma_u^+$	107777	2664.83	71.65	34.261	1.671
$X^1\Sigma_g^+$	0	4395.2	117.99	60.809	2.993

Table 6.1. Molecular constants of hydrogen in the $d^3\Pi_u$, the $a^3\Sigma_u^+$ and the $X^1\Sigma_g^+$ state in cm^{-1} after [49]. In spectroscopic notation T_e is the minimum of the potential curve. It must not be confused with the same symbol indicating the electron temperature in plasmas.

Molecular constants

The term values as defined in section 6.2 are given in table (6.1).

Excitation process

For the excitation process, the excitation cross section for the entire band, measured by De Heer and Möhlmann is taken. The redistribution over vibrational states is governed by the Franck-Condon factors from the $X^1\Sigma_g^+$ state to the $d^3\Pi$ state. Finally, the rotational excitation is ruled by the Q_L

	$v'' = 0$	$v'' = 1$	$v'' = 2$	$v'' = 3$	$v'' = 4$	$v'' = 5$
$v' = 0$	0.1084	0.3018	0.3339	0.1889	0.0573	0.0091
$v' = 1$	0.1817	0.1557	0.0001	0.1727	0.2932	0.1580
$v' = 2$	0.1867	0.0217	0.0955	0.0954	0.0144	0.2455
$v' = 3$	0.1537	0.0026	0.1112	0.0001	0.1233	0.0190
$v' = 4$	0.1122	0.0294	0.0534	0.0467	0.0462	0.0488
$v' = 5$	0.0772	0.0526	0.0111	0.0757	0.0000	0.0811

Table 6.2. Franck-Condon factors for the excitation process after [60].

factors introduced in section 6.4. These are given in table (6.3). The matrix

L	1	2	3	4
Q_L	0.76	0.12	0.10	0.014

Table 6.3. Q_L factors, that weigh the contributions of the various multipole transitions to the rotational excitation in the excitation of the Fulcher α band. Data after [54].

elements $R_{KK'}$ that are calculated from these Q_L and the $3 - J$ symbols are given in table 6.4. Note that the matrix elements with indices that have even

	$K'' = 1$	$K'' = 2$	$K'' = 3$	$K'' = 4$	$K'' = 5$	$K'' = 6$
$K' = 0$	0.760	0.122	0.101	0.014	$< 10^{-4}$	$< 10^{-4}$
$K' = 1$	0.416	0.423	0.079	0.005	0.007	$< 10^{-4}$
$K' = 2$	0.130	0.407	0.345	0.066	0.044	0.006
$K' = 3$	0.033	0.147	0.402	0.309	0.061	0.040
$K' = 4$	0.010	0.036	0.163	0.401	0.290	0.058
$K' = 5$	0.001	0.013	0.038	0.219	0.400	0.277

Table 6.4. $R_{K'K''}$ matrix describing the change of the rotational quantum number in the electron excitation of the Fulcher α band.

$K - K'$ concern only the excitation of the Q lines, and the matrix elements with indices that have odd $K - K'$ concern only the excitation of the P and R lines.

Radiative decay

The $d^3\Pi_u$ state can only decay to the $a^3\Sigma_g^+$ state; therefore the Fulcher α band is the only emission observed from the $d^3\Pi_u$ state. The lifetime of this level is therefore determined experimentally from the decay times of the Fulcher band. For the $d^3\Pi_u^-$ state (Q lines) the lifetime is 40 ± 3 ns [61, 62]. The $d^3\Pi_u^+$ states (P, R lines) are disturbed by interaction with the $e^3\Sigma_u^+$ state and show anomalies in the intensity distribution. The vibrational line strengths are determined by the Franck-Condon factors for the transition $d^3\Pi_u \rightarrow a^3\Sigma_g$. These are tabulated in table 6.5. The rotational dependence

	$v'' = 0$	$v'' = 1$	$v'' = 2$	$v'' = 3$	$v'' = 4$	$v'' = 5$
$v' = 0$	0.93058	0.06863	0.00078	0.00000	0.00000	0.00000
$v' = 1$	0.06414	0.79842	0.13516	0.00226	0.00001	0.00000
$v' = 2$	0.00485	0.11677	0.67463	0.19937	0.00433	0.00003
$v' = 3$	0.00039	0.01423	0.15683	0.56046	0.26113	0.00687
$v' = 4$	0.00003	0.00171	0.02725	0.18385	0.45689	0.32038
$v' = 5$	0.00000	0.00020	0.00448	0.04251	0.19799	0.36464

Table 6.5. Franck-Condon factors for the radiative decay process $X_1\Sigma \leftarrow d^3\Pi$ after [63].

of the line strengths is determined by the Hönl-London factors that are given in Eq. (6.20).

Fulcher α spectroscopy at FOMSCE

7.1 Introduction

This chapter reflects results of molecular spectroscopy performed on the surface conversion experiment at the FOM institute for atomic and molecular physics (AMOLF), Amsterdam. The FOM Surface Conversion Experiment (FOMSCE) is aimed to investigate the potential of surface negative ion production for neutral beam injection. It has been demonstrated that high H^-/D^- current densities can be produced on a negatively biased barium converter surface in contact with a hydrogen or deuterium plasma [64, 65]. In order to obtain a high negative ion yield, the converter must face a plasma with a substantial ion density. At the same time, the neutral particle density must be kept as low as possible to avoid stripping of the negative ions from their extra electron in collisions with neutral particles. The efficiency of this process is therefore strongly coupled to the plasma characteristics. Molecular emission spectroscopy is one of the available methods to acquire information on the plasma.

This chapter is simultaneously a test-case for the theory from chapter 6 and an application of it in the characterization of the FOMSCE plasma. The experimental setup is described in section 7.2. Section 7.3 is dedicated to theoretical and experimental aspects of the interpretation of the Fulcher α spectrum. The validity of the Corona phase assumption is discussed. Procedures to determinate the rotational and vibrational temperatures are presented. Results on the characterization of the plasma are found in section 7.4.

7.2 Experimental setup

The FOMSCE experimental setup does share some main characteristics with the $H^{+/-}$ setup at Eindhoven: in both cases an expanding hydrogen arc plasma is used to generate a hydrogen plasma beam. The type of source

and plasma conditions differ significantly though. The FOMSCE surface conversion experiment is depicted in Fig. 7.1. The apparatus consists of two

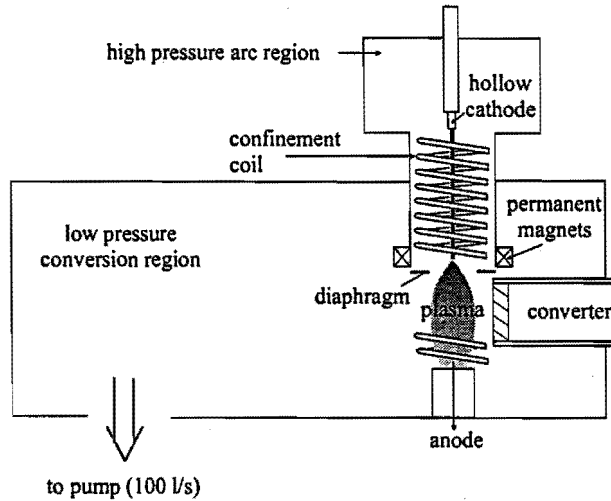


Figure 7.1. *Experimental setup of the FOM surface conversion experiment*

chambers connected through a diaphragm of 25 mm diameter. A plasma is produced in a hollow cathode, a 4 cm long tantalum cylinder with an internal diameter of 3 mm, wall thickness 0.5 mm. A magnetic coil around the hollow cathode, up to the diaphragm, confines the plasma in the upper chamber. After the diaphragm, the plasma expands into the lower chamber. The barium converter is placed halfway the lower chamber at the edge of the plasma column. Positive ions from the plasma can thus be accelerated to the surface. At the surface, conversion of incoming ions to negative ions takes place with an efficiency of $\approx 8\%$ [66]. A typical converter bias is -200 V. At this voltage the negative ions accelerated from the converter have an energy distribution around 350 eV [67].

At the bottom of the lower chamber the far anode is placed. The magnetic field configuration is designed to have a complete coverage of the converter surface with plasma. Hereto directly after the diaphragm a ring of permanent magnets is placed, producing a divergent magnetic field. At the position of the converter the plasma column reaches its maximum width. The magnetic field and thus the confinement is at minimum here. A magnetic coil around the far anode produces a magnetic field that focuses the plasma to the anode.

Only the lower chamber is pumped. This results in a pressure drop over the diaphragm; in the upper chamber the pressure is typically 10^{-2} mbar, in the lower or conversion chamber $3 \cdot 10^{-4}$ mbar. When the plasma expands into the lower chamber, the ions and electrons are confined by the magnetic

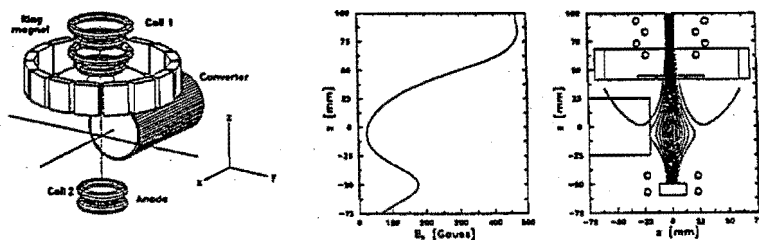


Figure 7.2. Magnetic structure configuration used in FOMSCE. The axial component of the magnetic field and traces of magnetic field lines are shown. Positions of the orifice and magnetic structure elements are indicated in magnetic field diagrams

field and the neutrals are not. In this way a plasma with a high ionization degree is created in the lower chamber. In the center of the plasma column facing the converter an ion density up to 10^{19} m^{-3} can be reached. Typical plasma conditions are listed in table 7.1.

Plasma production chamber pressure	$1 \cdot 10^{-2}$ mbar
Conversion chamber pressure	$3 \cdot 10^{-4}$ mbar
Discharge voltage	50 – 70 V (default: 55 V)
Discharge current	15 – 50 A (default: 20 A)
Degree of ionization	> 0.1
Magnetic guiding field	0.01 – 0.065 T (in converter region \ll 0.01 T)
Plasma density in converter region	$\sim 10^{19} \text{ m}^{-3}$
Pumping speed upper chamber	-
Pumping speed lower chamber	100 – 300 ls^{-1}

Table 7.1. The operating parameters of FOMSCE

The optical scanning system is depicted in figure 1. A 1:1 image of the plasma is made on the entrance slit of the monochromator by a system consisting of a lens and three mirrors. Rotation of the mirrors enables a displacement of the detection volume in horizontal and vertical direction. The plasma light is analyzed by a 1 meter McPherson visible light monochromator and an EG&G model 1422 diode array detector. This system enables simul-

taneous measurement of a wavelength interval of 120 \AA with a resolution of approximately 0.5 \AA .

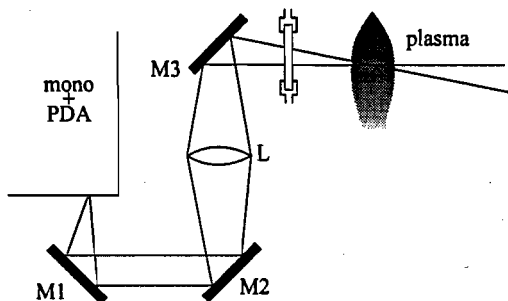


Figure 7.3. The optical scanning system

7.3 Interpretation of the molecular spectrum

The relation between the observed intensity of a spectral line and the state density of the upper level of the radiative transition was established in Eq. (6.22):

$$I_{n'n''} = \frac{16\pi^3\nu^3}{3h} A_{e'e''} q_{v'v''} N_{n'} \quad (7.1)$$

The molecular emission spectra are used to obtain vibrational and rotational distribution functions of the excited $d^3\Pi_u^-$ state. The approach introduced in chapter 6 is applied here to relate the excited state distribution functions to ground state rotational and vibrational temperatures. In this approach the excited levels are assumed to be in the Corona phase. This assumption is verified here.

7.3.1 Corona phase

If an excited level is in the Corona phase, the population of the level is dominated by electron excitation from the ground state and the depopulation is dominated by radiative decay. Collisional excitation from and deexcitation to near-lying levels must be negligible. For atomic hydrogen-like or Rydberg systems this problem is well known. Criteria for excited levels being in a Corona phase are summarized by Van der Mullen [23]. It is assumed here that the molecular system can be described in an appropriate way by this model. An effective principal quantum number p is defined:

$$p = Z\sqrt{Ry/|E_{pi}|} \quad (7.2)$$

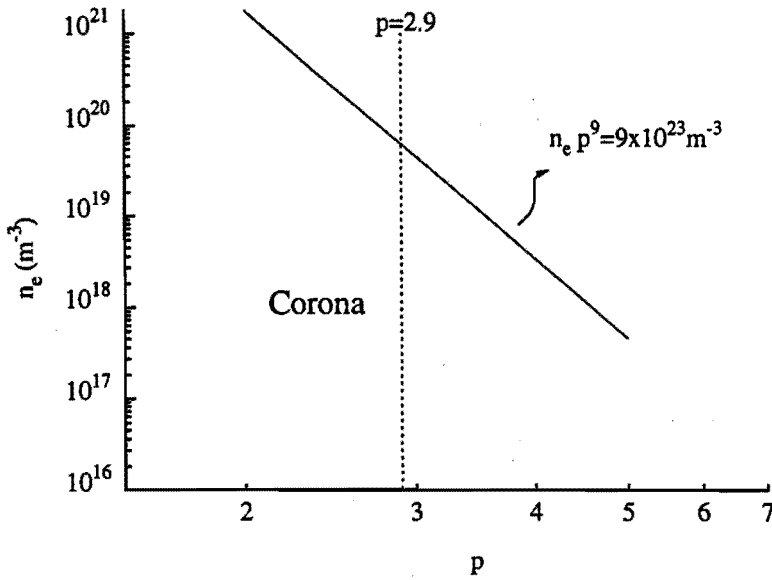


Figure 7.4. The critical level p_{cr} versus the electron density. p_{cr} is defined as the value of p at which collisional destruction occurs once in a mean radiative life time. The dashed line indicates $p = 2.9$, the effective quantum number for the Fulcher α band.

Here Z is the charge number of the core, $Ry=13.6$ eV is the Rydberg constant and E_{pi} the ionization energy from level p . For the $d^3\Pi$ level from molecular hydrogen $E_{pi}=1.6$ eV and $Z=1$. The effective quantum number consequently is 2.9. An approximation for the critical level p_{cr} , below which the Corona phase is valid, is taken from [23]:

$$n_e p_{cr}^9 = 9 \times 10^{23} \text{ m}^{-3} \tag{7.3}$$

The relation between the electron density and p_{cr} is depicted in Fig. 7.4. As the electron density in the FOMSCE plasma near the converter is not expected to exceed 10^{19} m^{-3} and the effective principal quantum number $p \approx 3$ for the $d^3\Pi$ level, the Corona phase approximation is valid here.

7.3.2 Vibration

Fig. 7.5 gives an example of a measured vibrational band. The band heads of the diagonal bands ($v' = v''$) are indicated in the figure. The intensity of a band $Q_{(v'-v'')}(K')$ head is proportional to the state density $n'(e', v', K')$, cf. Eq. (7.1). In the Corona phase the vibrational distribution function of the

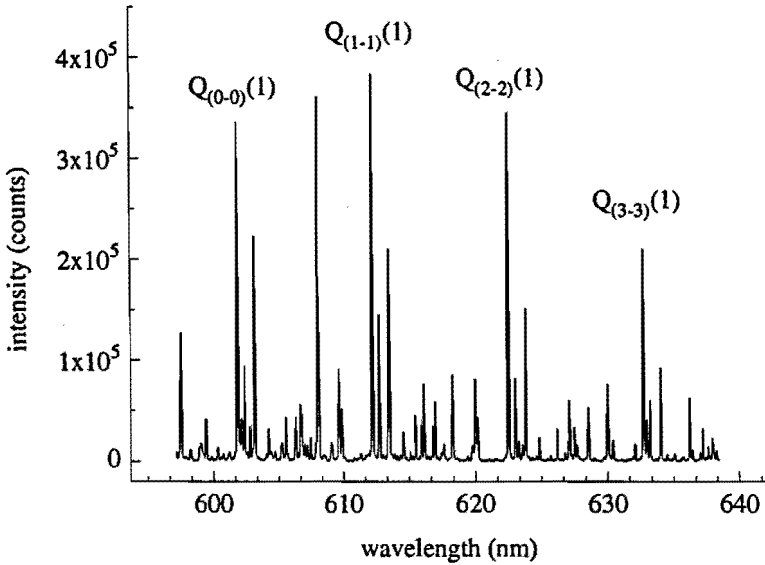


Figure 7.5. Part of the Fulcher α spectrum. The band heads of the diagonal vibrational bands $v' = v'', v = 0 - 3$ are indicated.

excited state is related to the ground state vibrational distribution by

$$f'_v(v') \propto \sum_{v^0} q_{v^0 v'} f_v(v^0) e^{-[G(v') - G(v^0)]hc/kT_e} \quad (7.4)$$

Here the vibrational energy is expressed in the form of term values $G(v)$ as defined in Eq. 6.6. This is the prevalent notation in molecular spectroscopy. In plasma physics it is more common to use E_v for vibrational energy, $E_v = G(v) \times hc$. The exponent $e^{-[G(v') - G(v^0)]hc/kT_e}$ accounts for the influence of the difference in vibrational energy between the initial and final state. A Maxwellian EEDF is assumed in this case. If the vibrational distribution of the electronic ground state is described by a thermal population, $f_v^0(v^0) \propto e^{-G(v^0)hc/kT_{vib}}$, combining Eqs. (7.1) and (7.4), the intensity distribution over the vibrational bands can be expressed in the electronic ground state vibrational temperature:

$$I_{v'v''} \propto \nu^3 \sum_{v^0} q_{v^0 v'} e^{-G^0(v^0)hc/kT_{vib}} e^{-[G(v') - G(v^0)]/kT_e} q_{v'v''} \quad (7.5)$$

The rotational distribution function is expected to be independent of the vibrational state (cf. section 6.4). The vibrational distribution function can therefore be determined from any set $Q_{(v'-v'')}(K')$, K' constant. Here only the first three diagonal bands ($v' = v'', v' = 0..3$) are used. The curves in Fig. 7.6 show the calculated intensity of $Q_{v'-v''}(1)$ lines as a function of

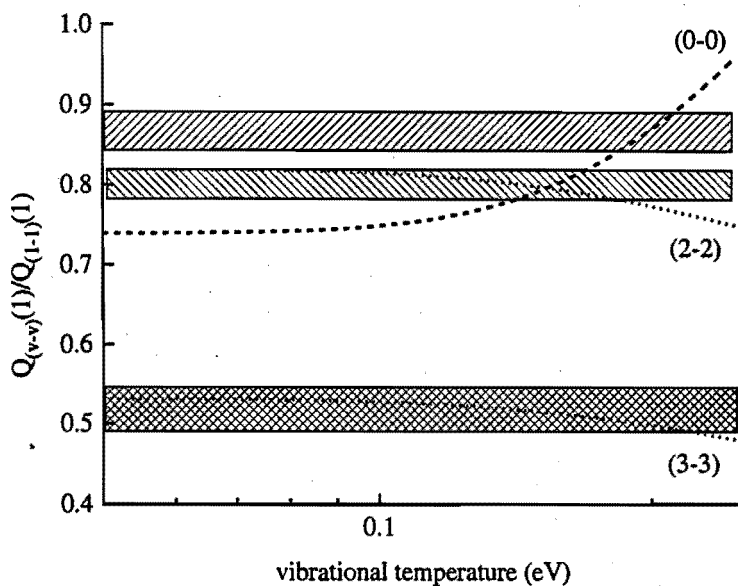


Figure 7.6. *Calculated intensity ratios of diagonal band heads versus ground state vibrational temperature T_{vib} , and measured intensity ratios. An electron temperature of 3 eV was assumed for the calculated curves.*

the ground state vibrational temperature. The intensities are normalized on the $Q_{(1-1)}(1)$ line intensity. Apparently only the ratio of the (0-0) to the (1-1) band is sensitive for the vibrational temperature in this range. The horizontal lines show measured line intensities, also normalized on the $Q_{(1-1)}(1)$ line. The bars indicate the experimental inaccuracy. The ratio $Q_{(0-0)}(1) / Q_{(1-1)}(1)$ corresponds to a vibrational temperature of 0.2 eV. As will be seen in the following, this is much higher than the rotational temperature in the plasma. This is a consequence of the nature of vibration and rotation. To change the vibrational state of a molecule with an incoming electron, it is not necessary to change the position or movement of the nuclei during the collision. In the Franck-Condon approximation a vibrational transition takes place as a result of a change in the orbitals of the electrons. The interaction between a bound electron in the molecule and an incoming electron can be strong. For a rotational transition, the movement of the nuclei in the molecule must be changed. The large mass ratio $m_{H_2} : m_e$ makes this interaction less effective.

7.3.3 Rotation

Fig. 7.7 gives an example of a measured rotational (0-0) band. In the determination of the electronic ground state rotational temperature, the formalism

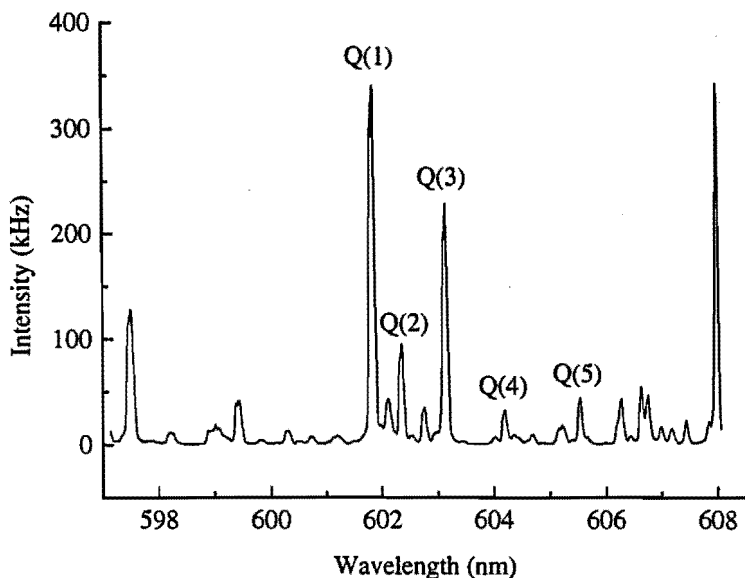


Figure 7.7. The (0-0) rotational band of the Fulcher α band. The intensity alternation for odd and even rotational quantum numbers is due to nuclear spin degeneracy.

from section 6.6 is followed. Using Eqs. (6.33), (6.39), and (6.40) the relation between the observed intensity distribution over a rotational band and the electronic ground state rotational temperature is:

$$I_{K^0 K'} \propto \nu^3 f'_{rot}(K') \propto \nu^3 g_I \sum_{K^0} R_{K^0 K'} (2K^0 + 1) e^{-F(K^0)hc/kT_{rot}} \quad (7.6)$$

The nuclear spin degeneracy g_I is 3 for odd and 1 for even rotational levels; this causes the intensity alternation in the rotational spectrum (cf. Fig. 7.7).

The most convenient way to determine the ground state rotational temperature is to determine an effective rotational temperature T'_{rot} for the $d^3\Pi^-$ state and relate this to the ground state rotational temperature by Fig. 6.10. The effective temperature T'_{rot} is defined as the best straight line fit through the measured $f'_{rot}(K')$ in a Boltzmann plot, $\ln[f'_{rot}(K')/(2K' + 1)(g_I)]$ versus the rotational energy. Fig. 7.8 shows the Boltzmann plots of a (0-0), (1-1) and (2-2) rotational band. The effective rotational temperatures T'_{rot} are indicated in the figure. There is some difference between the rotational temperatures determined from the (0-0), (1-1) and (2-2) bands. Although the differences are small ($\pm 5\%$), they appeared to be systematic in all measured spectra. As the molecular spectrum of hydrogen has numerous spectral lines over the entire visible range, the possibility of overlapping lines must be considered. Table 7.2 lists lines that are within 0.5 Å (the resolution of the

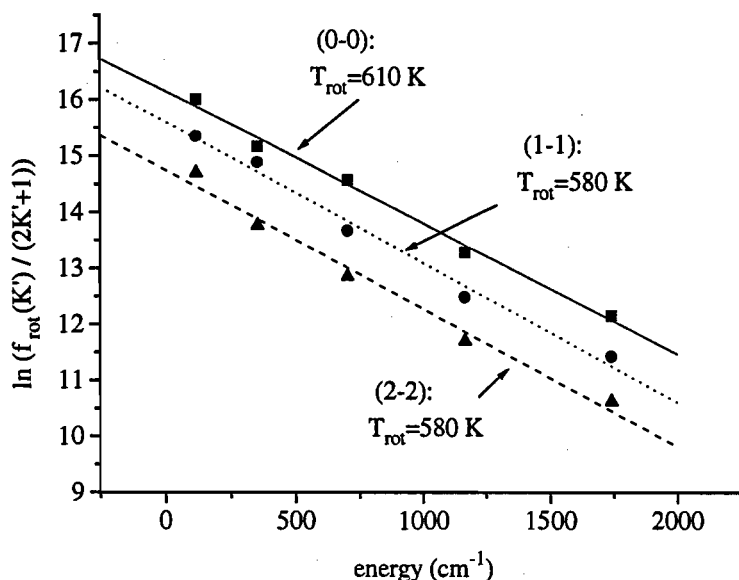


Figure 7.8. Boltzmann plot of the first five lines of the Q-branches in the (0-0), (1-1), and (2-2) band.

optical system is 0.5 Å) from any of the Fulcher α rotational lines used in Fig. 7.8. Only 'disturbing' lines that have a line strength of 5% or more of the 'disturbed' line are included. Data are taken from 'The hydrogen wavelength tables' from Dieke [68]. From the lines that may be disturbed by overlap ac-

"disturbed" line	"disturbing" lines			
	upper level	lower level	branche	wavelength
$Q_{(0-0)}(3)$ 6031.909 Å	$i^3\Pi_g(v' = 2)$	$c^3\Pi_u(v'' = 2)$	P(2)	6031.465 Å
$Q_{(1-1)}(2)$ 6127.246 Å	$h^3\Sigma_g^+(v' = 0)$	$c^3\Pi_u(v'' = 0)$	P(4)	6127.344 Å
$Q_{(1-1)}(5)$ 6159.565 Å	$d^3\Pi_u(v' = 0)$	$a^3\Sigma_g^+(v'' = 0)$	Q(10)	6159.269 Å
$Q_{(2-2)}(1)$ 6224.815 Å	$I^1\Pi_g(v' = 3)$	$B^1\Sigma_u^+(v'' = 10)$	Q(3)	6225.040 Å
	$g^3\Sigma_g^+(v' = 2)$	$c^3\Pi_u(v'' = 2)$	P(3)	6225.312 Å

Table 7.2. Lines coinciding with lines of the Fulcher α band within 0.5 Å (after [68]). Only disturbing lines with a tabulated intensity >5% relative to the disturbed line are included.

According to table 7.2 for the $Q_{(1-1)}(5)$ is not expected to be disturbed in the FOMSCE experiments. It overlaps with a $Q(10)$ line from the Fulcher α band. The rotational temperatures determined in the experiments are too low to populate such high rotational levels significantly. Furthermore above rotational quantum number $K=5$ the intensity of rotational lines generally was too low to distinguish them from the background. Remain the $Q_{(0-0)}(3)$, the $Q_{(1-1)}(2)$ and the $Q_{(2-2)}(1)$ lines as possibly overlapped. An interesting

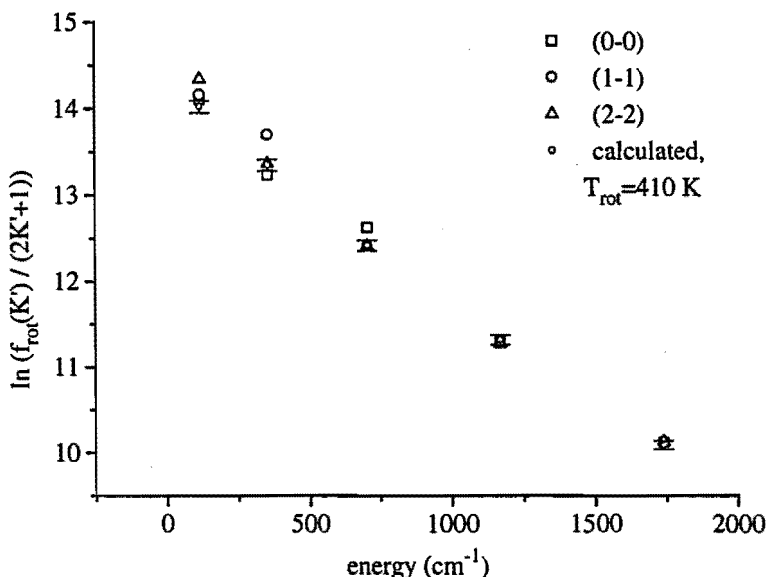


Figure 7.9. Boltzmann plot of the first five lines of the Q -branches in the $(0-0)$, $(1-1)$, and $(2-2)$ band and of the calculated distribution in the excited state.

result shows Fig. 7.9. In this figure a calculated and measured rotational distribution functions determined from the $(0-0)$, $(1-1)$ and $(2-2)$ vibrational bands are plotted in a Boltzmann plot. The calculated excited state population is derived from a ground state thermal distribution and matrix $R_{KK'}$ according to Eq. (7.6). The rotational temperature for the electronic ground state is optimized to match the observed rotational distribution functions of the excited state. Indeed the points in the Boltzmann plot related to the $Q_{(0-0)}(3)$, the $Q_{(1-1)}(2)$ and the $Q_{(2-2)}(1)$ line are lying too high. In further determinations of rotational temperatures these lines were ignored. A procedure is proposed here to determine the electronic ground state rotational temperature:

1. A rotational band is measured. The $(1-1)$ band is preferred as this is the most intense band. The $Q(2)$ line overlaps with another molecular line and is therefore omitted.

2. An effective rotational temperature T'_{rot} is determined from a Boltzmann plot from this band.
3. This effective rotational temperature is related to the electronic ground state rotational temperature. Hereto the effective rotational temperature as a function of the electronic ground state rotational temperature must be calculated for the relevant temperature range and selection of rotational lines.

In the following all rotational temperatures are determined according to this procedure.

7.4 Plasma characterization

A spatial temperature profile was measured from the region facing the converter for default plasma conditions. Fig. 7.10 shows the intensity distribu-

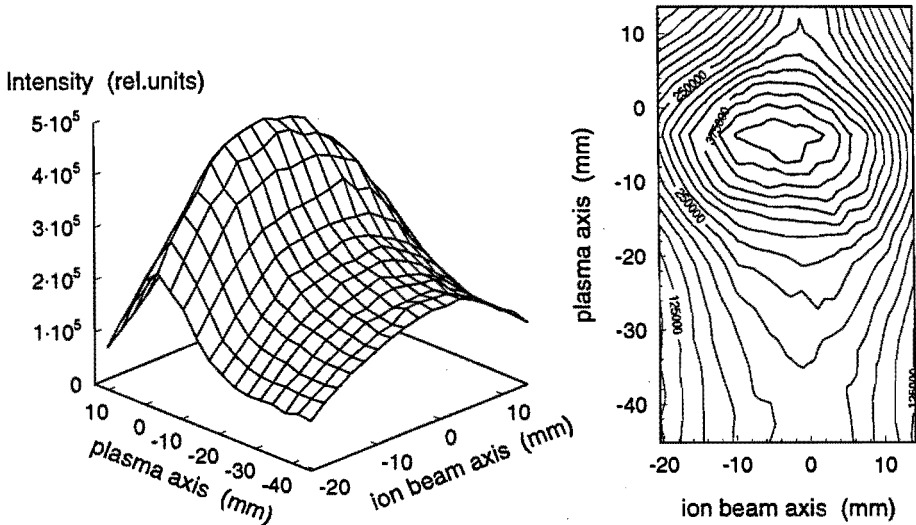


Figure 7.10. Spatially resolved measurement of the intensity of the $Q_{(0-0)}(1)$ line. The diaphragm separating the upper and lower chamber is at position $(0,40)$. The converter surface ranges from $(20,-15)$ to $(20,15)$. The far anode is at position $(0,-50)$.

tion of the $Q_{(0-0)}(1)$ line over this region. The spatial rotational temperature profile, as determined from the vibrational (1-1) band, is depicted in Fig. 7.11. The temperature decreases from the diaphragm to the far anode, along the flow direction of the plasma expanding through the diaphragm from the

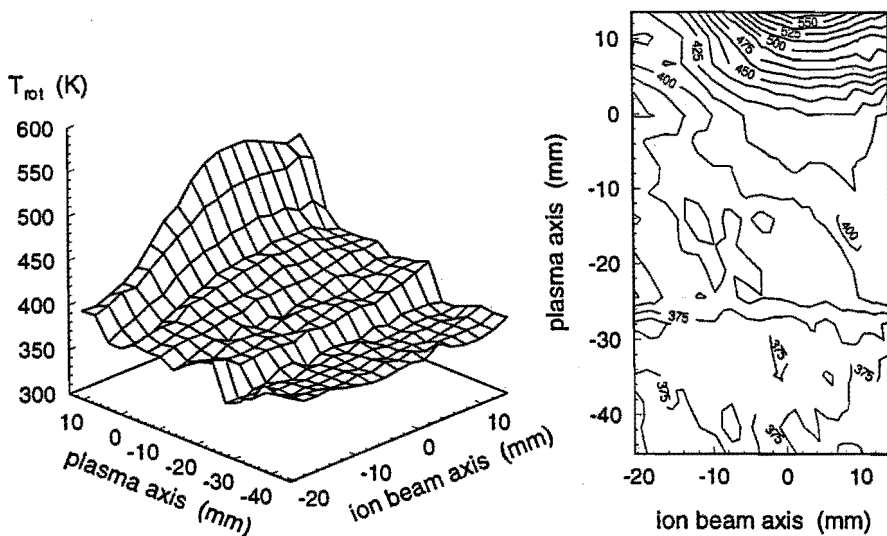


Figure 7.11. Spatially resolved rotational temperature determined from the $Q_{(0-0)}$ branch.

upper plasma chamber (cf. Fig. 7.1). At position (0,0), facing the converter, the response of the rotational temperature to discharge parameters is measured.

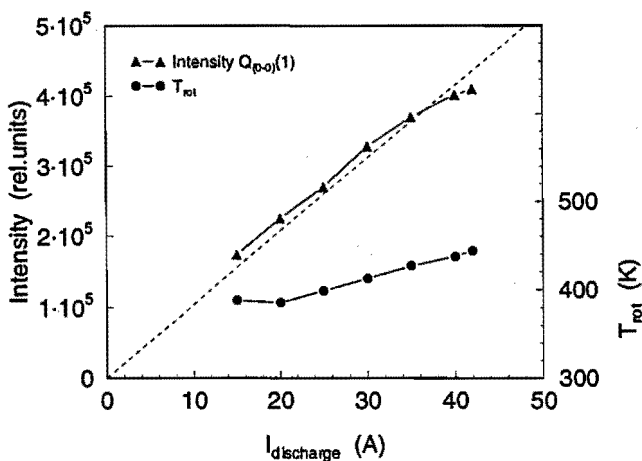


Figure 7.12. Effect of the discharge current on the rotational temperature and the intensity of the $Q_{(0-0)}(1)$ line.

The relation between the discharge current and the rotational temperature is given in Fig. 7.12. The coupling between the electron temperature and

the gas temperature is weak. The temperature of the gas is proportional to the discharge current. At a high electron temperature and ionization degree, as in the FOMSCE plasma, the rotational heating of the gas is dominated by electron-molecule collisions. The heat transfer from electrons to molecules is $\propto n_e n_{H_2} k_{e-H_2}^{rot}$. The rotational excitation rate is hardly temperature dependent in the temperature range 2-5 eV [69]. The electron temperature is furthermore expected to be only weakly dependent on the discharge current in this type of discharge (cf. [70]). Under constant plasma dimensions the electron density is linear with the discharge current. The observed increase in rotational temperature is therefore attributed to the increase in electron density. The intensity of the $Q_{(0-0)}(1)$ line versus discharge current is plotted in the same figure. Here also a linear relation is observed, between the observed intensity and the discharge current. In a Corona phase radiative system the intensity of a spectral line is linear with the electron density. This is in agreement with the picture of constant electron temperature and linearly increasing electron density.

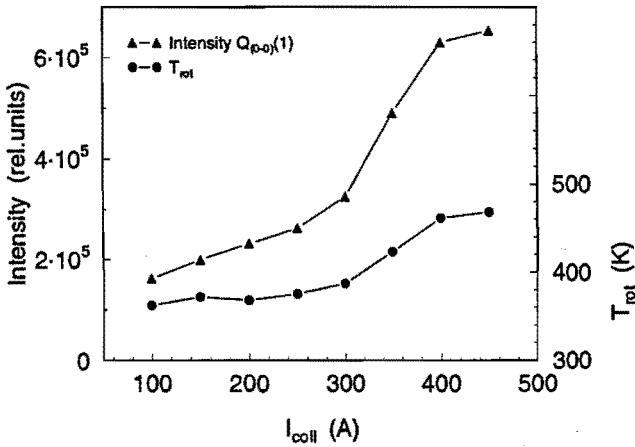


Figure 7.13. Effect of the coil current on the rotational temperature and the intensity of the $Q_{(0-0)}(1)$ line. The magnetic field is proportional to the coil current. It is not homogeneous over the plasma, cf. Fig. 7.2. In the upper chamber the magnetic field strength as a function of coil current is $\approx 1.2 \cdot 10^{-4} T/A$.

The magnetic field in the upper plasma chamber is proportional to the coil current applied. The influence of this magnetic field on the measured rotational temperature is found in Fig. 7.13. The curve presenting the rotational temperature versus coil current shows a sudden change in slope around 300 A coil current, corresponding to a magnetic field of approximately 30 mT. Below this point, the rotational temperature is only weakly dependent on the magnetic field in the upper chamber. Above this current the rotational temperature starts to increase. A possible explanation is found in a mode

transition of the plasma in and near the hollow cathode. Vogels [71] showed that in a hollow cathode discharge a mode transition can be found if the magnetic field is increased. The crucial parameter in this transition is the ion Hall parameter, the ratio between the ion-ion free path length λ_{ii} and the ion cyclotron radius ρ_i . An expression for the ion Hall parameter can be found in e.g. [72].

Vogels [71] showed that a phase transition occurs at a Hall parameter ≈ 5 . This was verified experimentally in his work on a hollow cathode arc discharge on argon, at a critical magnetic field of 0.06 T. The discharge current was 50 A in this experiment. The result was not dependent on the pressure in the range 3 to $30 \cdot 10^{-3}$ mbar (FOMSCE plasma: $20 \cdot 10^{-3}$ mbar in upper chamber). As the ion mass in a hydrogen plasma is 13 (H_3^+) to 40 (H^+) times less than in an argon plasma, in a hydrogen plasma the turning point might occur at a 4 to 6 times lower field strength. The ion density and ion temperature can also differ. Considering all this, the turn in the rotational temperature at 0.03 T can be explained by a transition to a turbulent regime.

The intensity of the $Q_{(0-0)}(1)$ line in Fig. 7.13 shows a similar behaviour as the rotational temperature.

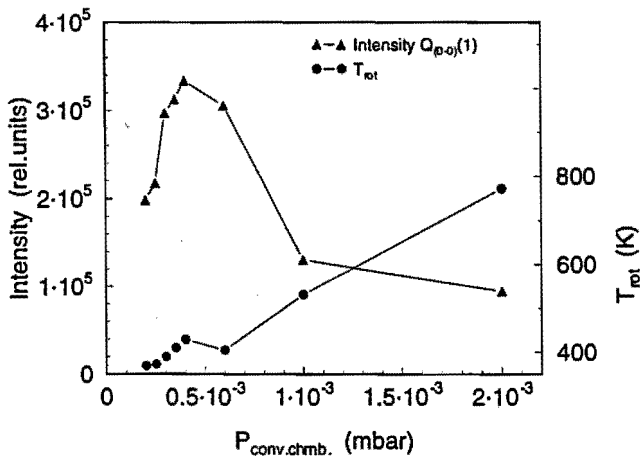


Figure 7.14. Effect of the pressure in the conversion chamber on the rotational temperature and the intensity of the $Q_{(0-0)}(1)$ line.

The rotational temperature increases linearly with the reactor pressure, Fig. 7.14. The intensity of the $Q_{(0-0)}(1)$ line shows two branches. Below $5 \cdot 10^{-4}$ mbar the intensity increases roughly linear with pressure. Above this pressure a sudden decrease is observed. The increase can be explained by the increase in molecular density. If the electron density and temperature do not change too much, the line intensity must be proportional to the molecular density. The decrease coincides with another phenomenon: the plasma switches mode near $5 \cdot 10^{-4}$ mbar. Below this pressure there is a clear plasma

column, focused on the far anode, above this pressure the plasma is 'blown up' and goes to the walls of the reactor instead of to the far anode.

7.5 Discussion

Rotational temperatures have been determined for the FOMSCE hydrogen plasma from the Fulcher α emission spectrum. Hereto the method described in chapter 6 was used, that accounts for a change in rotational state in the electronic excitation of the molecule. In an earlier publication, this rotational excitation was not accounted for [73]. The rotational temperatures given there, are systematically too high. The method from chapter 6 was adequate to describe the observed rotational spectrum assuming an electronic ground state rotational temperature.

The spatial temperature profile as depicted in Fig. 7.10 shows that the rotational temperature decreases downstream of the diaphragm. Here a tentative explanation is given for this observation. It will be argued that rotational relaxation can not take place in the plasma that expands from the diaphragm. For an explanation first the electron and neutral density must be estimated.

The neutral density in the plasma is estimated from the background pressure. With $p = nkT_g$ and an estimated gas temperature $T_g = 400$ K we find $n_0 = 6 \cdot 10^{18} \text{ m}^{-3}$. A further source of neutral particles is the converter. The vast majority of ions that hits the barium surface returns as atoms or, after wall association, molecules. An ion current of ~ 1 A yields a neutral particle flux of $3 - 6 \cdot 10^{18} \text{ s}^{-1}$. If it is assumed that these particles have a thermal velocity (2000 m/s at 400 K), this gives rise to an additional neutral density of $\sim 4 \cdot 10^{18} \text{ m}^{-3}$. Finally the gas flow to the plasma increases the neutral density in the conversion chamber. At standard discharge conditions this amounts 10^{18} m^{-3} .

The electron density can be estimated near the converter from the ion saturation current to the converter. With an electron temperature of 3 eV and a converter current of 1 A, this yields an electron density around 10^{18} m^{-3} . If the intensity of the emitted spectrum is used as a measure for n_e , the electron density is about two times higher near the plasma axis and increases further towards the diaphragm.

With these estimates for n_0 and n_e mean free path lengths for collisions that influence the rotation of molecules can be considered. For neutral-neutral collisions, an upper limit estimate for the cross section is the gas kinetical cross section, $\sim 10^{-19} \text{ m}^2$. The mean free path length for this type of interaction, $1 / \langle n_0 \sigma_0 \rangle$, is around 1 m. Close to the diaphragm the neutral density may be higher, but still the mean free path will be at a decimeter scale. Considering that the plasma radius is only a few centime-

ters, neutral-neutral interaction can be neglected. A consequence of this is that, as far as neutral particles are concerned, the background gas is transparent for the plasma beam, and the latter can be superimposed on the cold background. Neutral-ion and neutral-electron collisions both have the longer range induced dipole interaction. It appears that the electron-molecule collisions have a larger rate coefficient than the ion-molecule collisions for rotational (de-)excitation [69, 74]. The cross section for a rotational excitation ($\Delta K = 2$, cf. chapter 6) is $\sim 10^{-20} \text{ m}^2$. The mean free path of a molecule through the plasma is $v_{H_2} / \langle n_e \sigma v_e \rangle$. For $T_e = 3 \text{ eV}$ and $n_e = 10^{18} \text{ m}^{-3}$ this is 20 cm, for $n_e = 10^{19} \text{ m}^{-3}$ this is 2 cm. Rotational excitation through electron collisions can be important in the FOMSCE plasma, but depends very critical on the electron density. This can explain why in Fig. 7.10 closer to the diaphragm the rotational temperature is higher: here also the electron density is higher.

A further observation is made concerning the plasma flow. The gas is expected to be rotationally hot near the hollow cathode in the upper chamber, as it comes from the high density hollow cathode region. As argued, rotational relaxation is not possible in the plasma beam. Still the experimentally determined rotational temperatures in the lower, conversion chamber near the converter are rather low. Apparently the bulk of the molecules in the studied plasma region originates from the background gas. This is in full agreement with results at the expanding cascaded arc plasma setup, cf. chapter 3; there even at a two to three orders of magnitude higher particle density recirculation of background molecular gas mixing into the plasma beam dominates the molecule density in the plasma.

In view of an optimized negative ion yield from a surface conversion plasma, production and destruction of negative ions must be considered. The production depends mainly on the ion density near the barium converter. Destruction takes place when the negative ions cross the plasma in the direction of an extraction opening facing the converter. Destruction occurs through collisions of negative ions with electrons, positive ions, or neutral particles. For a typical negative ion energy of 350 eV (cf. [65]), the reaction with the largest cross section is mutual annihilation, $H^+ + H^- \rightarrow H^* + H$. This reaction has a cross section of $\sim 2 \cdot 10^{-18} \text{ m}^2$. Mutual annihilation is not problematic if the ion density is below 10^{19} m^{-3} . If the estimate of the electron density is accurate, this allows for a stronger plasma source for the converter. Detachment in collisions with H or H_2 has a cross section of $\sim 5 \cdot 10^{-20} \text{ m}^2$. As is argued above, the neutral particle density in the plasma is mainly determined by the background pressure. At the default condition the background pressure is $3 \cdot 10^{-4} \text{ mbar}$. This corresponds to a neutral particle density of $\sim 10^{19} \text{ m}^{-3}$ and a mean free path for detachment of the negative ions of 2 m. Detachment on neutral particles can therefore be neglected in the FOMSCE plasma setup.

Treatment of iron archeological artifacts in a hydrogen plasma beam

8.1 Introduction

In the conservation of iron archeological artifacts two major problems are encountered. The first problem concerns the encrustation, a hard agglomerate layer that covers the artifact. It consists of soil and oxides from migrated ions from the metal of the artifact. The second problem is post-corrosion: whereas before excavation the corrosion process has been very slow, the abundance of oxygen in musea or storage rooms may lead to a total destruction of the excavated object within a timescale as fast as months. A crucial element in the corrosion process is usually the presence of chlorides in the artifacts, leading to so-called chloride infections [75]. The nature of these chlorine infections will be explained in section 8.2.

Over the years, several methods to passivate or eliminate these infections have been examined, ranging from storage in alkaline environments [76], to hot gas treatments [77, 78] and electrolysis [79]. Currently the most favoured technique is the alkalide sulphite treatment: the artifacts are stored in an alkalide sulphite solution at 50 °C for a period of three months up to one year [80, 81]. Although the results of this method on chloride removal are generally reasonable, it has some serious disadvantages. The conservator is left with large quantities of hazardous chemicals and the treatment time is very long. The latter is particularly important; over the last decades the number of emergency excavations has increased strongly. Findings are often revealed at building sites and are only accessible for a short period of time. Moreover, artifacts previously safe in the soil are treated by acid rain and other factors that deteriorate the environment. Therefore alternative treatment strategies are pursued.

A promising line of research is hydrogen plasma treatment of the artifacts. This research has been initialized by Daniels et al. [82, 83], who used a

hydrogen glow discharge plasma with a low gas temperature (100 °C) to clean silver photographic plates. Picking up the idea of plasma treatment, Vepřek started treating iron artifacts in an RF glow discharge (27 Mhz, 4 kW) in 1985. His work has led to a commercial machine; over 20,000 objects have been treated since using this type of machine. The plasma treatment using the Vepřek technique has proven to greatly facilitate the removal of the encrustation. It is also effective in the removal of chlorides from the artifact at moderate (~ 400 °C) sample temperatures. This is attributed to the presence of atomic hydrogen in these plasmas [84, 85].

The expanding cascaded arc plasma is known to deliver a large flow of atomic hydrogen at a low plasma temperature [86]. Therefore at the Eindhoven University of Technology a survey experiment was done in 1989 on a small collection of artifacts. Despite the very short treatment time (20 minutes compared to 2 hours pretreatment and 18-20 hours posttreatment in the Vepřek experiments) and the provisory character of the experiments, the samples turned out to hold well [87, 88]. This was the reason to start a plasma treatment programme, results of which are presented in this paper.

8.2 Corrosion

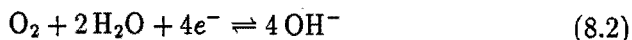
In nature non-noble metals like iron only occur as minerals. Metallic iron therefore is in a non-equilibrium state and corrosion is the process that brings the iron in equilibrium with its surroundings [89, 90]. The type of mineral that is formed and the speed at which this happens, is determined by the environment. In the corrosion of iron the abundance of water, oxygen and chlorine ions are of crucial influence. Two environments are distinguished. Before excavation, artifacts are in an environment where oxygen is sparse and water is abundant. After excavation, oxygen is abundant. A water layer is present at the artifacts at higher relative humidities (RH) of the surrounding air, but at low RH dehydration of the corrosion layer may occur. In the following a general description of the corrosion process is given. Attention is given to the specific aspects of chlorides before and after excavation.

When a metal is exposed to an aqueous environment, metallic ions can go into solution:

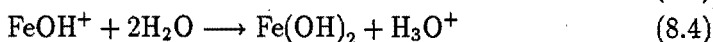
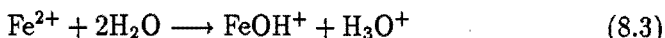


For a non-noble metal in water, there is always a surplus of electrons in the metal. This gives rise to a potential difference between the (positive) solution and the (negative) metal, the Nernst or equilibrium potential. At the same time the metal can serve as an active medium on which a redox reaction can

take place:



This redox system has a different equilibrium potential. This will lead to a system that is not in equilibrium but has a continuous flow of metal ions going into solution compensated by a continuous reduction of oxygen. In practical situations the anodic reaction (8.1) and cathodic reaction (8.2) are spatially separated. This is a consequence of irregularities in the metal. At some spots on the artifact pits may form, either due to metallurgic or structural inhomogenities or due to inhomogenities in the solution. Diffusion of oxygen into these pits will be more difficult than at the bulk surface of the artifact. The reduction of oxygen therefore occurs preferably at the surface and will be balanced by the solution of metallic ions in the anodic regions. As the pit area is much smaller than the surface area, there will be a high local rate of metal dissolution in the pits. Furthermore, the environment in the pits will become slightly acid by reaction (8.3):



The corrosion process is an electrochemical process driven by potential differences between the metal and the surrounding solution. The steps involved in the corrosion are:

1. At the anode side the potential of the aqueous solution is lower than on the metal. Here iron ions go into solution.
2. At the cathode side the potential of the aqueous solution is higher than on the metal. Here OH^- ions are produced according to Eq. (8.2).
3. Between the cathode and anode region an ionic current is driven, that balances the electron current through the metal.

Rate limiting factors for the corrosion process depend on the environment. Before excavation the availability of oxygen is usually the limiting factor (if this is not so, there is not any artifact left whatsoever). Especially when a corrosion layer is already formed on the metal, diffusion of oxygen to the metal will become very slow and the corrosion rate may become very low. This can stabilize artifacts for many centuries. The ionic current is carried by the most mobile ions. As chloride ions are mobile and usually more abundant than OH^- these will take care of the ionic current instead of Fe^{2+} or OH^- . As a consequence a concentration of chloride ions is built up at the anode region. This explains the high chloride concentrations found on artifacts.

The corrosion process before excavation leads to the formation of two types of corrosion, Fig. 8.2. Directly on the metallic core a layer of mainly

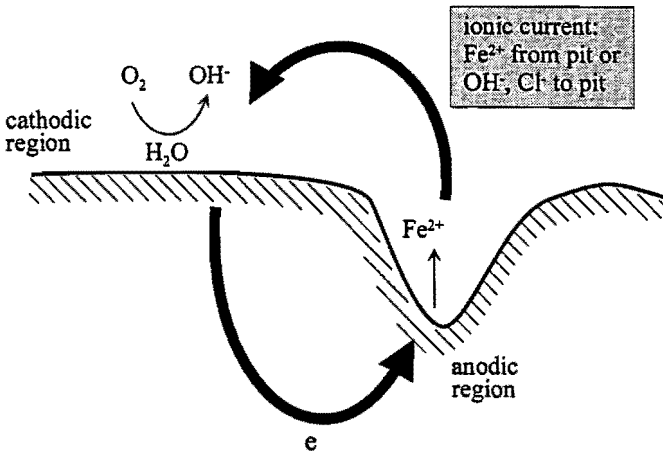


Figure 8.1. *The corrosion process. In a continuous corrosion process the electron current through the metal is balanced by the ionic current through the aqueous solution.*

Fe_3O_4 or magnetite is formed. This corrosion layer contains the original shape of the artifact and is to be preserved. A second type of corrosion forms the incrustation. The incrustation is formed by migrated iron ions from the pit regions that form an agglomerate with the surrounding soil. The dominant corrosion type is Fe_2O_3 . The incrustation must be removed entirely.

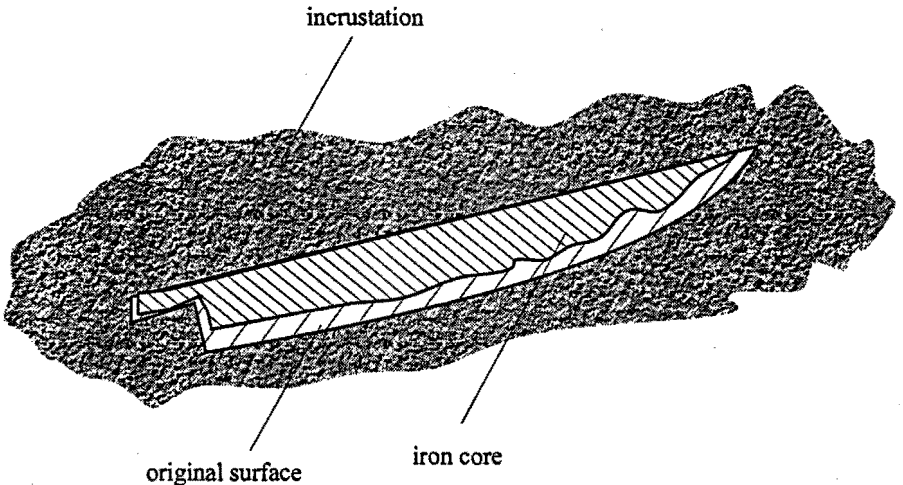
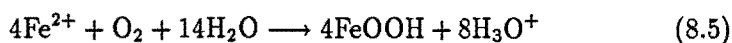


Figure 8.2. *The two types of corrosion on artifacts. Directly on the metallic core a magnetite layer is formed, containing the shape of the artifact. Around this a thick, irregularly shaped agglomerate layer of oxides and soil is found.*

The corrosion process changes after excavation. Oxygen now is abundant, and other factors can become rate limiting. At a very dry atmosphere the cathodic reaction can not take place due to the absence of water and ionic conduction. For a clean iron object, without any chloride or other contaminations, this is the case if the relative humidity (RH) of the surrounding air is below 60 percent. However, if chlorides are abundant in the corrosion layer, this changes dramatically. Iron chloride is very hygroscopic and will form a water layer at a RH of 20%. As the RH in typical musea and storage rooms is typically 30-40% chlorides have a dramatic effect on the formation of an aqueous layer. Another effect that occurs after excavation is that the ion concentration in the aqueous solution on the artifact increases strongly due to evaporation of water. Especially in pit regions this has a strong effect: abundance of Cl^- leads to a very acid solution with a pH often below 1. This enhances the dissolution of iron greatly. Another possible rate limiter, the ionic conduction, is also enhanced by the presence of mobile chloride ions. If the artifact is exposed to air, even in pit regions there is sufficient oxygen. Oxidation of Fe^{2+} in the pits supports the decrease in pH. The reaction can be summarized by

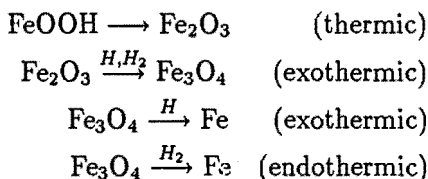


Under presence of chlorides FeOOH will form a lattice with Cl built in. If the concentration of chlorides is larger than 1 mol/l, akageneite ($\text{FeOOH} \cdot \text{Cl}_{0.02-0.05}$) is formed. Akageneite is generally considered to be the most problematic chemical form in which Cl is bound [75, 91, 92]. This mineral forms a water layer at $\text{RH} > 18\%$. It is furthermore more voluminous than iron oxides; when it is formed in pits, mechanical stress builds up that finally can lead to cracks in the artifact. Chlorides can be fixed into the akageneite lattice. This passivates chloride infection. However, this effect is temporary. Akageneite is instable, decay times are observed ranging from 8 months to 25 years [75]. When it decays chloride ions are released. If the relative humidity is fluctuating, the decay can even go faster. On each dehydration the lattice structure is changed and chlorides are released. After hydration they will again catalyze the corrosion process until they are again built in into akageneite. Therefore, in order to conserve chlorine-infested iron artifacts the decomposition of akageneite and the removal of chlorine are essential.

In summary the above chloride infections have a detrimental effect on artifacts. Therefore, in the conservation of artifacts a reduction of the chlorine content is wanted. This requires decomposition of the akageneite present in the corrosion layer. A plasma treatment, using the abundance of atomic hydrogen, could be an efficient way to achieve this reduction.

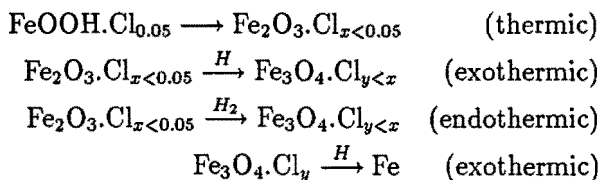
8.3 Reduction of oxides and chlorides

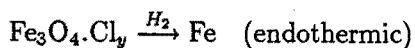
Two objectives can be met by the reduction of oxides. The first objective is to facilitate the removal of the incrustation. For this purpose it is sufficient to reduce the Fe_2O_3 in the incrustation to Fe_3O_4 . Due to this reduction the corrosion layer will shrink, as the Fe_3O_4 lattice is smaller than the Fe_2O_3 lattice. This will induce mechanical stress that leads to separation of the incrustation from the underlying corrosion layer, that already consisted of Fe_3O_4 . The second objective can be reduction of the Fe_3O_4 to metallic iron. Although from the conservators point of view it is not desired to obtain a full reduction of all oxides, it will be argued later that reduction to metallic iron of a thin top layer is convenient in view of the removal of chlorine and also facilitates post-treatment of the artifact. In the reduction of oxides therefore both the reduction of Fe_2O_3 and Fe_3O_4 must be considered. The relevant processes are shortly discussed here. For the reduction of FeOOH the main reactions are



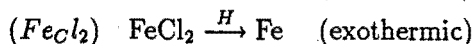
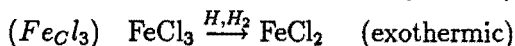
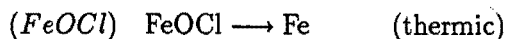
Distinction is made here between endo- and exothermic reactions. Evidently in the presence of molecular hydrogen the reduction of Fe_2O_3 to Fe_3O_4 is exothermic. For the reduction of Fe_3O_4 to metallic iron the reaction with molecular hydrogen is endothermic; this reaction can only be reducing if the hydrogen partial pressure is much higher than the water vapour partial pressure. High temperatures ($\gg 400^\circ\text{C}$) are furthermore required to make it fast. Atomic hydrogen is much more favourable for the reduction of oxides; the reactions will always be exothermic.

Reduction of chlorine containing compounds goes similar as the oxygen reduction. A central role in the reduction scheme is reserved for (β -) $\text{FeOOH}.\text{Cl}_{0.02-0.05}$ or akageneite. As argued before, this is a hydrated ferrous oxide lattice that hosts chlorides, and is the most problematic occurrence of chlorides. Therefore the reactions are organized around the decomposition of akageneite,





with possible intermediate compounds



As there is no definite answer on which structures are obtained after dehydration of akageneite, various options are given. The reduction of FeCl_3 to FeCl_2 is exothermic both for atomic and molecular hydrogen. The reduction of FeCl_2 is strongly endothermic with molecular hydrogen and therefore requires atomic hydrogen. In addition to reducing reactions involving hydrogen, also thermal decomposition of chlorides is possible. FeOCl , a possible intermediate product in the decay of akageneite, decomposes thermally to FeCl_3 . At temperatures above 350°C FeCl_3 evaporates. The reduction of chlorine from a corrosion layer can therefore occur both thermally as by chemical processes.

8.4 Diagnostics

The effect of the plasma treatment has been investigated with HEIS, PIXE and XPS. These techniques are summarized below.

High Energy Ion Scattering

In HEIS (High Energy Ion Scattering) a monoenergetic ion beam is scattered backward on a target sample. The scattered ions are detected under a fixed angle with the incoming beam. If an ion hits a target nucleus at the surface of the sample, the energy loss of the ion will be determined by the mass ratio of the incoming and target particle. In an energy loss spectrum each peak is related to a certain element. If deeper lying target nuclei are hit, the incoming ion will undergo a continuous stopping during the incoming and outgoing trajectory. This energy loss will broaden the peak in the energy loss spectrum to the larger energy loss side, resulting in a step rather than a peak signal. The amount of energy lost due to this stopping depends on the composition of the top layer of the sample and on the travelled distance. The energy loss spectrum thus can yield depth information on the composition of the target. HEIS is used here at beam energies that give resonant scattering. This improves the sensitivity for certain elements. For example using 8.8 MeV α -particles the sensitivity for oxygen is increased by a factor of 30

compared to RBS. A complication is that the cross sections for scattering have a complicated energy dependence. This is overcome by the use of a calibration sample. In the present work the ratio of cross sections for oxygen and iron was calibrated on a Fe_3O_4 single crystal. HEIS has been used to determine the relative densities of iron and oxygen. The depth range of the technique is for the examined samples approximately $10 \mu\text{m}$.

Proton Induced X-ray Emission

In the case of PIXE (Proton Induced X-ray Emission) the target is exposed to a 3 MeV proton beam. The beam current is of the order of 100 pA over an area of 4 mm diameter. The proton beam can remove inner shell electrons from target atoms. If an electron from a K or L inner shell is removed, the vacancy can be filled by an electron decaying from a higher shell. The released energy can be emitted as an X-ray photon (alternatively an Auger-electron can be emitted). This mechanism results in an X-ray emission spectrum. If the ionization cross sections and spectroscopic data are known, particle densities can be determined from the spectrum. The interpretation of the spectra was done using software developed by the group Nuclear Analysis Techniques of the Eindhoven University of Technology.

PIXE yields results averaged over the top $10 \mu\text{m}$ of the samples. The method is not sensitive to light elements ($Z \leq 11$), as in that case the Auger process is strongly favoured compared to the fluorescence. In this work it has been used to determine the top layer composition, with focus on chlorine. For chlorine, PIXE has a sensitivity in the order of parts per million.

X-ray Photo-electron Spectroscopy

XPS (X-ray Photo-electron Spectroscopy) uses soft X-rays to ionize inner shell electrons from target atoms. If the X-rays have a photon energy $h\nu$, the kinetic energy E_k of the emitted electron is given by

$$E_k = h\nu - E_B \quad (8.6)$$

where E_B is the binding energy of the emitted electron. The binding energy of the emitted electron is not only determined by the atomic configuration, but is also influenced by the chemical bonds of the atom. The resolution of XPS is high enough to resolve the chemical state of an atom; consequently not only information on the atomic particle densities in the target is obtained, but also on the chemical composition. The range of this diagnostic is only a few nanometers. Although the X-rays can penetrate several μm into the solid state, only those electrons that are emitted in the top few nm of the sample escape without energy loss. All electrons from deeper lying atoms will lose energy and form a continuous background.

In this work Al- K_α X-rays, 8.3401 \AA , were used. The positive charge built up at the sample due to the Auger electron emission is compensated by

adding slow electrons to the space near the sample. As this compensation is not perfect, a small energy offset usually still remains, due to either under- or overcompensation of the charging. This shift can be calibrated on a known energy peak in the spectrum. For this target the carbon C 1s line was used.

A comprehensive characterization of the discussed material analysis techniques is given in table (8.1).

technique	type	range	area	application
HEIS	ion in, ion out	10 μm	5 mm ²	depth resolution
PIXE	ion in, X-ray out	10 μm	15 mm ²	sensitivity, Z>11
XPS	X-ray in, electron out	3 nm	1 cm ²	chemical information

Table 8.1. Overview of the used diagnostics and typical characteristics

8.5 Results

The effect of the plasma treatment is studied on two groups of samples. The first group consists of a selection of findings from an excavation at Elst, The Netherlands. To the judgement of the involved conservator [88] the corrosion layer on these artifacts was problematic, which means that the specimen were hard to conserve. Therefore they presented a good test case for the plasma treatment. All samples had an incrustation of several mm's thick and were in a very similar condition. This collection was used for a qualitative comparison of various plasma treatments on crust removal and post-corrosion. Artifacts from this group will hereafter be referred to as *Elst* samples.

For the nuclear analysis techniques it is demanded that samples are smaller than 3x3 cm and have a thickness of less than 3 mm. This defined the second group of samples. For this purpose two types were used. A small number of platelets could be cut from a steel plate from a 19th century ship wreck. They will be referred to as *Ship wreck* samples. A larger group of platelets, hereafter referred to as *standard*, was made from a steel corner profile. The origin and age of this corner profile is unknown, but as will be argued the corrosion layer predominantly contains akageneite and is therefore a good representative for problematic corrosion layers.

8.5.1 Elst samples

From the Elst excavation 15 medieval knives were selected, dating from the 8th to 11th century. All knives were in a very similar state. They have been

divided over 5 groups of three. Four groups have been subjected to different plasma treatments. The fifth group was cleaned with abrasive techniques. No plasma treatment has been applied to this group. A sixth group was added, consisting of artifacts that were more different in shape, age and condition. The treatment conditions for each group are tabulated in table 8.3. After plasma treatment the incrustation was removed. The remaining artifacts were impregnated with epoxy resin, type Araldit AY 103-HY 956. For comparison with the Vepřek method, a small number of samples was dipped in a dispersion of microcrystalline wax in a solution of 7% Paraloid B72 in toluene.

Removal of the incrustation was greatly facilitated for all plasma treated artifacts. The incrustation had become very brittle and was easily removed from the artifact with a scalpel knife. As a consequence, fine surface details could be preserved that would have been lost on artifacts from which the incrustation was removed by abrasive methods. Another property of the plasma treated samples is the increased porosity of the top corrosion layer. This facilitates the post-treatment, as the epoxy is easier absorbed by the artifact and shows better adhesion.

corrosion scale	description
0	no corrosion observed
1	sporadic (5 or less on artifact) spots < 1 mm
2	frequent (more than 5 on artifact) spots < 1 mm
3	frequent spots 1-2 mm
4	corroded spots > 2 mm
5	flakes

Table 8.2. Definition of corrosion scale

A classification of the degree of corrosion ranging from 0 to 5 is introduced to evaluate the post-corrosion of the artifacts. A corrosion classification 0 corresponds to the absence of post-corrosion, 5 to corrosion resulting in blisters coming of the artifact. The definition of all corrosion scales is given in table 8.2. The effect of the treatment on the Elst artifacts is evaluated in table 8.3. The first four columns describe the plasma settings. The temperature T in the table is the temperature of the surface of the artifacts. It was measured with an infrared pyrometer through a NaCl window. Group I to III were treated for 30 minutes in a reducing argon/hydrogen plasma. Group IV was also treated for 30 minutes in an argon/hydrogen plasma, after which the gas was switched to argon/nitrogen. This nitriding plasma was applied for 15 minutes. In the table the first gas flows and temperature correspond

group	H ₂ (slm)	Ar (slm)	N ₂ (slm)	p (Torr)	T (°C)	colour	corrosion scale		
							nr 1	nr 2	nr 3
I	2.85	0.5	-	5	160	bl/br	2	1	2
II	2.85	0.15	-	1.2	200	bl	2	3	2
III	2.85	0.15/0.6	0/2.4	2	300	r/bl	0/2	0	0
IV	0.3	2.7	-	2	400	bl/br	1	1	1
V	-	-	-	-	-	red/br		1-5	
VI	0.6	2.4	-	1.5	270	-		1-3	
WAX	0.6	2.4	-	1.5	270		heavy corrosion		
MAINZ					400		heavy corrosion		

Table 8.3. Overview of the plasma conditions and the influence on the corrosion layer. Group I to V consisted of 3 knives each. Group VI was a collection of 8 artifacts of various age, roman age to 17th century. The group indicated by WAX also concerned different items. These were all plasma pre-treated and after removal of the incrustation dipped in wax. All items in group WAX showed heavy corrosion, also the knives present in this group. The group called MAINZ was from the same excavation, and also enclosed knives. This group was treated in a Vepřek type machine. These were also post-treated with wax.

to the argon/hydrogen plasma, the second to the argon/nitrogen plasma. In the evaluation of the corrosion degree and colour of this group also two values are given in the table. On the nitrified artifacts two regions were observed: an inside region of ≈ 5 cm in diameter that was in the plasma beam during treatment, and a region outside the beam¹. The beam part of the samples had a red colour, probably due to nitriding. On this part on none of the three samples any corrosion was observed. The outside region was black. Corrosion on the outside region was only observed on the first sample. Group WAX is a group of artifacts that had a similar plasma treatment as group VI, but was post-treated with wax instead of epoxy resin. As mentioned this is the default post-treatment method applied by Vepřek [84]. The MAINZ group was a similar group of artifacts that was sent to the University of Mainz by the ROB (Rijksdienst voor Oudheidkundig Bodemonderzoek, Dutch institute for archeological soil research). They were treated according to the Vepřek plasma method. In the Vepřek method after a first 2 hour plasma treatment the incrustation is removed. A second plasma treatment of typically 20 hours is applied to remove chlorides from the artifact. Finally the artifact is coated with microcrystalline wax. Results show that wax impregnated artifacts show strong post-corrosion. There was no significant difference observed

¹The diameter of the plasma beam is actually larger than 5 cm. The sample holder, however, is a mesh basket with an opening at plasma side of 5 cm.

between samples treated at the Eindhoven University and samples treated the Vepřek way if a wax post-treatment was applied. Apparently a proper post-treatment is essential and wax is not appropriate.

The combination of a reducing argon/hydrogen plasma, and subsequently an argon/nitrogen plasma in combination with the Araldit post-treatment gives the best results. In fact parts of the nitrided artifacts that were in the plasma beam, did not show any corrosion. The after-treatment is essential, as comparison between wax and epoxy coated artifacts learns. It is noted here that the post-corrosion on the plasma treated and epoxy impregnated artifacts occurred within a year after treatment. After the first year these artifacts were stable.

8.5.2 Platelets

The platelets were used to obtain quantitative results on the influence of the plasma treatment on the reduction of oxides and chlorides from the corrosion layer. Results are ordered according to oxygen and chlorine reduction. Oxygen reduction is determined from HEIS spectra. The chemical bonding of oxygen before and after treatments is observed with XPS. The chlorine content of platelets is determined from PIXE spectra.

Oxygen reduction

The ratio of oxygen to iron can be determined from the surface beneath the iron and oxygen step in the HEIS spectra. This ratio was found to be 2.1 ± 0.1 for untreated platelets, corresponding to FeOOH in the corrosion layer. Dehydrated samples had an oxygen/iron ratio that was 1.5 ± 0.1 . This is the stoichiometry of Fe₂O₃, dehydrated FeOOH. Fig. 8.3 shows HEIS spectra of three shipwreck platelets. The upper curve represents an untreated platelet. The middle curve is the spectrum of a platelet that was dehydrated in a vacuum oven at 400 °C. The treatment time was 20 minutes; longer dehydration does not alter the spectrum (spectra not given here). After vacuum oven treatment the oxygen fraction is determined to be ~ 0.75 times lower than in the untreated platelet. This is in agreement with the expected decrease due to the evaporation of the crystal water, transforming FeOOH into Fe₂O₃. The third curve belongs to a sample that was treated for 30 minutes in a 1 slm H₂, 3 slm Ar plasma. Discharge current was 40 A, reactor pressure 2 mbar. The platelet was placed perpendicularly to the plasma flow. At these conditions the surface temperature reached 550 °C. Clearly the oxides are almost completely reduced to metallic iron over at least the top 10 μm.

A time series of plasma treatment is given in Fig. 8.4: zero, 10 and 20 minutes plasma treatment duration. The platelets were of the standard

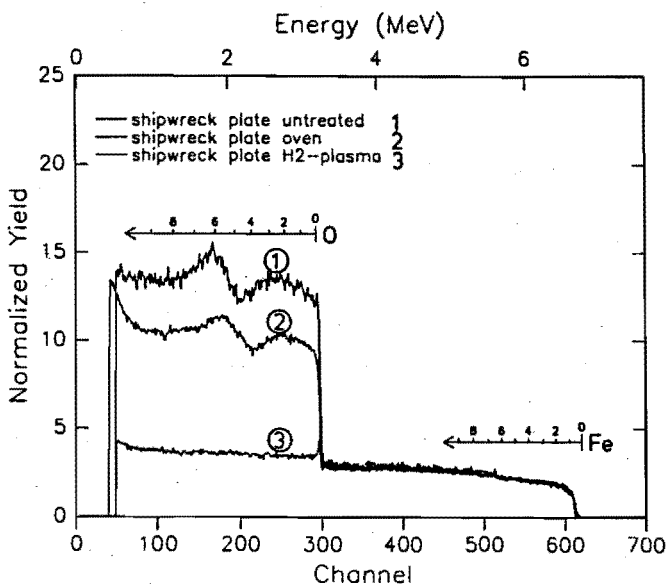


Figure 8.3. HEIS-spectra of three shipwreck platelets. The upper one represents an untreated platelet, the middle a dehydrated sample and the lower curve a hydrogen plasma treated sample. Clearly an iron and an oxygen step are observed in curves 1 and 2. In curve 3 (plasma treated platelet) the oxygen step has disappeared.

type. The depth-dependence of the oxide concentration suggests that the oxide reduction takes place at the interface of the plasma and the oxide layer rather than in the bulk of the corrosion layer. This could provide a method to control the depth of the oxide reduction with the treatment duration.

Fig. 8.5 shows the XPS oxygen 1s peak of a treated and an untreated standard sample. The presence of a strong OH^- related peak indicates that in the untreated sample akageneite is abundant. In the treated sample this peak has decreased strongly. Dehydration of the corrosion layer transforms FeOOH to Fe_2O_3 and therefore the disappearance of the OH^- related O 1s peak was to be expected. This result is in full agreement with the HEIS spectra.

The relation between the treatment conditions and the reduction of oxides is depicted in Fig. 8.6. The oven treatment and the pure argon treatment yield an oxygen reduction to $\sim 75\%$ of the untreated platelet. This corresponds to dehydration of akageneite. Further reduction of oxides takes only place under the presence of hydrogen. The fraction of hydrogen seeded to the plasma does not show an apparent correlation with the degree of reduction, Fig. 8.6(a). Provided there is hydrogen in the plasma, the reduction is

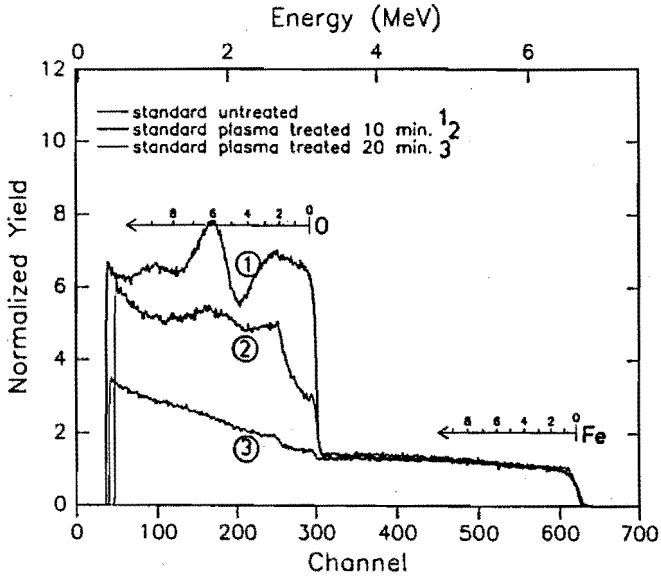


Figure 8.4. *The influence of treatment time in a hydrogen plasma (standard type platelets). The slope in the oxygen step of the lower curve shows that the reduction degree depends on the depth in the material. It can be expected that after a longer treatment time full reduction is achieved over the top 10 μm ; the spectrum will then look identical to the lower HEIS-spectrum of the shipwreck platelets*

clearly correlated with the treatment temperature, Fig. 8.6(b).

Chlorine removal

The PIXE spectra from Figs. 8.7 and 8.8 show the composition of the top 10 μm of an untreated and a plasma treated standard platelet. The plasma settings for the latter were 10% H_2 in a total Ar/H_2 flow of 3.5 slm, arc current 70 A, and reactor pressure 2 mbar. The temperature at the surface of the platelet was measured to be 560 $^\circ\text{C}$. At these settings the best results up to now on chlorine reduction were found (cf. later). The chlorine peak in the spectrum of the untreated platelet corresponds to a chloride to iron ratio of of 5:100. This corresponds to the composition of akageneite, cf. section 8.2. In the spectrum of the treated platelet the Cl peak has disappeared; this corresponds to a Cl fraction of less than 10^{-5} . Fig. 8.9 (a) shows the chlorine reduction versus treatment temperature for a series of standard type platelets. In this series the platelets were mounted on a heated sampleholder under an angle of 60 $^\circ$ with the plasma beam in the center of the reactor. The

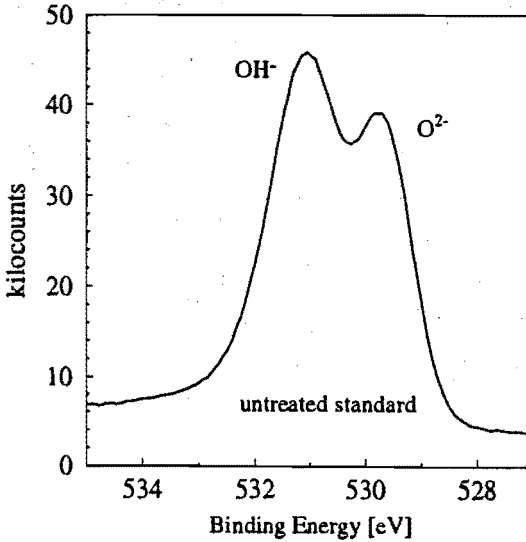


Figure 8.5. XPS oxygen 1s peak of an untreated standard type platelet. The line shape indicates that FeOOH (akageneite) is the dominant chemical component of the corrosion layer. (b) XPS oxygen 1s peak of a plasma treated platelet. The decrease of the OH^- peak indicates gross dehydration of the corrosion layer.

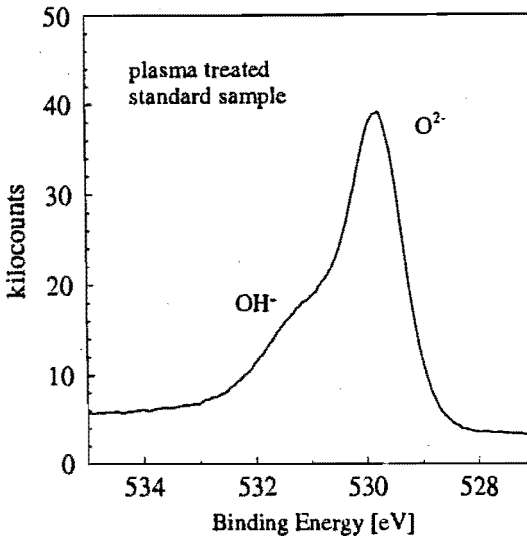


Figure 8.6. (a) The oxygen concentration near the surface (after treatment, normalized to untreated platelet) as a function of treatment temperature during treatment. (b) Same data, but now as a function of hydrogen fraction in the input gas. The total gas flow was kept constant in all plasma treatments. The pressure in the plasma chamber was 0.4 mbar. The discharge current was in the range from 50 to 70 A.

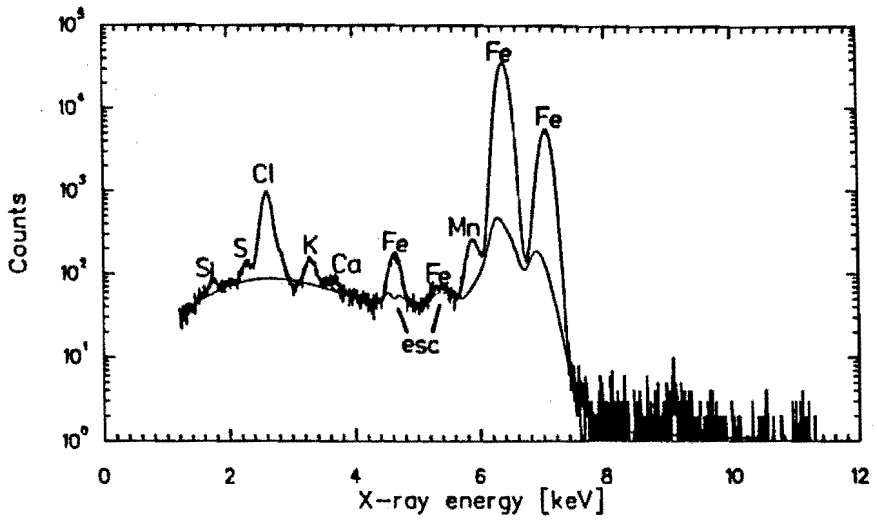


Figure 8.7. PIXE spectrum of an untreated standard type platelet. A strong Cl peak is observed in the spectrum. The iron-to-chlorine ratio determined from this spectrum is 1:0.05. This is the stoichiometry from Cl saturated akageneite, $\text{FeOOH}\cdot\text{Cl}_{0.05}$. The lower curve in the figure represents a background fit.

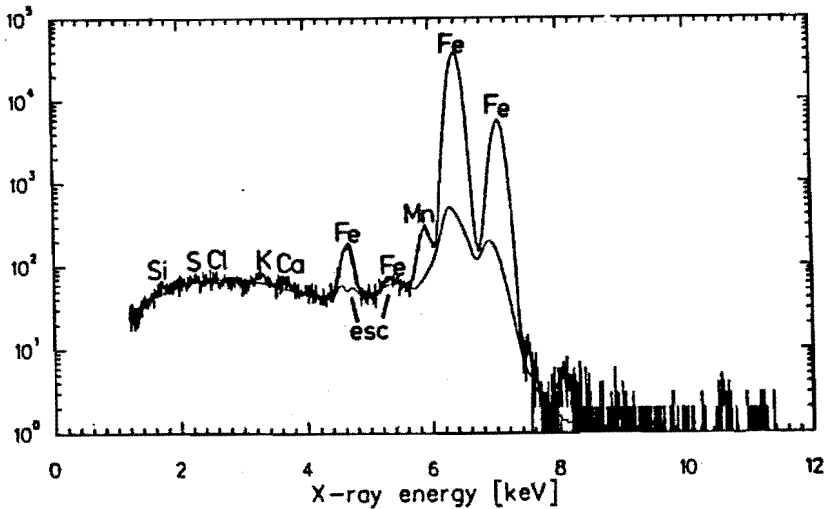


Figure 8.8. PIXE spectrum of a standard type platelet after 20 minutes plasma treatment. The Cl peak has disappeared from the spectrum.

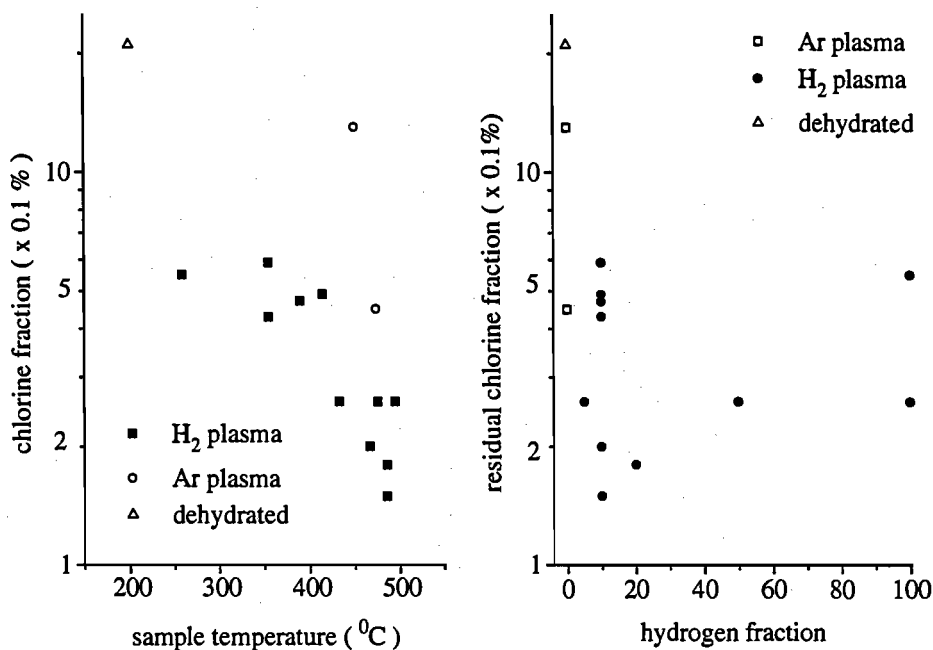


Figure 8.9. (a) Chloride content in standard platelets as a function of temperature. All platelets were treated at approximately the same pressure (0.4-0.5 mbar) and were mounted on a heated sampleholder. (b) The same datapoints as in (a) but now plotted as a function of the hydrogen fraction seeded to the plasma.

total gas flow was kept at 3.5 slm in all treatments, and the reactor pressure was held constant at 0.45 ± 0.05 mbar. The discharge current varied from 30 to 70 A and the hydrogen fraction of the total flow from 0 to 100%. The treatment temperature is the temperature measured on the platelet at the end of the plasma treatment. The temperature generally rises slowly to its end value, which is reached within 10 to 15 minutes. Data points that correspond to a treatment temperature <410 °C did not have additional heating from the sample holder. These platelets were treated for 20 minutes. Data points that correspond to temperatures >410 °C were preheated with the sample holder. The plasma treatment time after preheating was 10 minutes. The residual chlorine fraction decreases with treatment temperature. Furthermore at the same temperature a better chlorine removal is obtained in a hydrogen plasma than in an argon plasma. There is no apparent correlation between the seeded hydrogen fraction and chlorine removal in hydrogen containing plasmas, Fig. 8.9 (b). The inaccuracy in the figure is determined by the inaccuracy in the peak area determination in the PIXE spectrum. The

standard deviation in this determination is $\approx 15\%$.

A final remark is made on the oxide reduction observed at the platelets used in Fig. 8.9. As the temperature during treatment of these platelets was just above $400\text{ }^{\circ}\text{C}$, oxygen reduction is not expected, bearing the results from Fig. 8.6 in mind. Indeed the oxygen fraction of the platelets was found to correspond to a dehydrated corrosion layer. An overview of the chlorine reduction for standard and shipwreck types of platelets and for a wide range of plasma treatment conditions is given in Fig. 8.10. The squares represent standard type platelets, circles represent the shipwreck type samples. Hydrogen plasma treated platelets have open markers, argon plasma treated platelets have open markers with a cross inside and vacuum oven platelets have solid markers. The figure shows quite large scatter of data points. Especially in the hydrogen plasma treated samples the scatter is large. The three highest lying hydrogen points represent treatment at a different orientation (perpendicularly to the plasma beam) than the default orientation (30° with the plasma axis) and pressure (2 mbar) than the default pressure (0.45 mbar). Apparently details of the treatment conditions are important. Some trends are visible though. The chlorine reduction is better at higher temperatures. Full reduction (below the detection limit of PIXE) has only occurred in a hydrogen plasma at a high temperature, $560\text{ }^{\circ}\text{C}$. This can not be achieved with an oven or argon plasma treatment at equally high or higher temperatures. Note that the $560\text{ }^{\circ}\text{C}$ hydrogen plasma treatment is also the only treatment that yielded an almost complete reduction of the oxides over the top ten micrometer.

	untreated	Ar plasma $400\text{ }^{\circ}\text{C}$	H_2 plasma $400\text{ }^{\circ}\text{C}$
Cl:Fe	190:100	28:100	3.4:100

Table 8.4. Cl-to-Fe ratio measured in untreated, argon plasma treated and hydrogen plasma treated FeCl_2 pellets.

The relevance of a hydrogen plasma in comparison to the thermal, non-reducing argon and oven treatments is also tested on ferrous chloride (FeCl_2) pellets, table 8.4. An argon plasma treatment at $400\text{ }^{\circ}\text{C}$ gives a reduction of the Cl:Fe ratio from 190:100 to 28:100. The hydrogen plasma at the same temperature reduces the chlorine content to 3.4:100, which is approximately 8 times better. Both the argon and hydrogen plasma treatment were performed at the default reactor pressure of 0.45 mbar. The current was 30 A in the argon case and 45 A in the hydrogen plasma case. This resulted in a sample temperature of $400\text{ }^{\circ}\text{C}$ in both cases. The treatment time was 20 minutes.

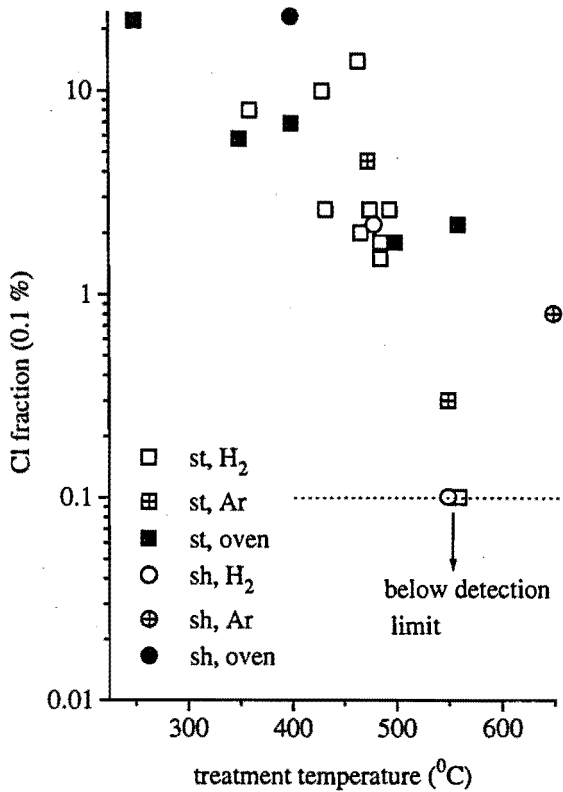


Figure 8.10. Overview of chlorine concentrations measured on both shipwreck and standard type platelets and for a wide range of treatment conditions. The chlorine fraction on an untreated platelet is 5%.

8.6 Discussion

The effect of a hydrogen plasma treatment was studied on knives from the Elst excavation. The incrustation removal is greatly enhanced compared to not plasma treated artifacts. This is in agreement with observations from other authors in high temperature hydrogen gas flows [76] and reducing plasma environments [84, 85]. The facilitation of incrustation removal is attributed to the reduction of Fe_2O_3 to Fe_3O_4 in the incrustation. Fe_3O_4 has a smaller lattice size than the Fe_2O_3 . The incrustation will therefore shrink, whereas the underlying Fe_3O_4 does not. The mechanical stress that is built up results in separation of the incrustation.

The Fe_3O_4 or magnetite layer, that is found underneath the incrusta-

tion and is to be preserved, usually becomes more porous and brittle after the plasma treatment. The artifact thus becomes more vulnerable to mechanical damage. The strength of this layer can be restored by a suitable post-treatment. Most plasma treated artifacts from the Elst finding have been covered with Araldite epoxy resin. The porosity of the magnetite appeared to be an advantage for the Araldite dipping, as the attachment of the epoxy resin was enhanced. This results in a strong protective coating on the artifacts. A disadvantage of the Araldite coating is that it may be considered esthetically less favourable; a shine comes over the artifacts causing fine surface details to become less visible. The Araldite treatment is furthermore not very easy undone, if this might be desired later.

The post-corrosion behaviour of the plasma-treated and Araldite coated Elst artifacts is good. On the average little corrosion is observed, whereas not plasma treated artifacts show strong post-corrosion. Results depend on the plasma settings. The best results were found for samples that first had a hydrogen plasma treatment followed by a nitrogen plasma treatment. As only four plasma settings were tested and no plasma treatment took place after the removal of the incrustation, further improvements are envisaged. Samples that were coated with a wax layer instead of Araldite showed strong post-corrosion. This accounts both for artifacts treated in the Eindhoven plasma machine as for artifacts that had a Vepřek type treatment at the University of Mainz.

Envisaging the succes of the plasma treatment on the Elst artifacts, the platelet experiments were started to get insight in the effect of plasma treatment on a corrosion layer. Focus was put on the chlorine and oxide reduction. Most platelets were of the standard type. An important question is whether this standard type is representative for corrosion layers found on real artifacts. The HEIS spectra indicate that the iron-oxygen ratio of the untreated platelets has the stoichiometry of akageneite. The chlorine to iron fraction is found to be 0.05:1 with PIXE. This is the stoichiometry of chloride saturated akageneite, $\text{FeOOH} \cdot \text{Cl}_{0.05}$. The O1s peak in the XPS spectrum of the standard platelets finally has the profile that is found in FeOOH bonds. Therefore it is concluded that the bulk of the corrosion layer of the standard type samples consists of akageneite.

In section 8.2 it is argued that the chlorides hosted in this akageneite are problematic chlorides to remove. Therefore the standard platelets represent problematic corrosion layers. A strategy that is capable of removing chlorides from these platelets is expected to be succesful on real artifacts too. For the reduction of oxides a reducing environment is necessary. In hydrogen containing plasmas the reduction increases with sample temperature. Below 400 °C no oxide reduction is observed. It is known [85] that reduction of Fe_3O_4 with molecular hydrogen is only exothermal above this temperature. From the above the conclusion is natural that for oxide reduction the abun-

dance of atomic hydrogen in the plasma is not essential. This is however not a definite conclusion yet. It is not impossible that the dissociation degree of the plasma beam correlates with the plasma temperature rather than with the hydrogen fraction of the seeded gas. If recirculation into the plasma jet is important [93], the plasma is diluted with colder background gas. The dissociation degree is lowered and the heat flux to the substrate is smaller. A higher hydrogen fraction in the plasma source yields a stronger influence of recirculation, and if this effect is strong enough a low dissociation degree can correlate with a low substrate temperature and a high hydrogen seeding fraction.

The removal of chlorine is also dependent on the sample temperature. The picture that arises from the PIXE data on treated samples is that chlorine removal is better in a hydrogen containing plasma than in an argon plasma or a vacuum oven at similar treatment temperature and duration. An exceptional reduction is found for samples treated at high temperatures ($> 550\text{ }^{\circ}\text{C}$) in a hydrogen plasma. Under these conditions removal of chlorines to below the detection limit of PIXE (100 ppm relative to iron) was achieved. These conditions also yielded almost full oxide reduction. As a treatment at equally high or higher temperatures in an argon plasma did not yield full removal, it is likely that full chlorine removal demands oxide reduction as well. This could mean that the oxide lattice structure has to be dismantled before all chlorine can be removed.

In the literature on heat [78] and plasma [84, 85] treatment a maximum treatment temperature of $400\text{ }^{\circ}\text{C}$ is mentioned. Above this temperature metallurgical information would be lost, which is undesirable. This would mean, that the high temperature treatments that led to full chlorine and fargoing oxide reduction are not acceptable for conservation. However, this temperature limit originates from a mis-interpretation of a paper from North et al. [94]. In that paper heat treatments at 400 , 600 and $1000\text{ }^{\circ}\text{C}$ are compared. Only after the $400\text{ }^{\circ}\text{C}$ treatment the metallurgical structure was not found to be damaged. There is an important phase transition for iron-oxygen at $570\text{ }^{\circ}\text{C}$, but not close to $400\text{ }^{\circ}\text{C}$ [95]. Therefore a better restriction on treatment temperature is 'below $560\text{ }^{\circ}\text{C}$ ' rather than 'not above $400\text{ }^{\circ}\text{C}$ '. In the case of a plasma treatment this is an important difference. Reduction of oxide and chlorine goes faster at increasing temperature. A high temperature can be reached by pulsing hydrogen into an argon plasma; the argon plasma beam has the larger energy flux and heats the artifacts, whereas the hydrogen pulses provide atomic and molecular hydrogen. The duty cycle of the pulse can be used to control the treatment temperature.

The relevance of a hydrogen plasma in comparison with an argon plasma or heat treatment for the removal of chlorine from the corrosion layer was confirmed by the experiments with FeCl_2 pellets. The hydrogen plasma treatment yielded at the same temperature as the argon treatment an 8x lower

residual chlorine concentration. Yet with the argon treatment already a strong reduction was achieved. As thermal decomposition of FeCl_2 is not possible at 400°C , another explanation is needed. Between production and treatment of the pellets they were exposed to the lab atmosphere for one day. It appeared that the ferrous chloride was already fully hydrated; they looked literally soaking wet. In this hydration process FeCl_2 is transformed to FeOOH and acid chloride. These can be decomposed thermally at 400°C . The better results with a hydrogen plasma can be explained from residual FeCl_2 in the pellets: this can not be decomposed thermally at 400°C and therefore has to be reduced chemically at this temperature which requires atomic hydrogen to be exothermic.

What residual chlorine concentration is acceptable for long term conservation? There is no clear answer to this question yet. The way the chlorine is distributed over the artifact and the chemical form are important factors. Sjögren and Buchwald [92] have observed chlorine infections in test chambers when the local chlorine concentration relative to iron was 0.08%. Below this value the artifacts are considered to be safe. For argon plasma or heat treated samples this is critical; hydrogen plasma treated samples generally have residual chlorine concentrations below this value. The PIXE measurements concern the top $10\ \mu\text{m}$ of the platelets. Chlorines that are built in deep inside the corrosion layer may not be reached by the plasma treatment, although this depends on the porosity of the corrosion layer. On many artifacts under the incrustation a corrosion layer of several mm's thickness is found, that has to be preserved. As full chlorine removal over the full corrosion layer demands change of the crystalline structure of this layer damage may not be avoided. Results on the Elst samples suggest that a strategy without full chlorine removal is feasible. The Elst samples were all treated under mild plasma conditions; the treatment temperature did not exceed 400°C in all cases. Full chlorine removal is unlikely under these circumstances according to the platelet results. Yet the combination of plasma treatment and post-treatment appear to be good. An appropriate strategy may be to treat a thin top layer and apply a post-treatment to passivate further corrosion. The Araldit coating applied on the Elst artifacts gave satisfactory results in combination with a proper plasma treatment. The opportunities for plasma post-treatment are furthermore large. Probably the esthetical disadvantages of the Araldite coating can be overcome if instead a plasma coating is applied. Examples of plasma coating can be found in other work. Buuron [96] found good corrosion resistance on iron coated in an argon plasma beam seeded with a mixture of acetylene and CF_4 . He used an almost identical plasma machine as used in the here presented work, featuring a cascaded arc source expanding into a low pressure chamber. In the present work artifacts that were exposed to a N_2 seeded plasma, even though the encrustation was not yet removed, showed no post-corrosion. An optimized strategy may incorpo-

rate two cycles of plasma treatment. A first, short exposure of the artifact to a hydrogen seeded plasma, after which the encrustation is removed. Subsequently the application of a convenient combination of plasma seedings can be used to make a suitable coating.

Two final remarks are made on very down-to-earth advantages of the Eindhoven plasma treatment. The low pressure treatment chamber and high energy flux from the plasma beam enable a safe method to expose artifacts to a hydrogen atmosphere at high temperatures. From the results it appears that the hydrogen fraction in the total gas flow can be kept below 4%, the explosion limit of hydrogen in air. This makes plasma treatment possible without specific safety measures. Finally, the treatment time of artifacts in the Eindhoven machine is typically 20 minutes. In a complete strategy including plasma post-treatment this is unlikely to exceed 1-2 hours. This is even more favourable than the fastest alternative so far, the Vepřek method, with a total time including post-treatment of 20 to 24 hours, where more conventional chemical methods like the alkalide sulphite treatment take months of treatment time.

Conclusions

- The expanding cascaded arc setup can also be used as a hydrogen atom or ion source. If properly constructed and operated, the standing time of the source is long ($\gg 2000$ hours).
- A hydrogen plasma emanating from the cascaded arc source has a dissociation degree ranging from 30% to almost full dissociation. Downstream the plasma beam the dissociation degree decreases. This is a result of the recirculating molecular background gas, that is formed by wall association of atomic hydrogen. The recirculation flow will enter the plasma beam and lower the averaged dissociation degree in the beam. At a position 25 cm downstream the source the dissociation degree is typically 10%. The recirculating molecular gas here apparently dominates the neutral density.
- The dissociation degree in a recombining plasma beam can be determined with RF excited active actinometry. This method has an estimated accuracy of 25%.
- Anomalous fast recombination leads to an ion density that is several orders of magnitude lower in a hydrogen plasma beam than in an argon plasma beam. This anomalous fast recombination starts with a charge exchange $\text{H}^+ + \text{H}_2(v, r) \rightarrow \text{H} + \text{H}_2^+$ that converts the atomic ions emanating from the source to molecular ions. Dissociative recombination of molecular ions is fast enough to explain the observed fast recombination.
- The atomic state distribution function that is determined from the atomic emission spectrum of the plasma beam, can only be explained if molecular recombination processes provide sources for excited atomic states. Molecules with a high vibrational or rotational energy must be abundant.

- The molecular Fulcher α band ($d^3\Pi \rightarrow a^3\Sigma$) can be used to determine the ground state rotational temperature of the molecular gas in the plasma, provided that the transfer of angular momentum in the excitation of the $d^3\Pi$ state is accounted for. A determination of the ground state vibrational distribution from the spectrum is hazardous, because the image of the vibrational distribution to the spectrum is very diffuse. Only the ratio $v = 1 : v = 0$ can be determined with a reasonable accuracy. If the atomic H_α spectral line is measured too, the dissociation degree of the plasma can be estimated.
- From rotational temperatures measured at the FOMSCE plasma is concluded that the neutral gas in the plasma mainly is background molecular gas. Rotational heating of the gas is dominated by electron collisions. The rotational temperature is weakly coupled to the electron temperature, $T_{rot} = 400 - 600$ K. Under default conditions the neutral density is too low to cause significant detachment of negative ions coming from the converter that cross the plasma.
- In the conservation of iron archeological artifacts, a short exposure to a hydrogen plasma beam is effective. Removal of detrimental chloride infections can be achieved in a 20 minute treatment. In order to stop the corrosion of artifacts, after chlorine removal a further post-treatment is crucial. A hydrogen plasma treatment followed by an Araldit epoxy coating has given good results. A plasma posttreatment, has not been investigated yet on artifacts. However, Buuron showed, that good anti-corrosion coatings can be obtained when hydrocarbons are seeded to the plasma beam. A complete plasma treatment including the application of an anti-corrosive coating will take 1 to 2 hours. This is an enormous improvement compared to conventional chemical methods, where a treatment time of months is common, or the Vepřek plasma method, where a treatment time of 20 to 24 hours is needed.

References

- [1] G.M.W. Kroesen, C.J. Timmermans, D.C. Schram, *Pure&Appl. Chem.* **60**, 795 (1988)
- [2] J.J. Beulens, A.J.M. Buuron, D.C. Schram, *Surface&Coating Techn.* **47**, 401 (1991)
- [3] G.M.W. Kroesen, D.C. Schram, J.C.M. de Haas, *Plasma Chem.&Plasma Processing* **10** (1990)
- [4] A.T.M. Wilbers, G.J. Meeusen, G.M.W. Kroesen, D.C. Schram, *Thin Solid Films* **204**, 59 (1991)
see also G.J. Meeusen, Ph. D. thesis, Eindhoven University of Technology (1994)
- [5] H.J.G. Gielen, D.C. Schram, *IEEE Trans. Plasma Sci.* **18**, 127 (1990)
see also H.J.G. Gielen, Ph. D. thesis, University of Eindhoven, The Netherlands (1989)
- [6] M.C.M. van de Sanden, J.M. de Regt, D.C. Schram, *Phys. Rev. E* **47**, 2792 (1993)
see also M.C.M. van de Sanden, Ph. D. Thesis, Eindhoven University of Technology, The Netherlands (1991)
- [7] R. Severens, private communication, Eindhoven University of Technology, The Netherlands
- [8] Z. Qing, internal report University of Technology Eindhoven, ISBN 90-5282-226-3 The Netherlands (1992)
- [9] John D. Anderson Jr. , 'Fundamentals of aerodynamics', McGraw Hill N.Y. (1984)
or
George Emanuel, 'Gas dynamics:theory and application', AIAA educational series, N.Y. (1986)
- [10] J.J. Beulens, M.J. de Graaf, G.M.W. Kroesen, D.C. Schram, *Proc. Materials Research Soc. Spring Mtg.*, Vol. 190, San Fransisco (Materials Research Society, Pittsburgh, 1990).
- [11] P.M. Vallinga, 'Cascaded arcs for neutralizers', NET report NET/88-145 (1988)
- [12] S.I. Braginskii, in *Rev. on Plasma Physics*, **1**, 205 (1965).
- [13] 'Atomic Transition Probabilities, Hydrogen Through Neon', NSRDS, NBS 4, Washington (1966)
- [14] B. Jackson, M. Persson, *J. Chem. Phys.* **96**, 2378 (1992)
- [15] P.J. Eenshuistra, J.H.M. Bonnie, J. Los, H.H. Hopman, *Phys. Rev. Lett.* **60**, 341 (1988)
- [16] R.I. Hall, I. Čadež, M. Landau, F. Pichou, C. Schermann, *Phys. Rev. Lett.* **60**, 337 (1988)
- [17] J.R. Hiskes, A.M. Karo, *J. Appl. Phys.* **56**, 1927 (1979)
- [18] M. Bacal, A.M. Bruneteau, M. Nachman, *J. Appl. Phys* **55**, 15 (1984)
- [19] M.B. Hopkins, K.N. Mellon, *Phys. Rev. Lett.* **67**, 449 (1991)
- [20] J.M. Shull, *The Astroph. J.*, **227**, 131 (1979)
- [21] A.T.M. Wilbers, G.J. Meeusen, M. Haverlag, G.M.W. Kroesen, D.C. Schram, *Thin Solid Films*, **204**, 59 (1991) *Coatings Techn.* **47**, 401 (1991) Kroesen, D.C. Schram, *Thin Solid Films* **204**, 59 (1991)
- [22] M.J. de Graaf, R.P. Dahiya, F.J. de Hoog, M.J.F. van de Sande, D.C. Schram, *J. Phys. (Paris)*, *Colloq.* **51**, C5-387 (1990)
- [23] J.A.M. van der Mullen, *Phys. Rep.* **191**, 109 (1990)

- [24] J.C. Morris, R.P. Rudis, J.M. Yos, *The Physics of Fluids* **13**, 608 (1970)
- [25] W.R. Ott, K. Behringer, G. Gieres, *Appl. Optics* **14**, 2121 (1975)
- [26] R.F.G. Meulenbroeks, A.J. van Beek, A.J.G. van Helvoort, M.C.M. van de Sanden, D.C. Schram, *Phys. Rev. E* **49**, 4397 (1994)
- [27] N.G. Adams, D. Smith, E. Alge, *J. Chem. Phys.* **81**, 1778 (1984)
- [28] M.T. Leu, M.A. Biondi, R. Johnson, *Phys. Rev. A* **8**, 413 (1973)
- [29] J.A. MacDonald, M.A. Biondi, R. Johnsen, *Planet. Space Sci.* **32**, 651 (1984)
- [30] T. Amano, *J. Chem. Phys.* **92**, 6492 (1990)
- [31] F.B. Youssif, P.J.T. Van der Donk, M. Orakazi, J.B.A. Mitchell, *Phys. Rev. A* **44**, 5653 (1991)
- [32] G. Niedner, M. Noll, J.P. Toennies, *J. Chem. Phys.* **87**, 2685 (1987)
- [33] E.W. McDaniel, 'Collision Phenomena in Ionized Gases' (John Wiley & Sons, New York)
- [34] A. Garscadden and W.F. Bailey, *Progr. in Astronautics and Aeronautics* **74** (1981)
- [35] M.C.M. van de Sanden, thesis Eindhoven University of Technology (1991)
- [36] M.J. de Graaf, R.P. Dahiya, M.C.M. van de Sanden, D.C. Schram, *Phys. Rev. E* **48** 2098 (1993)
- [37] H. Akatsuka and M. Suzuki, *Phys. Rev. E* **49** 1534, (1993)
- [38] P. Hoffmann, W.L. Bohn, *Z. Naturforsch. A* **27**, 878 (1972)
- [39] S. Suckewer, R.J. Hawryluk, M. Okabayashi, J.A. Schmidt, *Appl. Phys. Lett.* **29** 537, (1976)
- [40] G.A. Lukyanov, V.V. Nazarov, N.O. Pavlova, *Opt. Spectrosc.* **44**, 26 (1978)
- [41] T. Hara, K. Kodera, M. Hamagaki, M. Inutake, T. Dote, *Jap. J. Appl. Phys.* **19**, L386 (1980)
- [42] J.A.M. van der Mullen, D.C. Schram, *Spectrochim. Acta* **45B**, 233 (1990)
- [43] M.C.M. van de Sanden, P.P.J.M. Schram, A.G. Peeters, J.A.M. van der Mullen, G.M.W. Kroesen, *Phys. Rev. A* **40**, 5273 (1989)
- [44] M.C.M. van de Sanden, P.P.J.M. Schram, J.A.M. van der Mullen, D.C. Schram, *Phys. Rev. A* **42**, 2461 (1990)
- [45] G. Arfken, 'Mathematical methods for physicists' Academic press, Orlando (1985)
- [46] E.P. Szuszcwicz, P.Z. Takacs, *Phys. Fluids* **22**, 2424 (1979)
- [47] M.C.M. van de Sanden, Z. Qing, D.K. Otorbaev, M.J. de Graaf, J.C.A. Wevers, D.C. Schram, *proc. 5th European Workshop on the Prod. and Appl. of Light Negative Ions*, Dublin (1994)
- [48] M. van Eerden, M.C.M. van de Sanden, D.K. Otorbaev, D.C. Schram, to be published
- [49] G. Herzberg, 'Molecular Spectra and Molecular Structure, I. Spectra of Diatomic Molecules', Van Nostrand, Princeton (1965)
- [50] F. Hund, *Z. Phys.* **36**, 657 (1926)
- [51] L. Pauling and E. Bright Wilson, 'Introduction to Quantum Mechanics', McGraw-Hill N.Y. (1935)
- [52] I. Kovacs, 'Rotational Structure in the Spectra of Diatomic Molecules', Adam Hilger (1969)
- [53] G.R. Möhlmann, F.J. de Heer, *Chem. Phys. Lett.* **42** 240, (1976)
- [54] A.P. Bryukhovetskii, E.N. Kotlikov, D.K. Otorbaev, V.N. Ochkin, P.L. Rubin, S. Yu. Savinov, N.N. Sobolev, *Sov. Phys. JETP* **52**, 852 (1981)
- [55] B.P. Lavrov, V.N. Ostrovsky, V.I. Ustimov, *J. Phys.* **B14**, 4701 (1981)
- [56] M. Rotenberg, N. Metropolis, J.K. Wooten, 'The 3j and 6j symbols'
- [57] B. van der Sijde, *J. Quant. Spectrosc. Radiat. Transfer* **12**, 703 (1972)
- [58] T.E. Sharp, *Atomic Data* **2**, 128 (1971)
- [59] J. Callaway, *Phys. Rev. A* **37**, 3692 (1988)
- [60] R.J. Spindler Jr., *J. Quant. Spectrosc. Radiat. Transfer* **9**, 627 (1969)
- [61] R.L. Day, R.J. Anderson, F.A. Sharpson, *J. Chem. Phys.* **69**, 5518 (1978)
- [62] T. Kiyoshima, *J. Ph. Soc. Japan* **56**, 1989 (1987)
- [63] R.J. Spindler Jr., *J. Quant. Spectrosc. Radiat. Transfer* **9**, 597 (1969)

- [64] R.M. A. Heeren, D. Ćirić, S. Yagura, H.J. Hopman, A.W. Kleyn, *Nucl. Instr. Meth. B* **69**, 389 (1992)
- [65] R.M.A. Heeren, M.J. de Graaf, D. Ćirić, H.J. Hopman, A.W. Kleyn, *J. Appl. Phys.* **75**, (1994) 4340
- [66] R.M.A. Heeren, D. Ćirić, H.J. Hopman, A.W. Kleyn, *Appl. Phys. Lett.* **59**, 158 (1991)
- [67] R.M.A. Heeren, Ph. D. Thesis, Amsterdam (1992)
- [68] 'The hydrogen molecule wavelength tables...', ed. H.M. Crosswhite, Wiley, N.Y. (1972)
- [69] H. Tawara, Y. Itikawa, H. Nishimura, M. Yoshino, *J. Phys. Chem. Ref. Data* **19**, 617 (1990)
- [70] B.F.M. Pots, P. van Hooff, D.C. Schram, B. van der Sijde, *Plasma Physics* **23**, 67 (1981)
- [71] J.M.M.J. Vogels, D.C. Schram, *Plasma Physics* **26**, 297 (1986)
- [72] V.M. Lelevkin, D.K. Otorbaev, D.C. Schram, 'Physics of Non-Equilibrium Plasmas' North Holland, Amsterdam (1992)
- [73] M.J. de Graaf, Z. Qing, G. van Rooij, M.C.M. van de Sanden, D.C. Schram, R.M.A. Heeren, A.W. Kleyn, Proc. 5th intern. symp. on production and neutralisation of negative ions and beams, Brookhaven, Upton N.Y. (1992)
- [74] F. Linder, proc. Int. Conf. Electronic and Atomic Collisions', ed. N. Oda and K. Takayanagi, 535 (1980)
- [75] M.R. Gilbert, N.J. Seeley, *Studies in Conservation* **26**, 50 (1981)
- [76] N.A. North, C. Pearson, *Studies in Conservation*, **23**, 174 (1978)
- [77] W.M. McKewan, *Trans. Met. Soc. AIME* **5**, 2 (1962)
- [78] N.A. North, M. Owens, C. Pearson, *Studies in Conservation* **21**, 192 (1976)
- [79] S. Keene, C. Orton, *Studies in Conservation* **30**, 136 (1985)
- [80] A. Rinuy, F. Schweitzer, *ibid*, 44 (1982)
- [81] N.A. North, C. Pearson, ICOM Committee for Conservation 4th Triennial Meeting, Venice, 1 (1975)
- [82] V. Daniels, *Studies in Conservation* **26**, 45 (1982)
- [83] V. Daniels, L. Holland, M.W. Pascoe, *Studies in Conservation* **24**, 85 (1979)
- [84] S. Vepřek, J. Patscheider, J. Th. Elmer, *Plasma Chem. Plasma Process.* **5**, 201 (1985)
- [85] S. Vepřek, Ch. Eckmann, J. Th. Elmer, *Plasma Chem. Plasma Process.* **8**, 445 (1988)
- [86] M.J. de Graaf, Z. Qing, H.W.A. Tolido, M.C.M. van de Sanden, D.C. Schram, *J. of High Temp. Chem. Processes* **1**, 11 (1992).
- [87] M.J. de Graaf, R. Severens, M.J.F. van de Sande, R. Meyer, H. Kars, M.C.M. van de Sanden, D.C. Schram, *J. Nucl. Mat.* **380** (1993)
- [88] R. Meijers, private communication, ROB Amersfoort, The Netherlands
- [89] J.O.M. Bockris, B.E. Conway, E. Yeager, R.E. White, 'Comprehensive Treatise of Electrochemistry' vol. 4, Plenum, N.Y. (1981)
- [90] M.G. Fontana, 'Corrosion Engineering' McGraw-Hill, N.Y. (1986)
- [91] S. Turgoose, *Studies in Conservation* **27**, 97 (1982)
- [92] A. Sjøgren, V.F. Buchwald, *Studies in Conservation* **36**, 161 (1991)
- [93] M.J. de Graaf, R.J. Severens, D.C. Schram, D.K. Otorbaev, Z. Qing, R.F.G. Meulenbroeks, M.C.M. van de Sanden, 11th. Int. Symp. on Plasma Chem. (ISPC 11) Loughborough, U.K., Ed. J. Harry (IUPAC, 1993)
- [94] N. North, M. Owens, C. Pearson, *Studies in Conservation* **21**, 192 (1976)
- [95] J.S. Kirkaldy, R.G. Ward, 'Ferrous Metallurgy', University of Toronto Press (1964)
- [96] A.J.M. Buuron, thesis Eindhoven University of Technology (1993)

Summary

This thesis reflects the results of a study on the expanding cascaded arc for hydrogen and argon/hydrogen plasmas. The study has been initiated from a demand for an efficient source for hydrogen atoms and ions. In the course of the development of this source some fundamental aspects of the expanding hydrogen plasma have come up. Specifically two items run through this thesis like a thread: 1. the central role of vibrationally or rotationally excited molecules in the plasma kinetics, and 2. the determining influence of plasma-circulation via the wall (recirculation) on the plasma beam characteristics.

In the first part of the thesis the behaviour of the set up for hydrogen plasmas is described. As a reference, the well known argon plasma is used. The energy efficiency in the hydrogen case (35%) is somewhat lower than in the argon case (50%). This is a consequence of the better heat conductivity of hydrogen plasmas. A further consequence of this difference is that the hydrogen plasma source is exposed to a larger heat load, and modifications on the cascaded arc are necessary. The heat balance of the source plasma is used to estimate the dissociation degree of the plasma beam emanating from the cascaded arc. It appears that the dissociation degree is high under all conditions studied, varying from 30% to almost full dissociation.

With a newly developed diagnostical technique, RF-excited active actinometry, the dissociation degree of the same emanating plasma is measured a few decimeters downstream in the expansion. At this position the dissociation degree appears to be significantly lower and values of approximately 10% are found. This loss of dissociation degree is a result of recirculation in the expansion chamber. Hydrogen atoms, flowing from the cascaded arc into the expansion chamber, can circulate in the reactor many times before they are evacuated by the pumps. During this process it is very likely that the atoms form molecules by means of wall association. These molecules can re-enter the plasma beam in a recirculation flow. It is expected that molecules, produced in wall association, leave the wall in a vibrationally high excited state.

The ionization degree of the plasma beam has been measured for argon/hydrogen mixtures. In the plasma beam a recombination catastrophe occurs. The ionization degree collapses to a value that is a few orders of magnitude lower than in an argon plasma under similar conditions. This can be understood assuming that the atomic ions leaving the source, give rise to the production of molecular ions in a charge exchange reaction with vi-

brationally or rotationally excited molecules. The molecular ions can be lost through very fast dissociative recombination. The influence of this is also found in the atomic emission spectrum of the plasma. The atomic distribution functions, that have been determined from emission spectra, are only comprehensible if molecular sources for high excited atomic states are available. These states are only accessible for molecular recombination reactions if the molecules have sufficient internal (vibrational or rotational) energy.

Molecular spectroscopy can be used to obtain information on the rotational and vibrational distribution functions. The interpretation of the Fulcher α band has been studied for the determination of a rotational and a vibrational temperature and for the estimation of the dissociation degree of the plasma. It appears that, although the emission spectrum gives a diffuse image of the rotational distribution of electronic ground state molecules, the rotational temperature can be determined adequately from the emission spectrum. As far as vibration is concerned, only the ratio $v = 0$ to $v = 1$ can be determined. Under certain conditions a good estimate of the dissociation degree can be made from the spectrum. As the recombining plasma beam does not emit a molecular spectrum (due to the relatively low electron temperature) local heating of the plasma with an RF probe (RF-excited active actinometry) was applied in order to obtain a molecular spectrum.

Molecular spectroscopy has also been performed on the FOMSCE-plasma at AMOLF, Amsterdam. In the FOMSCE-experiment a negative ion beam is produced by means of a charge exchange of positive ions at a negatively biased barium surface. For this type of experiment the cascaded arc has been developed as an ion source. Molecular spectroscopy is used to characterize the FOMSCE-plasma. The neutral population in the plasma appears to be determined mainly by the background conditions. A weak coupling of electron and rotational temperature is observed in the plasma. The coupling of the vibrational temperature to the electron temperature is somewhat stronger.

An interesting application of the expanding cascaded arc plasma is found in the conservation of iron archeological artifacts. Without an anti-corrosion treatment these artifacts can be completely destroyed in a short period after excavation. This process can be slowed down by applying a hydrogen plasma. One of the main objectives of a hydrogen plasma treatment is the removal of chlorine from the artifact, as this plays a catalytic role in the corrosion process. A combination of plasma treatment for the removal of chlorine with an adequate post-treatment is likely to stop the corrosion process almost completely. In this work the focus was put on the chlorine removal. With the same plasma machine post-treatment is also possible.

Samenvatting

Dit proefschrift is de neerslag van een onderzoek aan de expanderende cascadeboog van een waterstof- en een argon-waterstof-plasma. De aanzet tot het onderzoek was de vraag naar een efficiënte bron voor waterstofatomen en -ionen. Tijdens de ontwikkeling van deze bron zijn enkele fundamentele aspecten van het expanderende waterstofplasma aan het licht gekomen. Met name twee items lopen als een rode draad door dit proefschrift: 1. de belangrijke rol van sterk aangeslagen moleculen in de plasmakinetic en 2. de bepalende invloed van de circulatie van het plasma via de wand (recirculatie) op de bundeleigenschappen.

In het eerste deel van het proefschrift wordt het gedrag van de opstelling voor waterstofplasma's beschreven. Als referentie wordt het argonplasma gebruikt, omdat dit goed bekend is. Het energierendement van een waterstofboog blijkt wat kleiner te zijn (35%) dan van een argonboog (50%). De betere warmtegeleiding van het waterstofplasma is hier debet aan. Dit heeft overigens ook tot gevolg dat, met een waterstofplasma, de onderdelen van de bron aan een grotere belasting blootstaan, en wel zozeer dat enige aanpassingen ten opzichte van de cascadeboog noodzakelijk zijn. De warmtehuishouding van het bronplasma is gebruikt om de dissociatiegraad van het uit de cascadeboog stromende plasma te schatten. Het blijkt dat de dissociatiegraad onder alle onderzochte condities hoog is, variërend van 30% tot vrijwel volledige dissociatie.

Met behulp van een nieuw ontwikkelde diagnostiek, RF-geëxciteerde actieve actinometrie, is de dissociatiegraad van hetzelfde uitstromende plasma gemeten op een positie van enkele decimeters stroomafwaarts van de bron. Daar blijkt een veel lagere dissociatiegraad van ongeveer 10% te heersen. Deze schijnbare discrepantie is een gevolg van recirculatie in de expansiekamer. Waterstofatomen, die vanuit de cascadeboog de expansiekamer instromen, kunnen vele malen rondgaan voordat ze door de pompen worden afgevoerd. In deze tijd is de kans groot dat de atomen via associatie aan de wand moleculen vormen. Die moleculen kunnen via de circulatiestroming weer opgenomen worden in de plasmabundel. Het is waarschijnlijk dat moleculen, die door wandassociatie ontstaan, in een vibrationeel hoog aangeslagen toestand de wand verlaten.

De ionisatiegraad van het uitstromende plasma is gemeten voor argon/waterstof mengsels. In de plasmabundel blijkt een soort recombinatiecatastrofe op te treden. De ionisatiegraad stort in tot een waarde die enkele ordes van grootte

lager is dan die in een argon plasma onder vergelijkbare condities. Dit is te begrijpen als men aanneemt dat de atomaire ionen die uit de bron komen via ladingsruil met vibrationeel of rotationeel hoog aangeslagen moleculen zorgen voor de vorming van moleculaire ionen. Deze ionen gaan snel verloren via een moleculaire dissociatieve recombinitie-reactie. De invloed van dit soort processen wordt ook teruggevonden in het atomaire emissiespectrum van het plasma. De atomaire verdelingsfuncties, die uit een emissiespectrum worden bepaald, zijn alleen te begrijpen als er moleculaire bronnen zijn voor hoog aangeslagen atomaire niveau's. Deze niveau's zijn niet anders te bereiken dan via moleculaire recombinitieprocessen, mits de moleculen voldoende inwendige (vibrationele of rotationele) energie hebben.

Moleculaire spectroscopie kan gebruikt worden om informatie over de rotationele en vibrationele verdelingsfuncties te verkrijgen. De interpretatie van de Fulcher α band is uitgewerkt hetgeen een rotationele en een vibrationele temperatuur en een schatting van de dissociatiegraad van het plasma oplevert. Het blijkt dat, hoewel het emissiespectrum een diffuus beeld geeft van de rotationele bezetting van moleculen in de electronische grondtoestand, de rotationele temperatuur goed bepaald kan worden uit het emissiespectrum. Wat betreft vibratie kan alleen de bezetting van $v = 0$ ten opzichte van $v = 1$ redelijk goed bepaald worden. Onder bepaalde voorwaarden kan wel een goede schatting van de dissociatiegraad gemaakt worden uit het emissiespectrum. Omdat de recombinerende plasmabundel geen moleculair spectrum uitzendt (de electronentemperatuur is daar te laag voor) is met behulp van een RF-sonde het plasma lokaal verhit (RF-geëxciteerde actieve actinometrie), waardoor toch een moleculair emissiespectrum wordt uitgezonden.

Moleculaire spectroscopie is ook verricht aan het FOMSCE-plasma bij het FOM instituut AMOLF te Amsterdam. In het FOMSCE-experiment wordt een negatieve ionenbundel gemaakt door middel van omlading van positieve ionen aan een bariumoppervlak op een negatieve spanning. Voor dit type experiment is de cascadeboog als ionenbron ontwikkeld. De moleculaire spectroscopie is gebruikt om het FOMSCE-plasma te karakteriseren. De neutralenpopulatie in het plasma blijkt voornamelijk bepaald te worden door achtergrondgas. De koppeling tussen de rotatie- en de electronentemperatuur in het plasma is zwak; die tussen de vibratie- en de electronentemperatuur iets sterker.

Een interessante toepassing van het expanderende cascadeboogplasma als bron voor atomair waterstof ligt in de conservering van archeologische ijzeren voorwerpen. Zonder behandeling tegen corrosie kunnen dergelijke voorwerpen in korte tijd na opgraving -soms zelfs binnen enkele maanden- volledig vernietigd worden. Met behulp van een waterstofplasma kan men dit proces vertragen. Een van de voornaamste taken van het waterstofplasma is het verwijderen van chloor uit het ijzeren voorwerp, omdat dit een katalytische

rol speelt in het corrosieproces. Een combinatie van een plasmabehandeling voor de verwijdering van chloor met een goede nabehandeling kan het corrosieproces waarschijnlijk vrijwel volledig tot stilstand brengen. De nadruk heeft in dit werk op de voorbehandeling gelegen ter verwijdering van chloor. Met dezelfde plasmamachine is waarschijnlijk ook een goede nabehandeling mogelijk.

Curriculum Vitae

- 5 mei 1965 geboren te Zwolle
- mei 1983 examen VWO,
Cobbenhagen College te Tilburg
- nov 1989 doctoraal examen Technische Natuurkunde,
Technische Universiteit Eindhoven
- nov 1989 -
aug 1990 toegevoegd onderzoeker,
vakgroep deeltjesfysica,
Technische Universiteit Eindhoven
- sep 1990 -
sep 1994 onderzoeker in opleiding,
vakgroep deeltjesfysica,
Technische Universiteit Eindhoven

STELLINGEN

behorende bij het proefschrift

A New Hydrogen Particle Source

Mark de Graaf

27 september 1994

1

In plasmabundel-depositie kan atomair waterstof de dissociërende rol die ionen hebben overnemen.

2

In een waterstofplasma kunnen atomaire ionen snel recombineren via achtereenvolgens ladingsruil met rovibrationeel geëxciteerde moleculen en dissociatieve recombinitie. Dit mechanisme kan zelfs bij lage dichtheden van geëxciteerde moleculen dominant zijn over atomaire twee- of drie deeltjes recombinitie.

- Dit proefschrift

3

Door de inmenging van aan de wand gevormde moleculen via recirculatie is bij expanderende waterstofplasma's geen sprake meer van een vrije expansie.

- Dit proefschrift

4

Het bestaan van intense P en R banden in het Fulcher α spectrum is een direct bewijs voor rotatie-aanslag in de elektronische excitatie van het waterstofmolecuul.

- Dit proefschrift

5

De bepaling van de EEDF uit de tweede afgeleide van een electrostatische sonde-karakteristiek zoals beschreven door Langmuir is alleen toegestaan als de sheath verwaarloosbaar dun is.

6

De door North et al aangegeven bovengrens van 400 °C voor de behandeling van archeologische ijzeren voorwerpen berust op een onjuiste interpretatie van experimentele gegevens. Een zinvolle bovengrens is 560 °C, bij welke temperatuur een faseovergang in ijzeroxide optreedt.

- N. North, M. Owens, C. Pearson, *Studies in Conservation* **21**, 192 (1976)

7

De toenemende capaciteit van computers stelt steeds hogere eisen aan de efficiëntie van numerieke algorithmes.

8

Legaliseren van onzorgvuldigheden, begaan door vervolgende instanties in het strafproces, is een aantasting van de rechtsstaat.

9

Afschaffing van het recht op hoger beroep in asielprocedures is in strijd met het gelijkheidsbeginsel zoals vastgelegd in artikel 1 van de grondwet.

10

Het gebruiken van rekenmodellen van het centraal plan bureau om de effectiviteit van een partijpolitiek programma te kwantificeren gaat voorbij aan de aanzienlijke beperkingen van dergelijke modellen.

11

Het idee dat voorzieningen voor studenten nog verder afgebroken kunnen worden is een verlate reactie op het ruimhartige gebruik dat de huidige generatie beleidsmakers heeft gemaakt van de mogelijkheden tijdens hun studietijd.

12

De primaire functie van wetenschappelijke publicaties verschuift van kennisoverdracht naar certificering van onderzoeksresultaten.

13

De hoeveelheid kooldioxide die is vastgelegd in het papier van de rapportage over het broeikas-effect, helpt dit te bestrijden.